Development of additive manufacturing processes for multi-material metal components

Politecnico di Bari

LIBERATORIA PER L'ARCHIVIAZIONE DELLA TESI DI DOTTORATO

Al Magnifico Rettore
del Politecnico di Bari

Il/la sottoscritto/a Posa Paolo nato/a a Bari il 06/10/1982

residente a Sannicandro di Bari in via Gen. C.A. Dalla Chiesa 21/c e-mail paolo.posa@poliba.it

iscritto al 3° anno di Corso di Dottorato di Ricerca in Ingegneria Meccanica e Gestionale ciclo XXXVII

ed essendo stato ammesso a sostenere l'esame finale con la prevista discussione della tesi dal titolo:

Development of additive manufacturing processes for multi-material metal components

DICHIARA

1) di essere consapevole che, ai sensi del D.P.R. n. 445 del 28.12.2000, le dichiarazioni mendaci, la falsità negli atti e l'uso di atti falsi sono puniti ai sensi del codice penale e delle Leggi speciali in materia, e che nel caso ricorressero dette ipotesi, decade fin dall'inizio e senza necessità di nessuna formalità dai benefici conseguenti al provvedimento emanato sulla base di tali dichiarazioni;
2) di essere iscritto al Corso di Dottorato di ricerca in Ingegneria Meccanica e Gestionale ciclo XXXVII corso attivato ai sensi del "*Regolamento dei Corsi di Dottorato di ricerca del Politecnico di Bari"*, emanato con D.R. n.286 del 01.07.2013;
3) di essere pienamente a conoscenza delle disposizioni contenute nel predetto Regolamento in merito alla procedura di deposito, pubblicazione e autoarchiviazione della tesi di dottorato nell'Archivio Istituzionale ad accesso aperto alla letteratura scientifica;
4) di essere consapevole che attraverso l'autoarchiviazione delle tesi nell'Archivio Istituzionale ad accesso aperto alla letteratura scientifica del Politecnico di Bari (IRIS-POLIBA), l'Ateneo archivierà e renderà consultabile in rete (nel rispetto della Policy di Ateneo di cui al D.R. 642 del 13.11.2015) il testo completo della tesi di dottorato, fatta salva la possibilità di sottoscrizione di apposite licenze per le relative condizioni di utilizzo (di cui al sito http://www.creativecommons.it/Licenze), e fatte salve, altresì, le eventuali esigenze di "embargo", legate a strette considerazioni sulla tutelabilità e sfruttamento industriale/commerciale dei contenuti della tesi, da rappresentarsi mediante compilazione e sottoscrizione del modulo in calce (Richiesta di embargo);
5) che la tesi da depositare in IRIS-POLIBA, in formato digitale (PDF/A) sarà del tutto identica a quelle **consegnate**/inviate/da inviarsi ai componenti della commissione per l'esame finale e a qualsiasi altra copia depositata presso gli Uffici del Politecnico di Bari in forma cartacea o digitale, ovvero a quella da discutere in sede di esame finale, a quella da depositare, a cura dell'Ateneo, presso le Biblioteche Nazionali Centrali di Roma e Firenze e presso tutti gli Uffici competenti per legge al momento del deposito stesso, e che di conseguenza va esclusa qualsiasi responsabilità del Politecnico di Bari per quanto riguarda eventuali errori, imprecisioni o omissioni nei contenuti della tesi;
6) che il contenuto e l'organizzazione della tesi è opera originale realizzata dal sottoscritto e non compromette in alcun modo i diritti di terzi, ivi compresi quelli relativi alla sicurezza dei dati personali; che pertanto il Politecnico di Bari ed i suoi funzionari sono in ogni caso esenti da responsabilità di qualsivoglia natura: civile, amministrativa e penale e saranno dal sottoscritto tenuti indenni da qualsiasi richiesta o rivendicazione da parte di terzi;
7) che il contenuto della tesi non infrange in alcun modo il diritto d'Autore né gli obblighi connessi alla salvaguardia di diritti morali od economici di altri autori o di altri aventi diritto, sia per testi, immagini, foto, tabelle, o altre parti di cui la tesi è composta.

Luogo e data Bari 07/01/2025 Firma _____

Il/La sottoscritto, con l'autoarchiviazione della propria tesi di dottorato nell'Archivio Istituzionale ad accesso aperto del Politecnico di Bari (POLIBA-IRIS), pur mantenendo su di essa tutti i diritti d'autore, morali ed economici, ai sensi della normativa vigente (Legge 633/1941 e ss.mm.ii.),

CONCEDE

- al Politecnico di Bari il permesso di trasferire l'opera su qualsiasi supporto e di convertirla in qualsiasi formato al fine di una corretta conservazione nel tempo. Il Politecnico di Bari garantisce che non verrà effettuata alcuna modifica al contenuto e alla struttura dell'opera.
- al Politecnico di Bari la possibilità di riprodurre l'opera in più di una copia per fini di sicurezza, back-up e conservazione.

Luogo e data Bari 07/01/2025_____ Firma _____

Politecnico di Bari

Department of Mechanics, Mathematics and Management
MECHANICAL AND MANAGEMENT ENGINEERING

Ph.D. Program
SSD: ING-IND/16 – MANUFACTURING TECHNOLOGY AND SYSTEMS

Final Dissertation

Development of additive manufacturing processes for multi-material metal components

by

PAOLO POSA

Referees:

Prof.

Prof.

Supervisors:

Prof. Sabina Luisa CAMPANELLI

Prof. Andrea Angelastro

Coordinator of Ph.D. Program:

Prof. Giuseppe CASALINO

Course n°37, 01/11/2021 – 31/10/2024

ABSTRACT

This thesis reports on all applications developed and published in the field of multi-material additive manufacturing with metal powders. The topics covered include several widely used technologies in the field of Additive Manufacturing (AM), such as Direct Energy Deposition (DED) and Laser Powder Bed Fusion (LPBF). The knowledge available in the literature on these categories of processes has served as a basis for the development of innovative studies and, in particular, for the optimisation, production and characterisation of artefacts consisting of metallic materials of different natures used simultaneously in the same process.

The text of the thesis has been divided into the following application categories:

1) Experiments using the LPBF process
    a) Case studies where the transition between different materials is immediate (clear);
    b) Case studies where the transition between different materials in gradual (cFGM).
2) Case studies using the DED process.

The most rigorous scientific methods available in the literature and the most advanced investigation techniques in powder metallurgy and laser processes were used in all phases of the experiments. In fact, it is possible to list the instruments used by subdividing them as shown below:

In the **design phase of the experiment**, various tools and methods are used. Bibliographic research is the first step to gather relevant information, followed by the use of statistical methods for Design of Experiments (DOE). Additionally, numerical simulations are conducted to model and predict the behavior of the system.

During the **setup phase**, the functionality and calibration of the equipment and instruments are checked to ensure they are ready for the experiment. Then, the necessary process parameters are set to perform the tests.

In the **execution phase of the experiment**, in-situ monitoring methods are used to control key process quantities (as geometrical features) and parameters. These include optical and thermal techniques, both on-axis and off-axis, to ensure that the process proceeds under the established conditions.

Next comes the **process analysis phase**, where techniques such as image analysis and control charts are used to evaluate the performance and stability of the process.

The **characterization of specimens** involves both non-destructive testing and more detailed analyses using Scanning Electron Microscopy (SEM), Electron Backscatter Diffraction (EBSD), and X-ray

Diffraction (XRD). In addition to these analyses, metallographic and mechanical characterizations are performed to determine the physical properties of the samples.

Finally, in the **conclusion phase of the experiment**, the results are analyzed to establish a correlation between the inputs and outputs using Analysis of Variance (ANOVA). Moreover, the numerical models developed during the design phase are validated.

The experiments carried out demonstrated that multi-material components produced by additive manufacturing processes are a real option, offering significant advantages in providing the optimum properties where they are required. Ad hoc fixtures were designed and built to produce test specimens on machines not designed for this purpose. In-process monitoring methods have provided important information for process optimisation, especially when analysed with appropriate statistical and image analysis tools.

SOMMARIO

In questo lavoro di tesi di dottorato sono state riportate tutte le applicazioni sviluppate e pubblicate nell'ambito della fabbricazione additiva multimateriale con polveri metalliche. Le tematiche trattate comprendono diverse tecnologie ampiamente diffuse nel campo dell'Additive Manufacturing (AM) come il Direct Energy Deposition (DED) e il Laser Powder Bed Fusion (LPBF). Le conoscenze disponibili in letteratura su queste categorie di processi sono servite da base per lo sviluppo di studi innovativi e, in particolare, nell'ottimizzazione, fabbricazione e caratterizzazione di manufatti costituiti da materiali metallici di diversa natura utilizzati contemporaneamente nello stesso processo.

Il testo della tesi è stato suddiviso secondo le seguenti categorie applicative:

1) Sperimentazioni in cui è stato sfruttato il processo LPBF
   a) Casi di studio in cui la transizione tra i diversi materiali è immediata (clear);
   b) Casi di studio in cui la transizione tra i diversi materiali è graduale (cFGM).
2) Sperimentazioni in cui è stato sfruttato il processo DED.

Per tutte le fasi delle sperimentazioni, sono stati utilizzati i più rigorosi metodi scientifici messi a disposizione dalla letteratura e le tecniche di indagine più avanzate nell'ambito della metallurgia delle polveri e dei processi laser. Infatti, è possibile elencare gli strumenti utilizzati suddividendoli come mostrato di seguito:

Nella fase di **progettazione dell'esperimento**, vengono utilizzati diversi strumenti e metodi. La ricerca bibliografica è il primo passo per raccogliere informazioni rilevanti, seguita dall'impiego di metodi statistici per il Design of Experiments (DOE). Inoltre, vengono eseguite simulazioni numeriche per modellare e prevedere il comportamento del sistema.

Durante la fase di **preparazione**, si verifica il corretto funzionamento e la calibrazione delle attrezzature e degli strumenti, assicurandosi che siano pronti per l'esperimento. Successivamente, si impostano i parametri di processo necessari per eseguire i test.

Nella fase di **esecuzione dell'esperimento**, vengono utilizzati metodi di monitoraggio in situ per controllare le quantità e i parametri chiave del processo. Questi includono tecniche ottiche e termiche, sia su asse che fuori asse, per garantire che il processo si svolga secondo le condizioni stabilite.

Segue la fase di **analisi del processo**, in cui si utilizzano tecniche come l'analisi delle immagini e l'uso di carte di controllo per valutare le prestazioni e la stabilità del processo.

La **caratterizzazione dei campioni** comprende sia test non distruttivi che analisi più dettagliate con microscopi a scansione elettronica (SEM), diffrazione di elettroni retro-diffusi (EBSD) e diffrazione a raggi X (XRD). Oltre a queste analisi, si eseguono caratterizzazioni metallografiche e meccaniche per determinare le proprietà fisiche dei campioni.

Infine, nella **conclusione dell'esperimento**, i risultati vengono analizzati per stabilire una correlazione tra gli input e gli output utilizzando l'analisi della varianza (ANOVA). Inoltre, si procede alla validazione dei modelli numerici sviluppati durante la fase di progettazione.

Dalle sperimentazioni eseguite è stato possibile verificare che i componenti multimateriali fabbricati con processi di additive manufacturing sono un'opzione concreta che offre importanti vantaggi nel fornire le caratteristiche ottimali nel punto in cui esse sono richieste. Sono state progettate e realizzate delle attrezzature ad-hoc per la realizzazione dei provini sfruttando macchine non predisposte per questo scopo. I metodi di monitoraggio in-process hanno fornito informazioni fondamentali per l'ottimizzazione dei processi soprattutto se analizzate con opportuni strumenti statistici e di analisi d'immagine.

TABLE OF CONTENTS

Chapter 1. Introduction

Additive Manufacturing (AM) is a manufacturing technology that originated in the late 1980s in the USA. It encompasses a set of techniques, according to which production takes place by aggregating layers of material. The innovation brought lies in the possibility of realising complex designs by reducing material waste, costs and production time. The first patent from '84, called SLA, involved the sintering of a photo-polymer employing a laser. SLA, however, turned out to be limited to plastic materials only and, for this reason, techniques capable of processing metallic materials were developed over time.

The Additive Manufacturing (AM) industry generated goods valued at over $11 billion in 2020. The advancement of Metal Additive Manufacturing (MAM) technologies, including Directed Energy Deposition (DED) and Laser-Powder Bed Fusion (PBF-LB), has benefited high-tech industries like aerospace, medicine, biomedical, tooling, and molding. These technologies can perform repair operations instead of replacing broken components, thereby lowering costs and pollution [1,2]. They can also build 3D components with complicated geometries without geometrical limits (e.g., molds with integrated conformal cooling channels) [3]. To enhance a surface's mechanical performance, selective coating is another option [4,5].

Thanks to additive manufacturing, it has been possible to introduce into the design phase, the possibility of making a prototype (even if the latter is a complex design) from the physical-mathematical models and computer-aided design (CAD) models made, providing the possibility of performing experimental tests on a functioning prototype [6].

In Additive Manufacturing, various materials can be used, such as:

- Metals
- Plastics
- Ceramics
- Resins

What has enabled the rapid spread of additive manufacturing is:

1. Possibility of designing components with complex shapes, improving the characteristics of the final product;

2. Reduced prototyping time and costs, as only one machine is used to make the components, and they can be produced in a single process;
3. Possibility of making parts that need to be integrated at the same time, thus reducing assembly costs.

The main disadvantages of AM, in contrast, are[7]:

4. High cost of raw materials used to build the components;
5. Low speed of manufacturing leading to difficulty in mass production of components;
6. Low level of surface finish compared to traditional manufacturing techniques;
7. High energy use due to the presence of a laser or electron beam.

ASTM International has made available a classification of AM techniques (Figure 1). These have been grouped according to the structure and bonding that the various layers have in the material[8].

Category	Operating Principle	Examples of Technology	Materials
Vat Photopolymerization (VP)	A liquid photopolymer is selectively cured in a vat by light-activated polymerization.	Stereolithography, Digital Light Processing, Continuous Liquid Interface Production	polymers, ceramics
Material Jetting (MJ)	Building material droplets are deposited selectively.	PolyJet, Multi-Jet, 3D Plotting	polymers, ceramics, composites, hybrid, biological
Binder Jetting (BJ)	A liquid binding agent is selectively deposited to bind the powdered material.	3D Printing	polymers, ceramics, composites, metals, hybrid
Material Extrusion (ME)	The material is selectively dispensed via a nozzle or an orifice.	Fused Deposition Modeling/ Fused Filament Fabrication/ Fused Layer Modelling, Robocasting/ Direct Ink Writing/ 3D Fiber Deposition	polymers, composites
Powder Bed Fusion (PBF)	Thermal energy is applied to selectively fuse areas of the powder bed.	Direct Metal Laser Sintering, Selective Laser Sintering/ Selective Laser Melting, Electron Beam Melting	polymers, ceramics, metals, composites, hybrid
Sheet Lamination (SL)	Sheets of the building material are bound with one another to form the object.	Laminated Object Manufacturing, Ultrasound Consolidation	polymers, ceramics, metals, paper, hybrid
Directed Energy Deposition (DED)	A focused flux of energy is applied to fuse materials by melting during deposition.	Laser Engineered Net Shaping, Direct Metal Deposition, Laser Powder Deposition, Electron Beam Additive Manufacturing	metals, hybrid

Figure 1 – ASTM classification of AM processes

A multi-material part consists of different materials physically distributed within it. This composition allows for the integration of various structures and functions, resulting in the possibility of combining the properties of different materials such as local wear resistance, high thermal conductivity, thermal insulation, chemical corrosion resistance, etc., to obtain a material with customised properties. The distribution of multiple materials within a part offers superior performance compared to parts composed of a single material. This feature is particularly advantageous for products that have to operate in difficult working conditions, requiring multi-functionality and adaptability to different environments.

MAM technologies can be used to process a wide range of metallic materials, including high-strength steels (like maraging steel and martensitic precipitation-hardening stainless steel) and alloys with excellent corrosion resistance (like Ti6Al4V alloy), good oxidation resistance even at high temperatures (Nickel-based alloys), and high wear resistance (WC, TiC, VC). Although

these materials perform quite well, working with them using traditional subtractive processes is very challenging. In addition, the price of these materials is typically greater than that of other materials (such stainless steels) that have strong corrosion resistance [9].

For these reasons, the technology industry has been pushing in recent years to combine different materials in a single additive process in order to produce multi-material components with superior mechanical qualities [9,10,11,12,13,14,15].

As a result, multi-material structures offer the possibility of producing integrated parts for end-use, characterised by innovative structures and multi-material layouts, to meet the growing needs in the aerospace, biomedical, automotive and mould and die sectors.

Additive manufacturing provides a solution to this challenge. With its ability to create parts layer by layer, it offers great design freedom and the possibility to manufacture complex components. In particular, multi-material AM allows precise control of material spatial distributions, opening up broad perspectives for the design and production of multi-material structures. Compared to conventional manufacturing techniques, multi-material AM offers a more reliable method for the production of geometrically complex components and can help reduce production costs.

The mechanical properties, such as tensile and flexural strength, of multi-material structures moulded with PBF-LB depend on the adhesion created at the interface between the two materials. This adhesion is influenced by the microstructures and defects present at the interface. Defects, such as porosity and cracks, can impair adhesion in these structures, while a refined microstructure at the interface can improve it.

In the PBF-LB process, multi-material structures are mainly realised using multiple discrete and composite materials. However, controlling the variation of different material compositions at specific locations is still a challenge, especially when using composite materials.

1.1 Additive manufacturing of multi-material components with PBF-LB processes

Because powder feeders coupled to the deposition head and a multi-axial robotic arm (or Cartesian system) can be used to accurately control the powders' spatial distribution and produce spatially tunable properties, DED is intrinsically more suited for multi-material fabrication [16,17]. Unfortunately, DED printed components have low surface quality and dimensional precision, which means that this technology is rarely used for multi-material AM. Rather, because of structural limitations and contamination issues, the PBF-LB process - which

produces components with superior surface qualities and higher resolution - is less appropriate for multi-material AM, particularly in systems that employ the blade/roller-based powder spreading technique [18,19].

However, combining heterogeneous materials with limited compatibility [20] and different characteristics (such as high and low melting temperatures) remains a challenge for both approaches. Additionally, there are certain drawbacks to both methods for applications involving multi-material components.

Still in its early stages, multi-material additive manufacturing has mostly focused on polymeric materials that provide industrial challenges, particularly for components that must withstand harsh environments. For example, great strength and toughness, as well as special combinations of thermal and electrical properties, are needed for nuclear reactors and current airplane turbine blades, in addition to common structural applications [21,10]. As an alternative, researchers and industry are beginning to pay more attention to recently developed metal multi-material AM since it offers the potential to address these issues. The multi-material AM (MMAM) of metallic materials is now made possible by a few AM technologies: Metal Bound Extrusion, Binder Jetting, Sheet Lamination, Laser-Powder Bed Fusion (PBF-LB), and Directed Energy Deposition (DED). Only the DED and PBF-LB methods enable the direct fabrication of metal components without the need for post-processing steps [22].

1.1.1 Multi-Material Additive Manufacturing strategies

The capacity to integrate several, often conflicting, mechanical, chemical, and physical qualities on the same structure is necessary for the majority of industrial applications, from the automotive to the aerospace and biomedical [23]. Certain components, like those with high thermal conductivity and thermal insulation, resistance to oxidation and corrosion at high temperatures but also having good mechanical strength characteristics at low temperatures, electrical conductivity, and thermal conductivity, are required to have specific, variable properties [24,25,26,27]. Because of this, creating multi-material structures is an extremely appealing task that has caught the attention of the scientific community. Nevertheless, creating a multi-material structure using a traditional manufacturing method is unreliable and severely constrained in terms of geometric complexity, precision in the spatial distribution of various elements, metallurgical compatibility of disparate components, etc.[26].

In response to these difficulties, several joining methods have been studied recently, and new printing configurations for multi-material fabrication using the PBF-LB technique have been created. In particular, three joining procedures [20] were examined: placing the third material

between two materials that need to be connected, joining the two materials directly, and joining the materials functionally graded. Even if these tactics have shown to be successful, there are still certain problems that need to be resolved: (i) the occurrence of defects like absence of fusion at the interface; (ii) the production of brittle interfaces due to the existence of brittle intermetallics; and (iii) the micropores and cracks brought on by embrittlement [28,11,29,30,31]. Regarding the newly designed printing setups, they are predicated on the utilization of in-situ powder feeders (such the DED process hoppers) that enable powder swapping between layers as needed[32,33,16]. Due to issues with material contamination, this technological approach works well for multi-material production across layers, but it is limited when it comes to multi-material fabrication inside the same layer.

1.1.2 Commercial solution for Layer-level MMAM

Layer-level multi-material components can currently be fabricated using a few number of PBF-LB methods. Among these is a prototype machine for intralayer multi-material manufacturing that was created by a research team at the University of Manchester in the United Kingdom[20]. This technological solution (see Figure 2) combines a selective powder removal system with precisely calibrated ultrasonic vibration with several nozzles to enable efficient and accurate powder adduction[34,35].

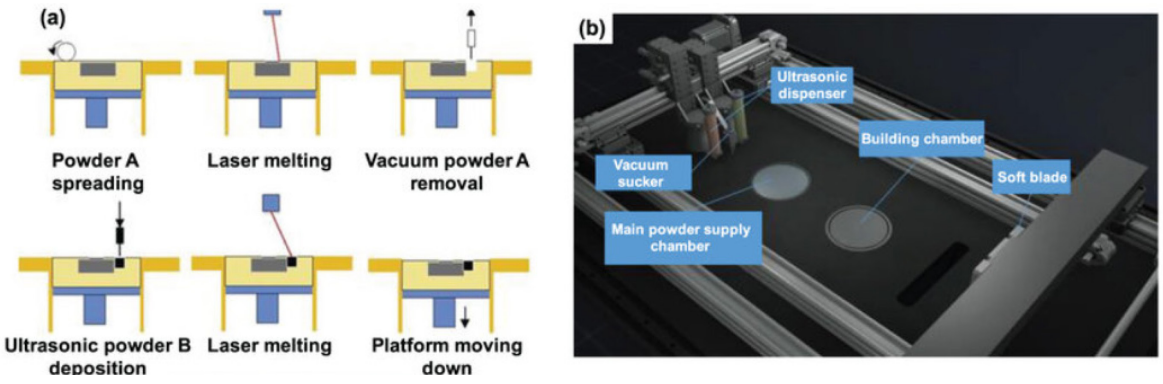

Figure 2 - MMAM prototype machine developed by the University of Manchester

By joining various metallic materials, such as Cu10Sn and Ti6Al4V [36], Invar36 and Cu10Sn [31], 316L and Cu10Sn [37], the same researchers have shown the fabricability of intralayer multi-material metal structures. They have also extended the same printing approach for metal/glass [38], metal/glass-ceramic [39], and metal/polymer [40] applications. Stronger adhesion at the interface between two materials and a lower number of fabrication errors were achieved in earlier studies.

Furthermore, Aerosint SA has developed a machine named "Selective Powder Deposition," which is a commercially viable PBF-LB system that facilitates multi-material intralayer fabrication [22]. Through selective powder voxel deposition, this electrophotographic device effectively fabricates complicated shapes (see Figure 3). Unfortunately, most engineers cannot afford this technology due to its higher complexity and price [41].

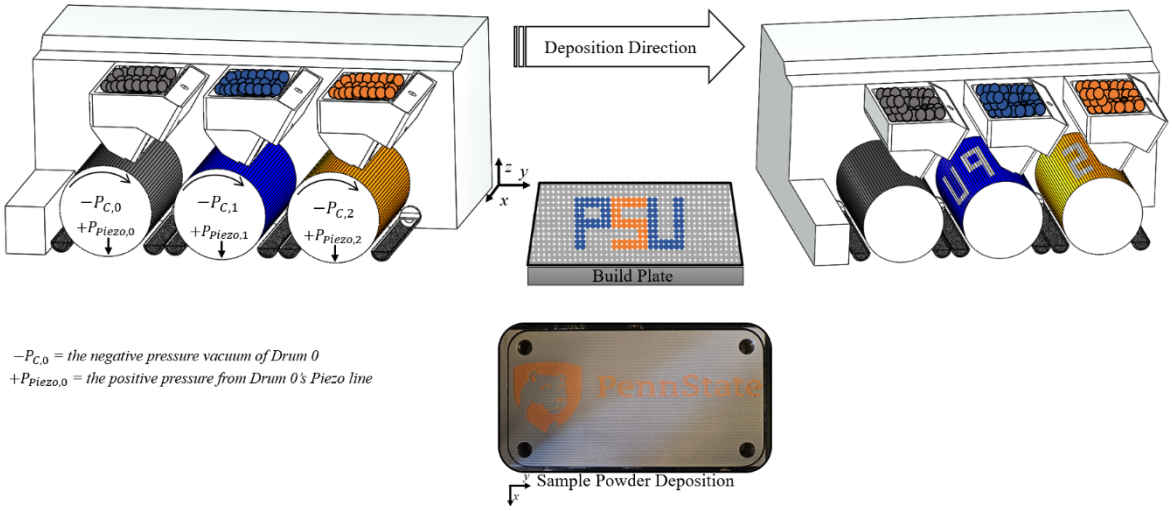

Figure 3 - Schematic of the Aerosint MMAM solution

However, there is still a issue to be solved: could intralayer multi-material selective laser melting procedures be carried out on existing conventional machines? If so, this would lower the development costs of multi-material AM technology. One approach may be to create machinery that expands the range of procedures that can be carried out using PBF-LB techniques for the systems that are now in use (such those that use a blade- or roller-based powder spreading technique). Blade-based methods can be readily adjusted for between-layer multi-material fabrication, as evaluated by Wang et al. [41], but intralayer multi-material manufacture is still difficult.

Recently, a team of researchers joined a nickel-based superalloy and a stainless steel alloy using a traditional blade-based PBF-LB system in a novel layer-level multi-material manufacturing process [42].

Many publications have been released on the topic of additive manufacturing of multi-material components using the PBF-LB technique. It has been possible to create a variety of multi-material structures using different printing techniques. These include: (i) multi-material substrate-embedded structures, which are made of a substrate made of one material with an PBF-LB part of another material manufactured on it; (ii) multi-material structures made by

manually replacing two different powders; and (iii) multi-material structures created using specialized in-situ powder feeding systems (hoppers) (see Figure 4). [41,43,44,45,46,16].

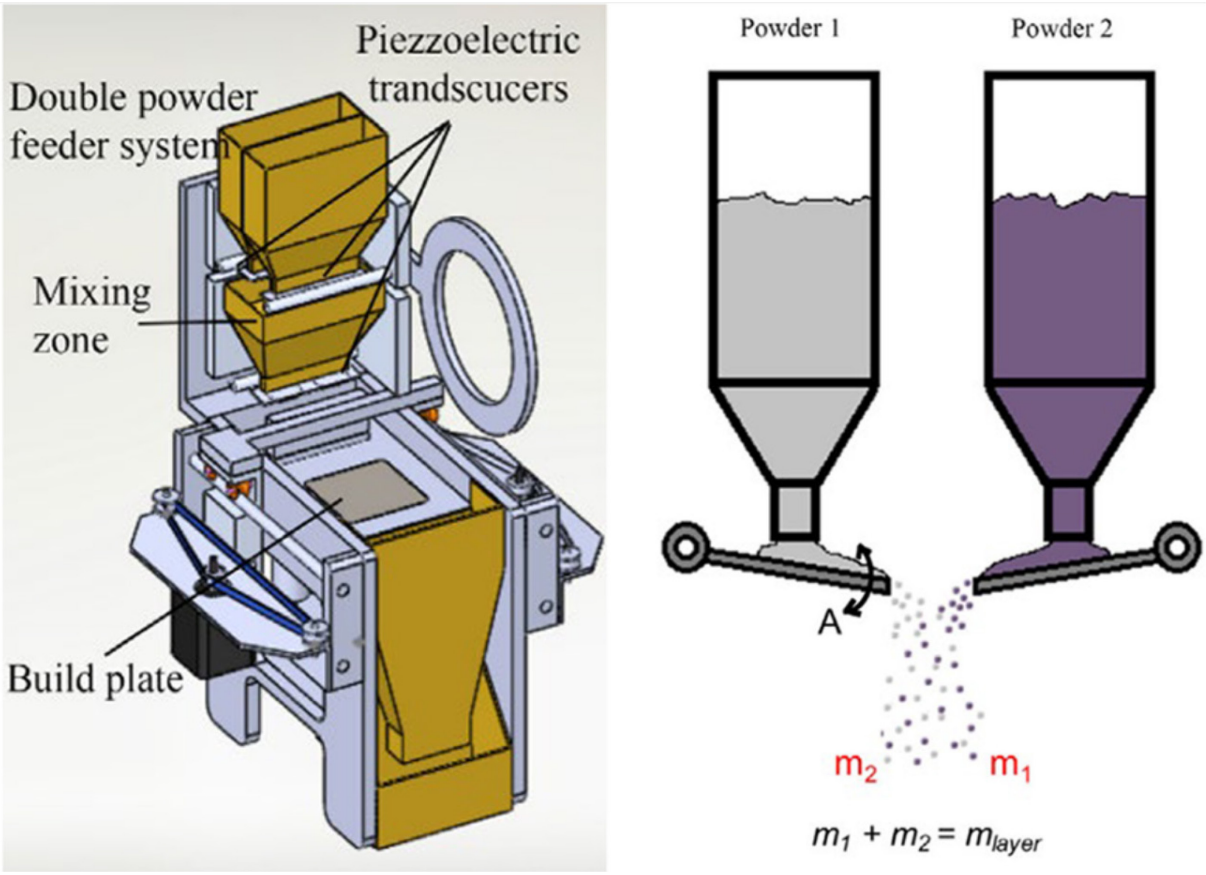

Figure 4 - Multi-hopper equipped machine for powder bed spreading

The latter has shown to be the most adaptable as it enables the creation of multi-material structures that are both intralayer and interlayer, contingent on the distribution of the various materials [41]. However, very few studies have been done on the fabrication of intralayer multi-material parts, even though many have been done on the fabrication of interlayer multi-material components.

1.1.3 Powders cross-contamination issue

Configuring powder feeding systems can be challenging and it is necessary to prevent contamination between different powders. Recently, Wei et al. [18,37,35,40] created an extremely intricate PBF-LB machine that combines a traditional powder bed coating, a selective powder removal system, and a feeder with multiple nozzles to replace removed material with a different powder before laser scanning. This allows for the fabrication of intralayer multi-material structures. Additionally, Aerosint SA has created a multi-material 3D printing technique known as "Selective Powder Deposition" that enables the deposition of many powders to create a single layer comprising a minimum of two materials. This technique may

provide an intralayer distribution of heterogeneous materials by enabling the selective deposition of powder voxels [41,47]. Although it involves a larger level of machine complexity and cost, it may be quite successful in realizing complicated shapes.

During multi-material fabrication, cross-contamination in Laser-Powder Bed Fusion (PBF-LB) techniques can significantly affect part quality and powder reuse. The impact of metal powder cross-contamination on component characteristics and the barrier to powder reuse in PBF-LB processes have been the subject of numerous research. The impact of metal powder cross-contamination of CuCr1Zr in AlSi10Mg during multi-material laser-based powder bed fusion was examined by Horn et al. [48], highlighting the significance of comprehending and controlling cross-contamination for preserving part characteristics. Furthermore, the implications of the laser-metal powder interaction in PBF-LB are discussed in a publication by Santecchia et al., wherein the possibility of powder contamination through this contact—which can result in cross-contamination—is highlighted [49]. Additionally, a study notes that one of the main drawbacks of multi-material PBF-LB approaches is the possibility of powder contamination [50], highlighting the necessity of successfully separating various powder species in order to avoid cross-contamination and permit the widely used and cost-effective implementation of multi-material PBF-LB processes [51]. Since it doesn't result in flaws in the components that are created, it can be considered that a certain amount of contamination between materials can be allowed. This implies that part quality may be considerably affected by a certain amount of cross-contamination and yet be tolerated. It is noteworthy, therefore, that because to the unpredictable impact of contaminations on component quality, contaminated powder feedstock continues to provide a significant difficulty in PBF-LB [52]. Material cross-contamination has the potential to negatively alter the additive manufacturing (AM) part's microstructure and, as a result, its functional qualities [53].

Several in-process monitoring strategies have been studied to identify cross-contamination in Laser Powder Bed Fusion (PBF-LB) processes. These methods use data from in situ sensors along with other techniques to try and pinpoint the exact moment when material cross-contamination starts. Optical monitoring using photographic equipment to record visible spectrum radiation generated by materials interacting with a laser beam is an efficient technique [42].

Powder Bed Fusion-Laser Beam (PBF-LB) technique is now one of the most promising candidate technologies for metal additive manufacturing (AM) that can produce multi-material parts with high complexity, precision, and performance [54]. Therefore, getting multi-material

PBF-LB processing to the same level as single-material PBF-LB businesses is of tremendous importance to both academia and industry [20]. Various methodologies and printing configurations have been investigated to tackle the difficulties associated with multi-material fabrication in the PBF process. The literature looked into three distinct approaches: using a third transitional material as an interlayer between the two materials of interest, creating a sharp interface by directly fusing the two materials, and creating a functionally graded transition by gradually mixing the two materials [20,54]. The development of brittle interfaces, the existence of flaws at the interface, and the emergence of micropores and cracks are among the issues that still exist despite their efficacy [55,56,57,58,59]. New printing configurations that rely on in-situ powder feeders are limited at the layer level due to contamination concerns, but they are helpful for multi-material fabrication between layers (i.e., switching to a different material after a predetermined build height) [16,32,33]. Multiple materials within a single print layer, also known as intralayer, can only be produced at the layer-level by a limited number of PBF machines at the moment. Specifically, two technologies now on the market are capable of producing multi-material intralayer components [20,22]. However, the majority of engineers cannot easily access either of these prototype solutions due to their complexity and cost [41]. By suitably altering conventional PBF systems (blade-based and powder platform from below), Errico et al. [60,42] have recently shown the manufacturability of intralayer multi-material components, avoiding contamination difficulties that hindered their development [41]. Although previous research on the subject has focused on the material interface [42,61] and bi-material specimen tensile testing [60], this is the first study to use the intralayer approach to examine functional engineering components like lattice structures.

1.1.4 Multi-material lattice structures

Presently, the methods that enable the creation of multi-material parts are diffusion bonding and conventional welding, both of which have considerable drawbacks when it comes to producing parts with intricate geometries and which even after heat treatment inevitably result in residual stresses and microstructure alterations [62,63,64]. AM is a desirable alternative for multi-material manufacturing since it enables the creation of complicated multi-material parts [54], as well as the reduction of weight and solving of assembly-related problems through assembly consolidation [65,66]. The ability of multi-material components to extend the capabilities and functionality of a single component as well as the capacity to design and create ad hoc components to meet specific needs or purposes have had an impact on a number of engineering domains, including automotive, aerospace, medical, motorsports, industrial, and energy [67,68]. More effective goods can be made by combining several components. A number of

effective applications have involved combining materials with good thermal insulation qualities with those that conduct heat well, resulting in the creation of components that aid in lowering energy consumption across a range of industries, including the building and automotive sectors [40]. The fusion of particular and distinctive thermal and electrical properties with attributes like great strength and toughness [10,69]. Furthermore, multi-material components have the potential to significantly contribute to a future that is more sustainable [70]. For instance, employing robust yet lightweight multi-material components in a car could result in lower CO2 emissions and better energy efficiency [54].

As was previously indicated, AM makes it possible to deeply customize and use complicated geometries like lattices, which are currently widely investigated and used in a wide range of applications. This covers heat transfer issues with heat sinks [71,72,73] and heat exchangers [74,75], as well as structural issues with lightweighting [76,77,78] and energy absorption [79,80,81]. It also covers porous structures in orthopedic devices [82,83]. This has involved studying the mechanical and thermal characteristics of various lattice geometry variants as well as modifying and customizing the structure as needed [84,85]. By permitting variations in the parent material, multi-material additive manufacturing techniques offer even more customization options for lattice designs, opening up an even wider range of possible features and uses.

The use of multi-material lattices approach is suggested because this could be especially useful in situations where a uniform geometry or density is needed, or if specific material characteristics are needed in specific areas. Due to the wide range of applications for which lattices are used, designers frequently strive to optimize lattices for multiple objectives at once. Additionally, multi-material lattices increase the range of properties that can be achieved in graded lattices despite limitations like manufacturing constraints and lightweighting objectives. Polymer methods such as material jetting [86] and material extrusion [87,88] have been used to study various AM multi-material lattice varieties. These technologies have included mixtures of soft polymers like TPU with tougher materials like ABS/PLA. Regarding metal structures, a variety of composite structures have been produced using hybrid techniques by using casting, foaming, and injection molding to fill the pores in AM lattices with a matrix material [89,90,91]. Studies on multi-material metal lattices, on the other hand, where each component is created concurrently in a single process, are scarce. Ti6Al4V lattices with gradients in TiB2 concentration were fabricated and evaluated by J. Zhang et al. [92], and multi-material Ti6Al4V/AlCuMg lattices with a Cu interlayer to avoid cracking along the interface were produced [54]. Multi-material metal lattices with maraging steel, cobalt chromium, 316L, and

copper tin have also been studied by M. Zhang et al [93,94]. Research on multi-material lattice variations is needed to examine the material interface, behavior, and prospective applications of these techniques, which are becoming more and more popular.

1.1.5 MMAM for Functionally Graded Materials (FGM) structures

The creation of functionally graded materials (FGMs), which result in a smooth fluctuation of characteristics because of their graded interfaces, has been the solution to this issue [95,96,97]. The literature classifies FGMs based on a variety of factors, including manufacturing methods (conventional, non-conventional, and advanced), material composition (ceramic/ceramic, metal/metal, metal/ceramic, etc.), type of gradation (continuous and discontinuous), and others. These factors are covered in detail in a number of research studies [98,99,100,101,102].

The most widely used field of advanced manufacturing techniques for producing functionally graded structures is Additive Manufacturing (AM) [103]. Like traditional techniques, advanced manufacturing approaches fall into a few categories. Metal Bound Extrusion, Sheet Lamination, Powder Bed Fusion - Laser Beam (PBF-LB), and Directed Energy Deposition - Laser Beam (DED-LB) are the ones that are currently utilized in FGM AM fabrication. Of these, only the DED-LB and PBF-LB procedures provide direct metal component manufacturing without the need for post-processing steps like metal infiltration to achieve full density, thermal sintering, and polymer binder removal [104,105]. Both approaches, however, have drawbacks when it comes to applications involving FGM components. Due to its ability to use flexible powder feeders, which allows for precise control over powder distribution for spatially tunable properties, the DED-LB has inherent advantages for FGM fabrication; however, its adoption for FGM AM is limited by the low dimensional accuracy and surface quality of its printed components [17]. On the other hand, because of structural limitations and contamination concerns, the PBF-LB process—which may create intricate geometric components with better surface qualities and resolution—is less appropriate for FGM AM, especially when blade-based powder deposition techniques are involved [104,25,49].

Using the PBF-LB technique, innovative print combinations have been created to get over these challenges in the manufacturing of FGM [26]. These configurations make use of in-situ powder feeders, which are comparable to the hoppers used in the DED-LB process. The powder flow controller controls the rate at which powders are deposited once they are mixed. For instance, Wang et al. effectively produced a four-material FGM component made of CoCr/18Ni300/CuSn10/316L in series using this novel arrangement [106]. The risk of contamination between different materials and structural limitations that prevent controlling the

functional gradation between materials within the same layer limit the applicability of this technological solution, even though it is effective for manufacturing FGMs across different layers [18]. At the moment, only a small number of PBF-LB machines are capable of layer-by-layer fabrication of FGM components. Interestingly, intralayer FGM production is made easier by a prototype machine developed by a research consortium at the University of Manchester (UK) [25,20]. This technological innovation combines several nozzles, a mechanism for powder removal, and precisely calibrated ultrasonic vibration to deliver powder precisely and efficiently. By mixing various materials, such as metal/metal (316L/Cu10Sn), the researchers have shown that it is feasible to fabricate FGM metal structures. They have also extended the same printing approach to metal/glass[38] and polymer-metal/ceramic [40] applications. Moreover, the intralayer manufacturing of FGMs is made possible by a commercially available PBF-LB equipment called "Selective Powder Deposition," which was created by Aerosint SA [47]. This electrophotographic technique deposits powder voxels selectively, enabling efficient synthesis of complex shapes. However, the solutions that are now being found in academic research and business need the development of new machinery, which adds to the complexity and cost. Because of this, most people cannot afford these creative solutions. Still unresolved is the challenge of establishing intralayer FGMs selective laser melting techniques with existing conventional machinery, which offers a potential avenue to reduce costs associated with FGM AM technology development.

Building machinery that improves the performance of currently operating systems, such as blade/roller-based powder deposition systems, is one potential tactic to expand the scope of applications that can be executed with PBF-LB. A group of scientists recently joined a stainless steel alloy with a nickel-based superalloy to create new tools for intralayer bi-material fabrication utilizing a conventional blade-based PBF-LB system[42]. Furthermore, the same method was applied to create layer-level bi-material specimens of AISI 316L and 18Ni Maraging 300 [60].

There are two types of FGMs: continuous and discontinuous. Whereas in the latter case (cFGMs), the spatial variation in composition and characteristics happens continuously, in the former case it follows a discrete stepwise pattern [107,108]. The two most popular powder-based AM processes for creating multi-material structures are Directed Energy Deposition – Laser Beam (DED-LB) and Powder Bed Fusion – Laser Beam (PBF-LB) [9,25]. Additionally, since layer-by-layer construction is a common practice in additive manufacturing, the majority of research has concentrated on structures where the spatial variation of the composition is along the build direction, particularly when employing DED-LB; studies where this is within

the layer and using PBF-LB, on the other hand, are less common and have only recently come to light [9,25,109,60,42].

1.1.6 Residual stresses in MMAM fabrication

Using a laser source, PBF-LB melts the powder in a highly localized manner to create a melt pool, which quickly solidifies to create a three-dimensional part layer by layer. However, a complicated and sizable residual stress field is created as a result of the material being subjected to numerous heat cycles and highly steep thermal gradients, which can also lead to the failure of the manufacturing process [110,111]. Inadequate analysis and control of residual stresses can lead to process cracking, detachment from the build platform, and considerable deformation in the finished product [9,110,111,112]. Additionally, they have a significant impact on the fatigue characteristics of AM components, necessitating the need for heat treatments or post-process machining to enhance their mechanical behavior [113,114,115].

Furthermore, numerous researchers have already identified the difficulties associated with the development of multi-materials. One of the key obstacles is in producing components that combine metal alloys that do not mix well, such as those that can be differentiated by toughness and hardness. This is because the different interface between these alloys can induce the production of weak metal connections, thermal stress accumulation, solubility issues, and inconsistencies in thermal properties. FGMs offer a possible answer to these difficulties, as they allow a smooth transition of characteristics, eliminating sudden changes at the interface [98,116]. Given their great capabilities FGMs are proven to be particularly beneficial in industrial settings (aerospace applications, energy industry, biomechanical applications, automotive industry, maritime applications, etc.).

Several materials have been mixed and tested to make FGMs [117,118,99,101]. For example, parts can be obtained with a lighter core, while the exterior can be formed of a different material compatible with the environment in which the part will be utilized, avoiding abrupt changes in chemical composition and mechanical properties [100]. In aerospace contexts, there are many situations where a gradient transition between materials is required to reduce thermal stresses, for example, in jet engine components that experience high temperature gradients; in this case, the use of the stainless steel-SS316L/superalloy-Rene88DT combination was decisive [119,120].

However, research of great interest related to FGM fabrication is the investigation and characterisation of powders employed in the process. The characterization of metal powders used in PBF-LB processes is a topic that many studies have addressed to determine the

connections between the measurable and observable qualities of the particles prior to melting and the quality of the fabricated components. Hilzenthaler et al. studied the characterisation of virgin and recycled steel powders by morphological, chemical, mechanical, and electrical investigations [121]. Among other results, they confirmed that a greater powder particle size results in higher flowability, as was proven in prior work [121,122]. The mechanical properties of the components were likewise connected to the powder particle size in the instance of 17-4 PH steel. The results suggest that the optimal characteristics are obtained when the particle diameter is in the range of 20÷40 μm [27]. It is likely that the varied physical, chemical, and geometric properties of different powders affect the way they interact during the spreading phase from the powder chamber to the construction platform.

Several investigations, performed with more complicated spreading systems not based on a coater or roller, have proven the possibility of powder bed laser processing on diverse materials combined in the same layer and have explored the metallurgical qualities of the produced parts [123,16,37]. Demir and Previtali, exhibited the ability to make FGM (Fe/Al-12Si) components using a prototype PBF-LB machine that allows two different powders to be mixed with variable percentages, according to the manufacturer's requirements, and distributed from the top utilizing hoppers. This is the case for FGM components between layers, i.e., along the Z-axis of the structure [16]. While Wei et al. demonstrated the capacity to create FGM components inside the same layer. In this investigation, 316L/Cu10Sn materials were mixed utilizing a prototype machine patented by the same research group. The prototype system comprises of a selective multiple powder distribution system (up to 6 distinct materials) functioning through programmed ultrasonic vibrations, paired with a selective powder removal mechanism [37]. The latter is the case for FGM components layer-level.

Regarding systems using the coater or roller for powder bed spreading, some studies have attempted to use numerical simulations to infer the influence of powder particle size and flowability on the manufactured samples [124,125]. However, numerous data obtained have been irrelevant due to the substantial experimental restrictions connected with this production process, such as contamination concerns as stated extensively in the literature [49].

According to Mercelis and Kruth in [126], the temperature gradient mechanism (TGM) and the cool-down phase are the two mechanisms responsible for the start of residual stresses in AM. The generation of residual strains resulting from the significant temperature gradients surrounding the laser spot is defined by the TGM. Following laser passage, a compressive region encloses the irradiated area, which is characterized by tensile stresses. Conversely, the

cool-down phase is linked to the molten top layer's shrinking, which is limited by the solid material beneath it during solidification. This causes compression in the layers beneath and tensile tensions in the higher layer. Furthermore, the complexity and amount of the residual stresses, in addition to the part's manufacturing, are greatly influenced by the process parameters that are employed, as well as the size, geometry, and characteristics of the material [110,111,127,128,129,130,131,132,133,134]. To create a fully dense part while reducing residual stresses, laser power, scan speed, and scan method must be tuned; these factors also rely on the kind of material [110,132,135].

Even when all metallic AM technologies are taken into account, there is a dearth of analysis about the contextual residual stresses generated, despite the fact that studies on the fabrication of FGM structures have been steadily increasing. The literature, in particular, does a poor job of reporting residual stress measurements on FGM specimens. With five distinct DED-LB discontinuous between-layer FGM ferritic-austenitic steel specimens, Woo et al. assessed the through-thickness residual stress field using a variety of methods [109]. They discovered that when the number of interlayers increased, the stress trend adopted a sinusoidal pattern when a bidirectional scanning technique was used. Furthermore, a notable shift from tension to compression is noted, reaching up to 950 MPa, as a result of the substantial difference in the thermal expansion coefficient between the totally austenitic composition and the 50% austenitic and 50% ferritic composition. The residual stress range, however, dramatically decreases to roughly 430 MPa when the scanning approach is changed to orthogonal or island scanning, and the stress profile throughout the thickness (direction of composition change) resumes a smoother trend. In order to forecast residual stresses and distortion in FGMs made by DED-LB, Shan et al. created a multiscale framework based on the inherent strain approach in a later study [136]. Using a computer model, the scientists expanded on the previous study [109] and discovered that reducing distortion in the final portion and mitigating residual stress oscillations by using nine interlayers. This shows that the residual stress field becomes more uniform when continuous composition variation, or cFGMs, is adopted. Moreover, combining this effect with an island scanning approach lowers the residual stress range across the thickness. Similar findings were reported by Ghanavati et al. [137], who used DED-LB to create a between-layer multi-material SS316L-IN718 structure and adopted a smoother compositional transition to mitigate abrupt changes in residual stress. Li et al. discovered that employing Inconel 718 and AISI 316L buffer layers in multi-material Cu depositions on AISI 304L using DED-LB led to defect-free copper and a decrease in the maximum tensile residual stress [138]. In their study, Shin et al. used three interlayers, each measuring 5 mm, to quantify solely the surface residual

stresses by X-ray diffraction in steel FGM specimens made by DED-LB, in which the composition varied along the build direction from completely ferritic to austenitic [139]. A computer model for residual stress analysis of between-layer TC4-Inconel 718 FGMs has been established by Zhao et al. [140]. Nevertheless, the typical PBF-LB process characteristics, which produce distinct residual stress fields, were not taken into consideration in their work, and within-layer FGMs were specifically overlooked. A seamless transition from AISI 316L stainless steel to Inconel 625 FGM was achieved by Rodrigues et al. using wire and arc additive manufacturing in increments of 5% composition changes [141]. By measuring residual stresses with neutron diffraction, the FGM specimen showed higher values than a straight transition between the two materials. This outcome was brought about by the increased production of harmful precipitates in FGM, which led to volumetric mismatches and increased residual stresses at the end. A between-layer AISI 316L-Inconel 625 cFGM specimen was created by Bodner et al. [142] utilizing a brand-new deposition method known as liquid dispersed metal PBF. The residual stresses, according to the scientists, showed a C-shaped profile across the specimen's thickness, with superimposed variations at the material interfaces. The residual stresses in a multi-material structure with both between-layer and intra-layer changes of these materials that was constructed using the same technology were then measured by the same authors [143]. As a result of the process, extremely large residual stresses - even reaching 900 MPa - developed. Furthermore, stress concentrations were noted at both between- and intra-layer material transitions. To the best of the authors' knowledge, no research has measured the residual stresses in FGMs produced using PBF-LB. Additionally, only Rodrigues et al. examined a structure with smooth composition variation; however, because of the large number of precipitates, they produced an unexpected outcome with a direct interface that outperformed FGM; as a result, smooth composition variations unquestionably need more research [141]. Furthermore, the analysis of residual stresses in an intra-layer multi-material structure was limited to Bodner et al. [143]. It has only been recently shown that it is feasible to manufacture these layer-level FGMs using PBF-LB, and there is still a dearth of contextual residual stress characterization in the literature. The construction direction has a major impact on the mechanical properties of specimens made using additive manufacturing [144,145]. This also holds true for the manner in which FGMs' material composition varies. Consequently, the measurement of residual stresses cannot be easily deduced from similar research on PBF-LB produced samples with several layers and materials. Lastly, the impact of process factors unique to a certain material on residual stresses in FGM constructions was not examined in any of the research mentioned above.

1.2 Additive manufacturing of multi-material components with DED processes

MMAM technologies can be used to process a wide range of metallic materials, including high-strength steels (like maraging steel and martensitic precipitation hardening stainless steel) and alloys with excellent corrosion resistance (like Ti6Al4V alloy), good oxidation resistance even at high temperatures (like nickel-based alloys), and high wear resistance (like WC, TiC, and VC). Although these materials perform quite well, using traditional subtractive techniques to work with them proves to be exceedingly challenging. Additionally, these materials are typically more expensive than other materials with strong corrosion resistance (such as stainless steel)[9].

For these reasons, the technology industry has been pushing in recent years to produce multi-material components with enhanced mechanical qualities by combining different materials in a single additive process[15,14,13,12,59,146,9].

For instance, to build a component using the DED technique, Ben–Artzy et al.[147] investigated the viability of combining two incompatible metals (300 maraging steel/SS316L). To prevent the development of brittle intermetallic phases, they specifically investigated the interface zone between the materials and created a functionally graded transition. Using DED technology, Aydogan and Sahasrabudhe[148] created a multi-material T800 + NiCr component with varying NiCr percentages to enhance the manufacturability of a Co-based superalloy and lessen the likelihood of brittle fracture and crack development. Multi-material PBF-LB, on the other hand, is one of the most promising for metal applications.

To enhance the surface performance of hot-rolled or cast components, several studies have been conducted on the application of the DED technique for ad hoc coating[4,2]. For instance, Félix—Martínez et al.[149] investigated how process variables affected the DED coating's microstructural characteristics on 18Ni-300 maraging steel. The findings demonstrated that some process variables, such as energy density, had a significant impact on the coating's final microstructural and geometrical characteristics.

Nowadays, the manufacturing sector views obtaining or restoring surfaces with superior mechanical performance as a need rather than just a preference. This requirement results from the industry's dedication to three key goals: efficiency, sustainability, and competitiveness. Reducing processing waste and extending the usable life of manufactured components are two possible steps in the pursuit of sustainable products and processes [150]. Because of this,

attaining or restoring surfaces with superior mechanical performance is essential, particularly when working with intricate geometries like interior components or regions that are off-limits to conventional tools [150]. This highlights the significance of such research by extending component durability and reducing waste.

Exploring this field with the Directed Energy Deposition-Laser Beam (DED-LB) technology is very beneficial [5,151]. There are a lot of advantages to this process over conventional methods. First off, it minimizes distortion and thermal impact by efficiently shielding the base material from deterioration through its localized heat input [152]. Second, the quick cooling rates of DED-LB lead to the development of finer microstructures, which enhance the mechanical properties of the material [153]. Furthermore, the method prevents any chemical alterations in the coating composition by regulating substrate dilution and ensuring a robust metallurgical link between the substrate and coating [154]. In addition to improving flexural strength, this regulated bonding keeps the coating from coming off [155]. Furthermore, DED-LB eliminates structural or physical constraints to allow coating of surfaces that are generally difficult to access with conventional techniques.

However, the DED-LB technique's material diversity is one of its main advantages when it comes to producing coatings with exceptional mechanical qualities. In particular, the DED-LB technique can strictly controllably and dynamically change the feedstock material's composition throughout manufacturing [156,157]. Because of its special quality, it is at the forefront of materials research and development, enabling the creation of multi-material structures right at the fabrication stage [9]. Advanced materials like metal matrix composites (MMCs), functionally graded materials (FGM), and high entropy alloys (HEA) can be processed thanks to this capability [158,159]. For coating applications that seek to improve mechanical performance, ceramic-reinforced metal matrix composites are especially beneficial [160,161]. In fact, because each ingredient contributes a distinct property, ceramic-reinforced MMCs have improved material characteristics [162]. For example, the metal matrix's high toughness and ductility are complimented by the ceramic phase's high hardness and advantageous strength-to-weight ratio [160,163]. Moreover, ceramic reinforcements minimize wear of the metal phase by acting as dislocation barriers and counteracting plastic deformation [164]. Superior strength, hardness, and resistance to wear, corrosion, and high temperatures are just a few of the remarkable qualities that ceramic-reinforced MMCs typically display [164]. Because of these qualities, composite structures are adaptable solutions that may be used in a variety of industries, including mining, oil and gas, machining, aerospace, and agricultural [154,165,166,167]. Notably, two types of DED-LB for MMCs are distinguished in the scientific

literature according to the strategy used to reinforce phase development. In ex-situ manufacture, matrix and reinforcement powders are pre-mixed with exact volume fractions; this may cause the ceramic phase to dissolve partially or completely. Conversely, in-situ production comprises the synthesis of alloys in which the hard phases have completely broken down and are distributed throughout the matrix [156]. Nevertheless, controlling the ceramic phase's dissolution in ex-situ manufactured metal matrix composites (MMCs) is a very difficult task that continues to be a major obstacle in ongoing research. One of the primary innovations of this study is also this [168]. Cracking, uneven dispersion of the reinforcement phase, or insufficient adhesion between the components are frequently the result of the partial or complete dissolution of the ceramic reinforcement within the metal matrix, which creates complex hierarchical structures at the interface [169].

The evolution of the mechanical (wear resistance, hardness) and microstructural properties of MMC composites has been examined in a number of research published in scholarly journals. A number of research examine the effects of DED-LB process parameters, while others focus on the effect of material selection (reinforcement, matrix), and the percentage of reinforcement inside the matrix.

The compatibility of the reinforcement and matrix chemicals must be taken into account while choosing materials for MMCs. The characteristics of the finished product are greatly impacted by this compatibility. In a thorough investigation comparing various reinforcement and matrix materials, Nurminen et al. discovered that materials with close chemical affinities promoted the breakdown of the ceramic phase. The ultimate coated product's mechanical performance may suffer as a result of this breakdown [170]. Additionally, research by Zhang and Kovacevic, Jiang and Kovacevic, Bartkowski and Bartkowska, and Adam et al. has looked at how different reinforcements (VC, TiC, WC, SiC) affect the tribological characteristics of coatings made of metal matrix composite (MMC). The advantages of employing MMC composites for surface hardness augmentation and anti-wear coatings are demonstrated by these investigations. For high temperatures and harsh service conditions, it's crucial to choose Ni- or Co-based matrices [154,171,172,173].

Furthermore, the effect of the amount of reinforcement on the final qualities of coated items has been the subject of multiple research. The weight proportions of typical MMC coatings, which use pre-mixed metal and ceramic powders, range from 1 to 20% [174]. Hardness increased gradually when the volume fractions of WC in a Fe-based matrix rose from 0% to 20%, according to Li et al. [175]. In a study on WC-MMC wear resistance, Xie et al. discovered

a significant correlation between MMC reinforcement content and wear resistance [176]. Similar results of better tribological and hardness qualities with increasing reinforcing percentage were also reported by Zhao et al. [177] and Raahgini et al. [162]. The development of carbides, grain refinement, and the existence of unfused reinforcement particles scattered throughout the metal matrix have all been linked to the increase in these properties. Studies have indicated that augmenting the proportion of reinforcement, surpassing 20%, can result in additional enhancements to the ultimate characteristics of the MMC coating, particularly for tribological efficacy, durability, and hardness [168]. Nevertheless, embrittlement may result from an overabundance of reinforcement and uncontrolled disintegration of the reinforcement inside the matrix, which may cause degradation and the eventual loss or detachment of particles from the MMC coating [165]. Increasing the proportion of ceramic compounds in the deposits actually causes the total hardness to rise, according to multiple studies [178,179,180]).

Ostolaza et al. carried out preliminary research on the impact of DED-LB process parameters on the mechanical characteristics and microstructure of MMC coatings [155,181]. Important information about how interaction time affects ceramic particle dissolving was obtained from the study. Extended exposure to elevated temperatures caused the ceramic particles to dissolve more readily, resulting in a final matrix that was richer in W phase and had better tribological qualities. On the other hand, over-dissolution might cause degradation. Furthermore, because of grain refinement, a rapid deposition rate may help achieve better ultimate mechanical properties [181,155].

Scientific knowledge on the viability of applying a DED coating using different materials to a component generated by PBF-LB is still lacking, though. This option can be extremely important for the manufacturing of tools and molds since it enables the use of a more expensive material with better properties for the necessary surfaces and a less mechanically performing and less expensive material for the core. When compared to the existing method of making a component made solely of tool steel, this would result in a reduction of production costs.

For instance, in order to fabricate a component using the DED technique, Ben-Artzy et al. [147] investigated the viability of combining two incompatible metals (SS316L and 300 maraging steel). To prevent the development of brittle intermetallic phases, they specifically investigated the interface zone between the materials and created a functionally graded transition. Through the use of DED technology, Aydogan and Sahasrabudhe [148] created a multi-material T800 + NiCr component with varying ratios of NiCr to enhance the manufacturability of Co-based superalloy and lessen the likelihood of brittle fracture and crack development. However, multi-

material PBF-LB appears to be one of the most promising for metal applications. For example, Demir et al. [33] used a novel PBF-LB machine with a double hopper to combine two austenitic steels, AISI 316L and Fe35Mn, to create a multi-material gradient structure. This process can be used to produce components with intricate geometry that need mechanical properties in particular zones. However, because of the dramatic fluctuation in the material's physical properties, PBF-LB still requires a great deal of research to determine whether processing faults are present [20].

Additionally, creative methods like Hybrid Additive Manufacturing (HAM) have been looked upon. For instance, a novel hybrid manufacturing method combining subtractive and additive technologies was investigated in the work of Samei et al. [3] in order to construct an AISI 420/Corrax component for use in plastic injection molding. They confirmed that it is possible to produce economically priced dies that are stronger, more corrosion resistant, and more intricately contoured cooling channels than traditional dies.

Furthermore, a number of studies have been conducted on the application of the DED technique for hot-rolled or cast component ad hoc coating in order to enhance surface performances [2,4]. For instance, the impacts of treatment parameters on the microstructural characteristics of a DED coating of 18Ni-300 maraging steel were investigated by Félix-Martínez et al. [149]. The findings demonstrated that some process variables, such as the energy density, had a significant impact on the coating's final microstructural and geometrical characteristics.

Nonetheless, there are still technical gaps regarding the viability of applying a DED coating utilizing different materials on a component created via PBF-LB. This option can be extremely important for the manufacturing of tools and molds, enabling the use of a more expensive material with better properties for the necessary surfaces and a less mechanically performing and less expensive material for the core. As opposed to now, when producing a component made entirely of tool steel, this would result in lower production costs.

1.2.1 Layer-level MMAM with L-DED process

Within the framework of L-DED processes, there are few studies on the fabrication of multi-material components at the layer level. One of them, conducted by Jin et al., develops a lamination method for combining different materials by LDED technology with the aim of creating defect-free multi-material joints [182]. These researchers designed various geometries, such as V-shaped joints and anchors, to optimize the mechanical bond between dissimilar materials and fabricated them using LDED and tensile testing to evaluate the mechanical properties and strength of the joints. In this way, they were able to determine the influence of

geometry by finding that the direction and angle of rolling significantly influenced the formation of defects such as pores and cracks. In addition, it was observed that lower angles, such as the 30° V-angle design, showed better joint quality than higher angles, and that anchor joints showed good strength in vertical specimens but problems in horizontal specimens [182]. Mechanically, however, the study concluded that vertically rolled specimens exhibited ductile fracture and superior performance compared to horizontally rolled specimens, which had more rolling defects; joints with more complex geometries exhibited more homogeneous behavior and were less susceptible to critical defects. [182].

Chapter 2. Multi-material AM techniques and applications in PBF-LB processes

2.1 Multi-material components with immediate transitions

2.1.1 AISI 316L austenitic stainless steel with Nickel Superalloy

The objective of this study was to investigate a novel method for proving the feasibility of producing an intralayer multi-material stainless steel/nickel superalloy structure using a blade-based PBF-LB system. The created system is adaptable, affordable, and user-friendly; it may be applied to PBF-LB machines that are currently in operation. A great deal of research was done on the chemical and microstructural characteristics of the multi-material component's interface. This is the first effort where a layer-wise in-situ optical monitoring system was used to guarantee the excellent quality of the created components during the multi-material component fabrication process. Two rectangular parallelepipeds, each measuring 50x20x3 mm, were built using the M1 Cusing apparatus from Concept Laser. A specialized partitioning system (Figure 5), consisting of a support structure having the same shape as the edge of the powder chamber and integral with a vertical wall positioned to divide the chamber into two equal volumes, was developed and positioned within the powder chamber, aligned along the XZ plane (refer to Figure 6a). This innovative system facilitated the intralayer creation of a multi-material structure while preventing cross-contamination between the two metal powders. The powders employed were gas-atomized AISI 316L stainless steel and a Nickel-superalloy, both detailed in Table 1 regarding their chemical compositions. The particle size of the AISI 316L powder ranged from 15 to 53 μm, while the Nickel-superalloy powder varied from 15 to 45 μm, both exhibiting a spherical shape, as depicted in Figure 6b and Figure 6c. Table 1 further outlines the optimized set of process parameters applied in this study to produce Laser Powder Bed Fusion (PBF-LB) parts for each specified powder, ensuring a density of around 99%.

Table 1. Chemical compositions and process parameter values.

Chemical composition of powder materials [wt.%]										
	C	Ni	Cr	Mn	Co	Mo	Al	Ti	W	Fe
Nickel-superalloy	0.16	Bal.	15.60	-	10.73	1.20	2.98	5.17	2.11	-
AISI 316L	0.02	10.10	16.70	1.00	-	2.04	-	-	-	Bal.

Process parameters						
Laser power [W]	Scan speed [mm/s]	Laser spot diameter [µm]	Hatch distance [µm]	Layer thickness [µm]	Scan strategy	Island size [mm^2]
100	200	200	140	30	random island	5x5

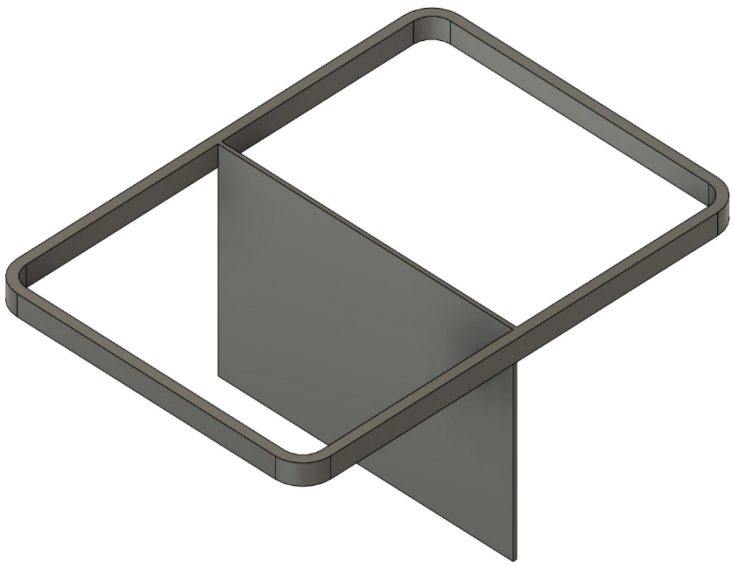

Figure 5 - Drawing of the equipment designed to divide the powder chamber into two adjacent and equal compartments

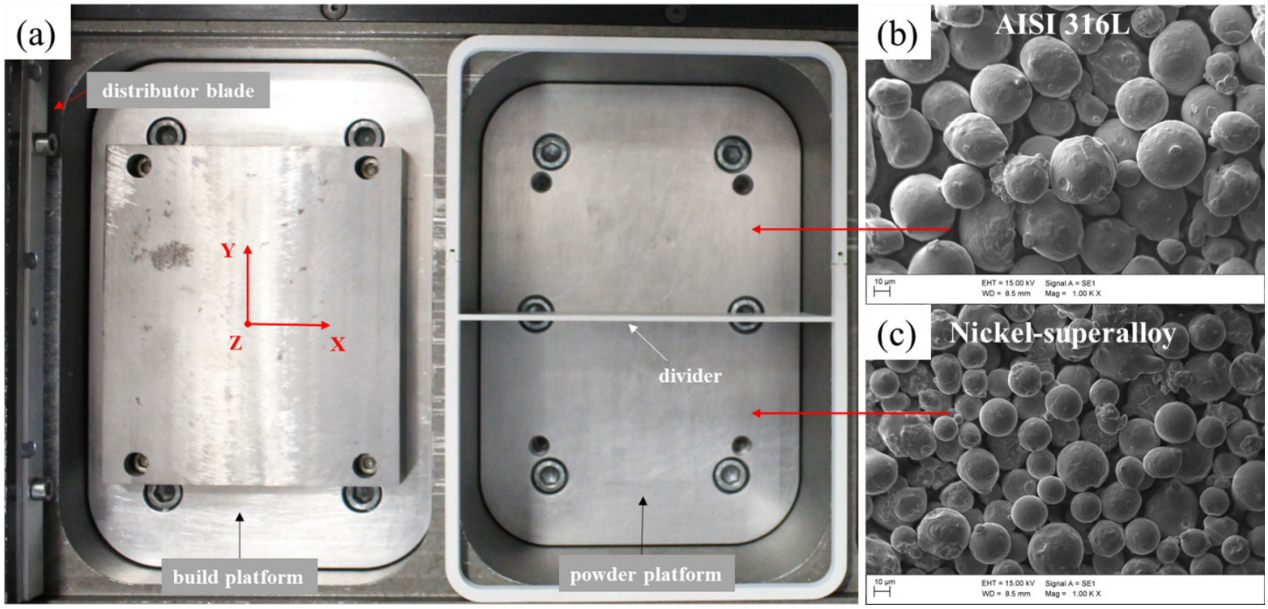

Figure 6 - (a) Design of the partitioning system within the powder chamber that enabled the intralayer fabrication of the multi-material structure; (b) and (c) SEM images of AISI 316L and Nickel-superalloy powders.

2.1.1.1 In-situ optical monitoring system

An image processing methodology detailed in Figure 6 and a layerwise optical monitoring device known as High Resolution-Optical Tomography (HR-OT) were used to characterize in-situ and real-time the process during the production of the multi-material structure. Specifically, the monitoring system implemented consists of a high-resolution CMOS off-axis camera (Canon Eos 1100D), equipped with a lens and a set of neutral density filters. The camera was set in bulb mode with an ISO equal to 100; furthermore, the exposure time was synchronized with the scanning time of each whole layer through a trigger. Previous publications [183,184] provide detailed descriptions of the adopted monitoring approach and statistical process control. This monitoring system made it possible to save a number of images equal to the number of layers required for the complete construction of the specimens. An example is shown in Figure 7.

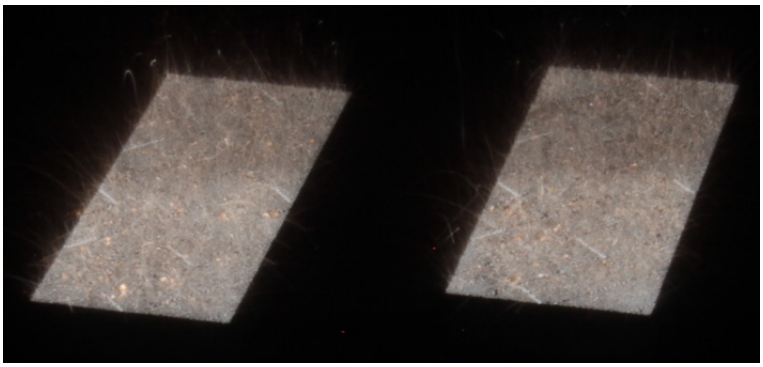

Figure 7 - Image captured by the monitoring system during laser scanning for the creation of one of the layers.

From these images, the central part where the interface between the two materials that made up the sample was cut out (see Figure 8a and Figure 8b).

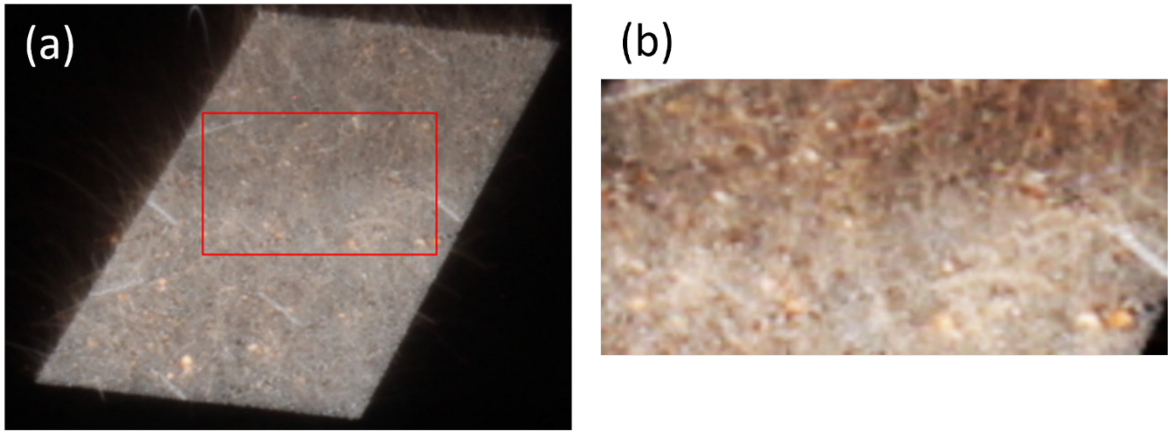

Figure 8 - Definition of the area of the images subjected to statistical analysis.

The window was transformed into a binary image (Figure 9) using the image analysis techniques, from which the real form (a curve) of the interface between the two materials is obtained.

Figure 9 - Result of the binary conversion of the cropped portion of the images

After these steps, it is possible to obtain a graph (Figure 10) showing on the x-axis the number of pixels corresponding to the width of the images and, on the y-axis, the grey value for each abscissa (a value that can range from a minimum of 0 to a maximum of 255 and depends on the number of white pixels).

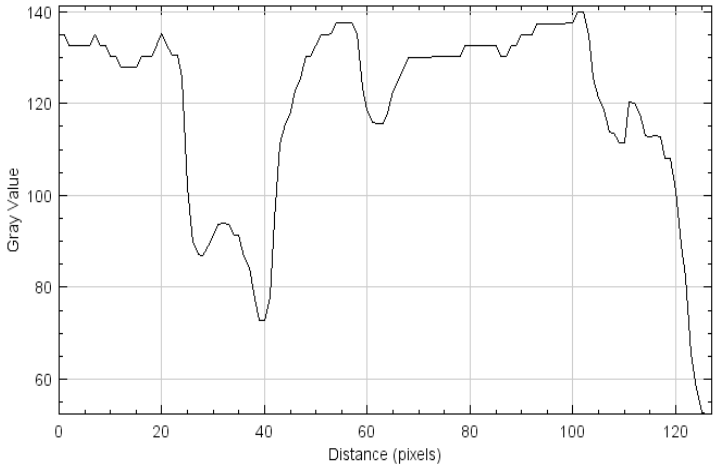

Figure 10 - Grey value graph

The outcome of the monitoring analysis is the deviation (D) of the actual interface profile between the two materials from the ideal (linear) one, which is shown in Eq. 1.

$$D = \frac{1}{L}\sum_{i=1}^{L}|GV_i - \overline{GV}| \quad (1)$$

Where:

- L = width clipping window (px)
- GV_i = gray value after threshold segmentation
- $\overline{GV}$ = arithmetic mean of the GV_i values
- i = i_{th} pixel in the clipping window.

2.1.1.2 Characterization of multi-material structure

A thorough metallographic analysis of the samples was done in order to look into the manufacturability of the created multi-material structure. After the samples were appropriately prepared and a chemical etching appropriate for both materials (10ml HNO3¬¬3 + 50ml HCl + 60ml glycerol), the microstructural examination was first carried out using an inverted optical microscope. The contact region was then specifically examined using Energy Dispersive X-ray Chemical Microanalysis (EDX), which was carried out using a scanning electron microscope.

Lastly, a hardness tester was used to assess the Vickers microhardness profile in accordance with ISO 6507-1 test standard (0.3 kgf applied stress and 10 s dwell duration).

2.1.1.3 Results and Discussion

The nickel-superalloy region had γ' microstructure in a dendritic pattern, as demonstrated by metallographic study and shown in Figure 11a and Figure 11d [185,186]. Nevertheless, the same region was affected by a non-negligible number of microscopic cracks that were visible by laser tracks. The AISI 316L section (Figure 11a and Figure 11b) had a flawless structure free of porosity and with a dendritic shape. There were no cracks or porosities in the contact region between the two metals (Figure 11a). Swirls resulting from the Marangoni effect between the two distinct materials may be seen in Figure 11c.

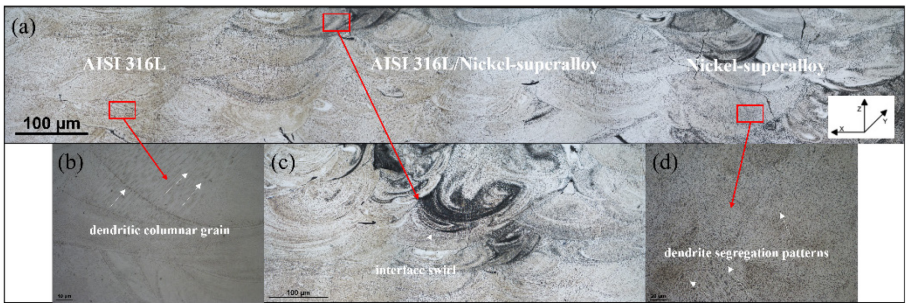

Figure 11 - Microstructure of the two mayerals used to manufacture the specimens

As previously mentioned, the Marangoni convection-induced circular flows changed the size of the molten pool, which in turn impacted the migration of the elements from the two alloys and sorted them into extremely strong bonds. [187,105]. This excellent outcome was further corroborated by SEM examination (Figure 12a), which displays a steady and progressive variation in the concentration of certain distinctive elements (Fe, Ni, and Ti) of the two alloys near the interface. Furthermore, the chemical analysis revealed the restricted width (≈600 microns) of the two materials' interface area; EDX maps corroborated this finding (Figure 12a). Figure 12b illustrates how the microhardness of the AISI316L (≈230HV) and Nickel-superalloy (≈390HV) increases consistently within the interface zone (≈600 µm). According to Wang et al., this outcome is additional evidence of the two materials' strong metallurgical connection [26]. Notably, investigations based on microhardness, metallography, and chemistry did not reveal the existence of brittle intermetallic phases.

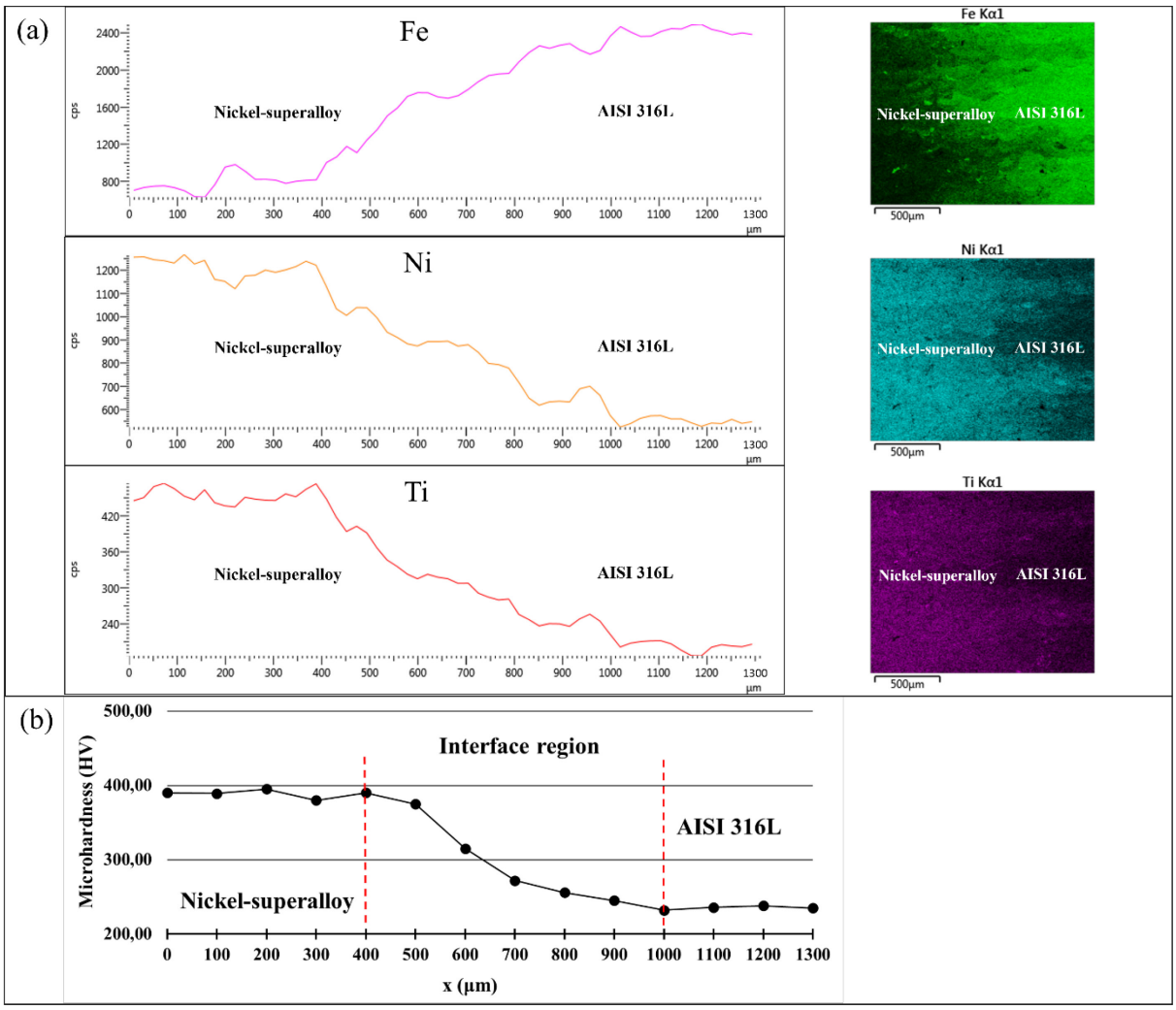

Figure 12 - Results of chemical analysis and Vickers hardness measurements performed on test specimens

Lastly, because parameter D (specified in Eq. 1) stays under control for the duration of the print, statistical control of the process - developed through the control chart depicted in Figure 13 - demonstrates in real-time, layer by layer, the lack of contamination between the two distinct materials.

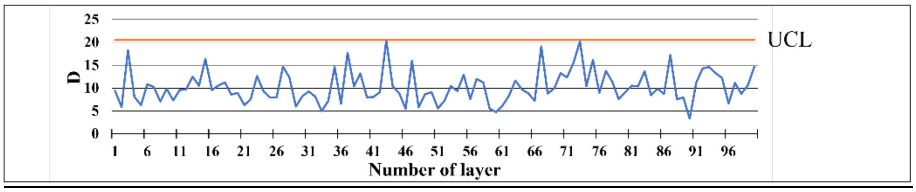

Figure 13 - Control chart for parameter D as determined by Eq. 1

2.1.1.4 Conclusions

This study examined a novel method for assessing the manufacturing viability of an intralayer multi-material stainless steel/nickel superalloy structure that is created using a blade-based PBF-LB technique. Here is a list of the principal outcomes.

A very small interface (about 600 μm) was seen at the interface, which showed excellent bonding between the two materials and no signs of cracking or porosity.

The presence of swirls caused by Marangoni convection in the interface area indicated a strong metallurgical bond between the two materials; this conclusion was supported by the steady and gradual variation in the microhardness and concentration of the two alloys' characteristic elements (Fe, Ni, and Ti).

The layer-wise in-situ optical monitoring system's deployment made it possible to monitor, in real time, the layer-by-layer variation in the real interface profile between the two materials and the ideal (linear) one throughout the entire structure. This system allowed for the assurance of the high quality of the produced component by preventing contamination between the materials without the need for additional, costly, and time-consuming inspections.

The current work shows that intralayer multi-material structures can be successfully fabricated using the established technology. The outcomes show this novel methodology's enormous potential, which may be further developed in the future to fabricate functionally graded intralayer structures.

2.1.2 AISI 316L with 18Ni (300) Maraging steel via PBF-LB process

The production of a bi-metallic component combining AISI 316L stainless steel and 18Ni (300) Maraging steel can be highly beneficial for applications requiring a combination of corrosion resistance and high strength. AISI 316L is a low-carbon version of 316 stainless steel, renowned for its exceptional resistance to corrosion, particularly in harsh environments such as marine or chemical processing industries. Its excellent formability and weldability make it a preferred choice for components exposed to corrosive conditions. On the other hand, 18Ni (300) Maraging steel is known for its superior mechanical properties, including high tensile strength, toughness, and resistance to fatigue, thanks to its nickel-rich alloying system and age-hardening treatment. This steel is commonly used in aerospace, tooling, and other high-performance applications where strength is paramount. Combining these two materials into a bi-metallic component leverages the distinct advantages of each: the corrosion resistance of AISI 316L in external environments and the superior strength and hardness of 18Ni (300) Maraging in critical load-bearing sections. Additionally, such a bi-metallic structure can be tailored to optimize performance in specific regions of the component, enhancing its overall functionality without compromising on either strength or durability.

The aim of this work is to successfully generate intralayer bi-material samples consisting of AISI 316L and 18Ni (300) Maraging using the above technology for the first time. Based on data from metallurgical and mechanical testing, the results show that this unique technique is reproducible and capable of creating durable intralayer interfaces. Although multi-material printing methods often produce weak interfaces between materials that have notably different mechanical properties, this methodology reduces the discontinuities that are characteristic of multi-material additively manufactured components while also enabling the production of bi-materials with stronger interfaces. Because these benefits may be achieved without changing the machine and without requiring expensive extra equipment, they can be implemented rapidly and economically.

2.1.2.1 Materials and Heat Treatment

The PBF-LB process uses AISI 316L stainless steel (Mimete Metal Powders) and 18Ni (300) Maraging steel (GE Additive) as raw materials. Based on Figure 14, both powders had good spherodity and were generated by gas atomization.

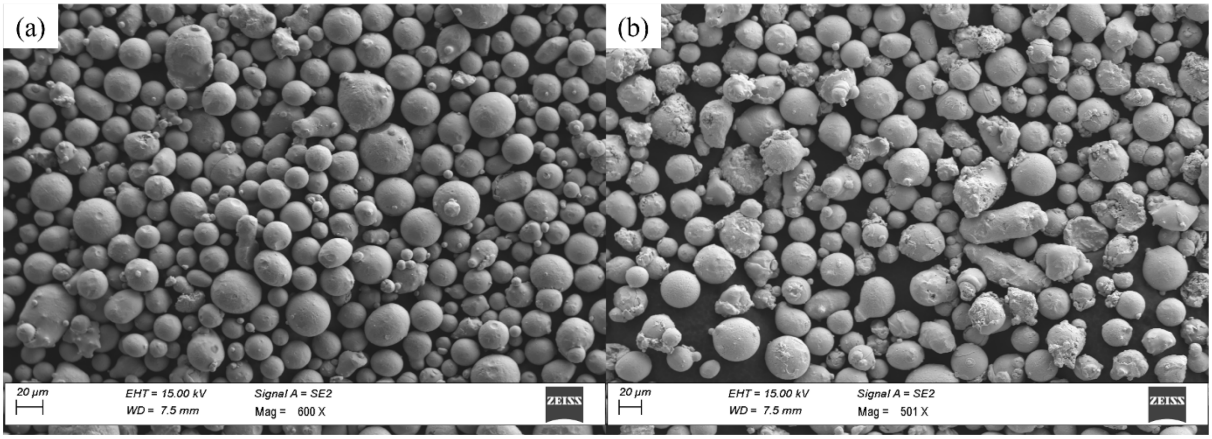

Figure 14 - Metal powders used for multi-material fabrication: (a) 18Ni (300) Maraging steel and (b) AISI 316L stainless steel

Table 1 displays the two materials' chemical compositions as confirmed by the manufacturers. The two materials' chemical compositions may be clearly distinguished from one another, as evidenced by the differences in the percentages of the elements Ni and Mo as well as the presence of Ti and Co in the 18Ni (300) Maraging particles and the Cr, Mn, and Si contents in the AISI 316L powders. All of the materials are low-carbon alloys, nevertheless.

Table 2 - Chemical composition of the powders conducted by inductively plasma optical emission spectrometry.

Metal Powder	**Powder Size (µm)**	**Chemical Element** (all values are in weight %)								
		C	**Cr**	**Fe**	**Mn**	**Mo**	**Ni**	**Si**	**Co**	**Ti**
18Ni (300) maraging steel	15–53	0.02	-	bal	-	4.70	18.7	-	10.4	1.15
AISI 316L stainless steel	15–45	0.01	17.30	bal	1.16	2.31	12.6	0.69	-	-

Furthermore, these materials possess distinct mechanical and physical attributes, including resistance to wear (18Ni (300) Maraging), resistance to chemical corrosion, and non-magnetic nature (AISI 316L) [188,189,151]. In contrast to AISI 316L stainless steel, 18Ni (300) Maraging steel has a higher strength and less ductility. As a result, their combination may offer a means of producing robust yet durable materials, preventing catastrophic failure. 18Ni (300) Maraging steel is typically obtained after solution annealing treatment followed by ageing hardening. Furthermore, the two materials' thermal characteristics (thermal capacity and coefficient of thermal expansion) differ significantly, which complicates the production of their multi-material combination [147]. In order to improve the mechanical properties, specimens made of 18Ni (300) Maraging steel were given the suitable furnace ageing treatment after

manufacture. The specifics of this treatment are covered in depth in earlier research by the same authors [151].

2.1.2.2 Experimental set-up of the PBF-LB process for multi-material manufacturing

The powder platform was split into two neighbouring volumes in order to fabricate bi-material components inside the layers (see Figure 15). Ad hoc equipment (a planar divider) was made specifically for this use and was intended to be installed inside the powder platform. The divider was constructed as a single piece, and to guarantee centering, its rectangular edge matches the size of the powder platform [42]. After filling with powders, the apparatus that was utilised to accomplish the separation required to be taken apart. With the help of this technique, the platform may be filled without the powders mixing together unintentionally or changing shape. In this experiment, the divider was positioned so that it separated the powder chamber into two equal sections.

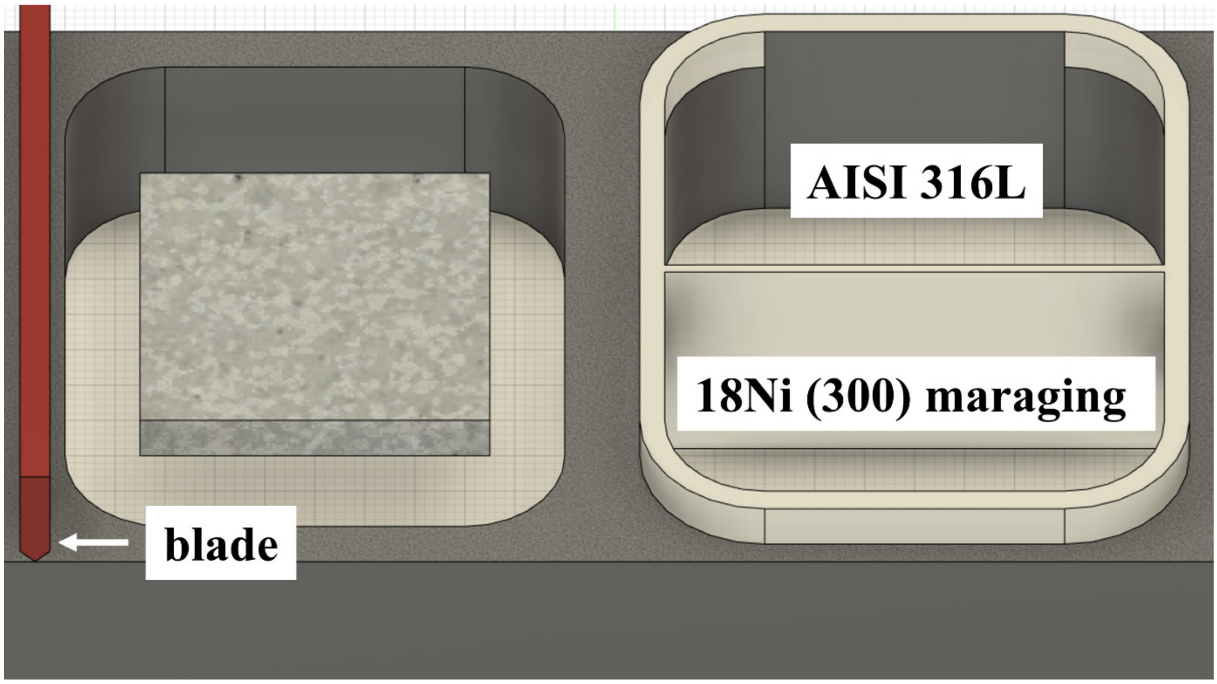

Figure 15 - Schematic diagram of the custom-designed equipment for intralayer multi-material fabrication using the conventional blade-based PBF-LB system

The M1 Cusing Concept Laser machine was configured for manufacturing based on process parameters optimised in earlier trials conducted on the same materials [190,191,192]. This allowed for the production of samples with a relative density > 99%, as determined by the Archimedes method in compliance with ASTM B962-17. As a result, even though these are two distinct materials, it was decided that the entire surface that the laser scanned should be scanned

using the same set of parameters (as in [190,192]). To be more precise, the following process parameters were employed to fabricate all samples: hatch distance of 140 μm, laser spot diameter of 200 μm (set by the machine), minimum adjustable layer thickness of 30 μm, maximum adjustable laser power of 100 W, and scan speed of 200 mm/s.

2.1.2.3 Specimens' fabrication

To explore the bi-material additive manufacturing method, numerous types of specimens were manufactured for performing metallographic, chemical, and mechanical tests. In the first stage, powders of each material were utilised individually to produce five tensile specimens to serve as the basis for comparison against the bi-material specimens. Specifically, dogbone-shaped examples were designed based on the ASTM E8-21 standard for powder metallurgy, as shown in Figure 16. Two batches of five bi-material tensile specimens with the same geometry were then created by employing the in-house divider (described above). To possible evaluate the effective mechanical properties of the interface between the two materials, the bi-material separation was realized at the mid-length of the specimens (Figure 16).

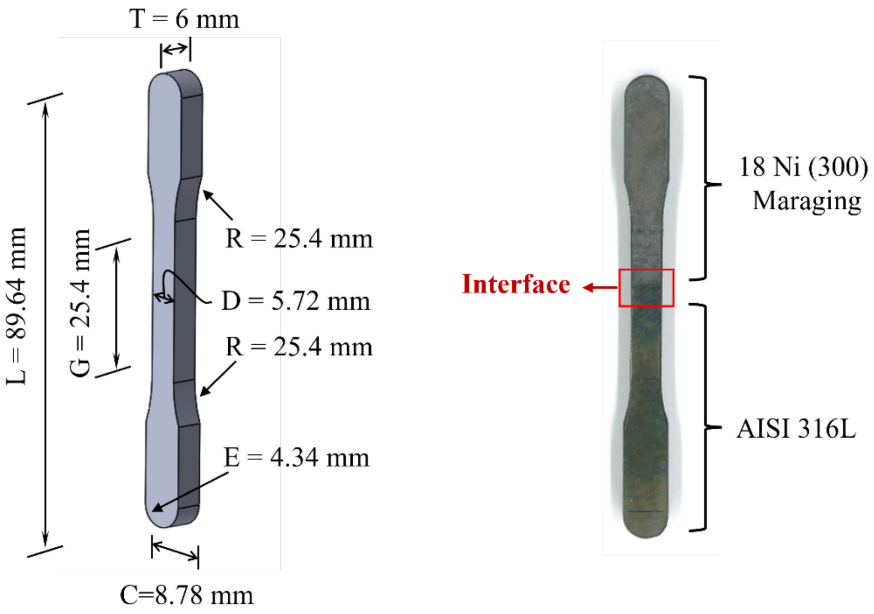

Figure 16 - Drawing of the geometry of the manufactured specimens and indication of the position of the two materials.

Moreover, a test specimen for metallographic investigations with a parallelepiped shape of 10x10x20 mm was manufactured for each batch (Figure 17).

Figure 17 - Image of specimens made for tensile tests and metallographic examinations.

The different tensile specimens were identified with abbreviations, as shown in Table 2.

Table 3 - Specimens identification

Specimen ID	Tensile Specimens Description
M1 T1÷T5	AISI 316L
M2 T1÷T5	18Ni (300) Maraging
B1 T1÷T5	Bi-Material (Batch 1)
B2 T1÷T5	Bi-Material (Batch 2)

2.1.2.4 Metallography and mechanical testing of the printed specimens

In order to examine and validate the intralayer AM showed in this work and investigate the final quality of the manufactured products generated using this new technological solution, an in-depth metallurgical and mechanical evaluation was carried out.

Specifically, a preliminary metallographic study was carried out to examine the quality of the interface and analyze the manufacturing density of the different components. This investigation was performed with the Nikon Eclipse MA200 inverted optical microscope after the samples had been adequately prepared by cutting, mounting, and polishing techniques.

In order to evaluate any contamination between the two materials during fabrication and the presence of intermetallic phases, the manufactured samples were further characterized in terms of microstructure, chemical composition, and phase analysis. The characterisation was principally carried out by employing scanning electron microscopy (SEM, Quanta 650 FEG-SEM, ThermoFisher Scientific Inc.) equipped with electron backscattered diffraction (EBSD, NORDIF) and energy dispersive X-ray spectroscopy (EDS, EDAX) equipment.

To examine the change of mechanical characteristics at the interface, Vickers microhardness tests were carried out using an HMV-G by Shimadzu tester, utilising the ISO 6507-1 standard test method, for microhardness of materials under a force of 0.3 kgf for 10s dwell time.

2.1.2.5 Chemical and Microstructural characterization of interfaces and low-force Vickers hardness results

Figure 18a and Figure 18b show the optical micrograph of the test specimen in both the transversal and the longitudinal cross-sections. Several portions can be distinctly defined. The melt pools and the scanning patterns can also be clearly observed across the micrographs. We note that the austenitic phase has a striking bright contrast, whereas the martensitic phase displays a contrasting dark look. These opposing properties are related to the unique etching regimen adopted, which effectively uncovers the phase boundaries. No defects, such as cracks, porosity, or lack of fusion, are observed in the contact area (see Figure 18a and Figure 18b).

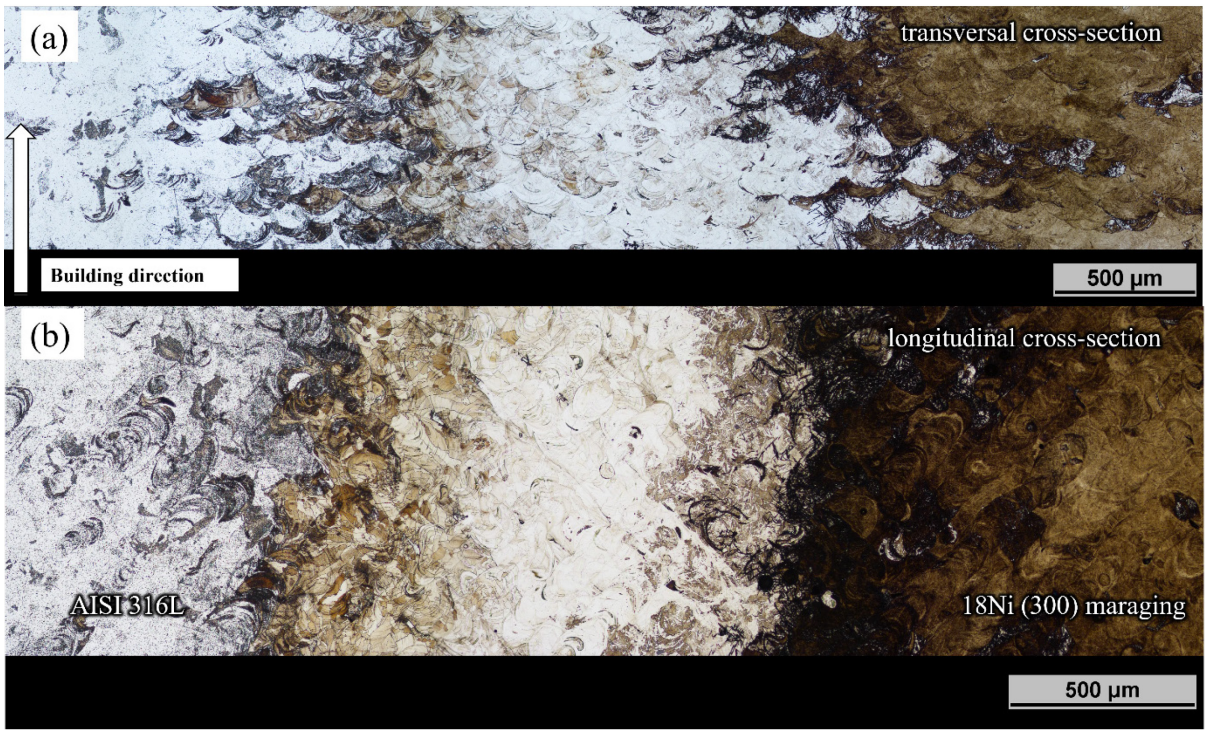

Figure 18 - Optical micrograph of the test specimen (Batch 2) interface for metallographic analyses at 100 magnification: (a) cross-section showing the building direction; (b) longitudinal section showing the single layer.

The phase information can also be detected by the matching hardness values, where austenite exhibits a hardness lower than 300 HV whereas martensite can be as hard as 600 HV (see

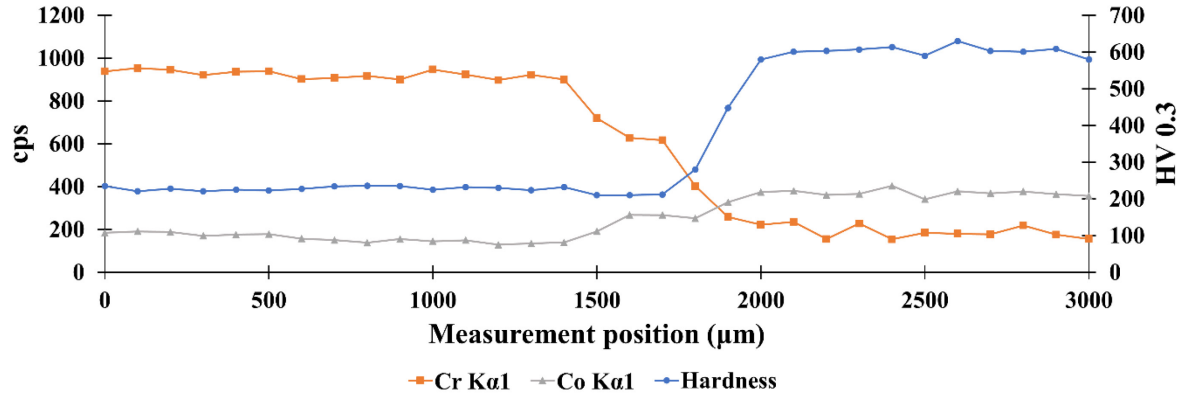

Figure 19). The transitional area is not a clear interface between the two phases, but a narrow mixing region (≈500 µm) with the two phases intersecting each other (bright contrast and dark contrast). Further validation of the aforesaid finding was acquired using EDS analysis, by observing the trend of the main characteristic chemical elements, present in the two alloys, Cr and Co, in the same area where the Vickers hardness test was done. The observed concentrations shift from a maximum to a minimum value within a range overlaid on the transitional zone of the hardness values (see

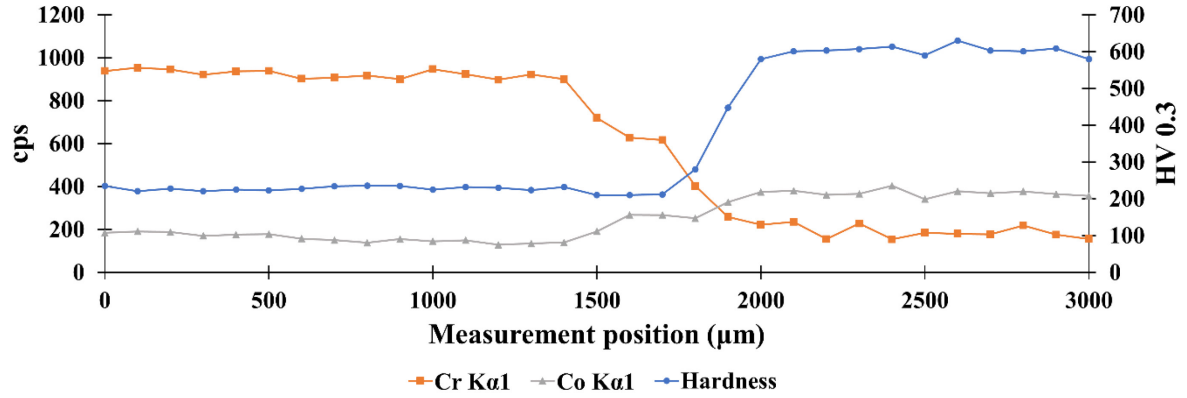

Figure 19).

The trend of the measured quantities is gradual for each of them and in line with the expected results, demonstrating the good quality of the metallurgical bond between the two materials [26].

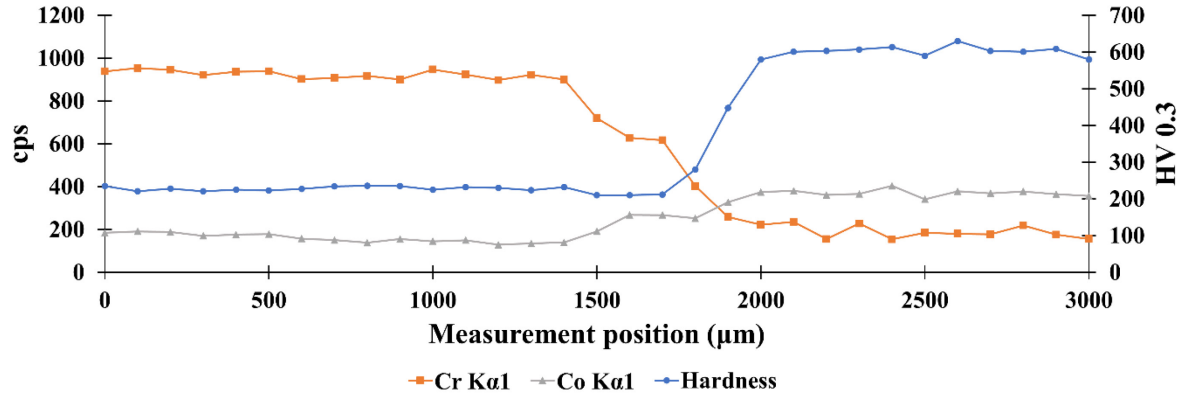

Figure 19 - EDS and Hardness test results profile across the interface.

Mechanical tensile tests were also carried out and it was observed that the failure of the specimens occurred in a different area than the interface between the materials. This result also confirms the good quality of the joint in terms of mechanical performance.

2.1.2.6 Conclusions

In this work, a traditional blade-based PBF-LB system was utilized to facilitate the multi-material intralayer fabrication of two steel powders, AISI 316L and 18Ni (300) Maraging. The following is a summary of the key findings.

• Excellent bonding between the two materials is demonstrated by metallurgical examinations of the interface using the established technique; the interface is relatively small (about 500 µm) and free of cracks and porosity in the transition zone.

• The interface's EDS and hardness test findings attest to the high caliber of the metallurgical link between the two materials; the lack of brittle intermetallic compounds is confirmed by the gradual and regular trends in the transition zone.

• Tensile tests, which show that the fracture of the bi-material specimens occurs on the weak region (AISI 316L), confirm that the interface strength is higher than the AISI 316L.

Therefore, the current work shows that modifying conventional blade-based systems to produce multi-materials at the layer level can be achieved at a reasonable cost using a flexible, adaptive method. One of the main issues with AM multi-material fabrication is resolved by this solution, which can also be used to join materials with relatively dissimilar mechanical properties. This opens the door for future structural applications that call for mutually exclusive qualities (like strength and toughness).

2.1.3 Bi-Material lattice structures by PBF-LB process

Cellular structures classified as lattices include sheet-based structures with periodic repeats of unit cells, strut-based topologies with triply periodic minimum surface, and other forms [193,194]. According to Ashby [195], the compressive response of strut-based structures can be divided into two categories based on their connectivity: 1) Bending dominated structures with low connectivity, where struts deform via bending and usually have a flat stress-strain plateau, and 2) Stretching dominated lattices with high connectivity, where struts deform via tension or compression and have a high structural efficiency, though they usually experience post-yield softening, which is not ideal for energy absorption applications. But lattice features are not so easily generalized; Gibson & Ashby [196] go into additional detail about the dependency on material and relative density. Body-centered cubic (BCC) lattices of different metals show distinct failure mechanisms and consequent stress-strain responses, even within materials widely employed in metal AM. While BCC lattices of Ti6Al4V [197,198,199,200,201] and Al10SiMg [202,203,204,205,206] fail with shear bands and crushing behavior, resulting in an unstable stress-strain response that is not ideal for energy-absorption applications, 316L stainless steel lattices [207,208,209,210] exhibit smooth ductile behavior with a flat or hardening stress-strain plateau typical of bending dominated structures. The octet-truss (OCT) made of 316L [210,211,80] exhibits the expected post-yield softening for low relative densities, but as relative density increases in the range of 0.2–0.3, the mode of deformation changes from the “twist” mode via buckling to a more stable mode of bending at the nodes [80]. This is similar to what happens when a typical stretch-dominated lattice for similar materials is examined. This leads to a stable stress-strain plateau that is appropriate for energy absorption; nevertheless, the expected unstable collapse is observed with local fracture and shear banding for less ductile materials as Al10SiMg [212,213]. Although 316L is a great material for energy absorption applications, applications like motorsport and aircraft require energy-absorbing crash structures. These applications are better suited for lightweight, often more brittle AM materials like titanium and aluminum alloys.

The purpose of this work is to examine the bi-metallic lattice structures of 316L and 17-4PH stainless steel that are produced by an intralayer multi-material fabrication technique. Although there is a good chance that post-build heat treatment would change the materials' mechanical characteristics, they were selected for their PBF compatibility. 316L is an austenitic stainless steel with high ductility and formability that is used in many industrial fields, such as the food and petrochemical industries, and is precipitation-hardening martensitic stainless steel with high strength and high hardness [214]. Therefore, their combination could offer a method of

obtaining materials that are both tough and strong, removing the possibility of catastrophic failure and many other applications. In order to examine the interactions between the two sections of a bi-material lattice that is printed concurrently, this combination of materials and heat treatment choice creates a difference in strength and elongation at failure between the two materials. The analysis of the material interface resulting from this manufacturing technique is made possible by the differing microstructure of these materials.

This study is the first to successfully build bi-material lattice structures using the intralayer multi-material technique for functional components. Experimental and numerical research is done on the compressive behavior of the resultant material and interface (both as-printed and after heat treatment) in bulk and complex lattice structures. The possible applications of the 316L/17-4PH structures to absorb energy and modify lattice properties are investigated, and the behavior of the bi-metallic lattices is predicted using finite element analysis.

2.1.3.1 Design & Modelling of Test Samples

Two unique unit cells—the octet truss (OCT) and body centred cubic (BCC)—are used to design lattice samples. The samples are 15 mm cubes with a 0.7 mm strut diameter; Figure 20 and describes the sample design in full with photos. The volume of solid material divided by the volume of the bounding box is the formula used in CAD software to get the similar volume fraction of the samples. Three material states are used in the manufacturing and testing of each lattice geometry: 1) 17–4PH 100%; 2) Bi-material: 17–4PH 50%; 3) 316L 100%. For testing purposes, the bi-material design is orientated so that the two material parts are either loaded in parallel or in series.

Table 4 - Design details of lattice samples. All dimensions are as-designed values, and the volume fraction calculated based on the CAD file.

Unit Cell	**Unit Cell Size** (mm)	**Overall Dimension** (mm)	**Strut Diameter** (mm)	**Volume Fraction**
BCC	3	15×15×15	0.7	0.210
OCT	5	15×15×15	0.7	0.217

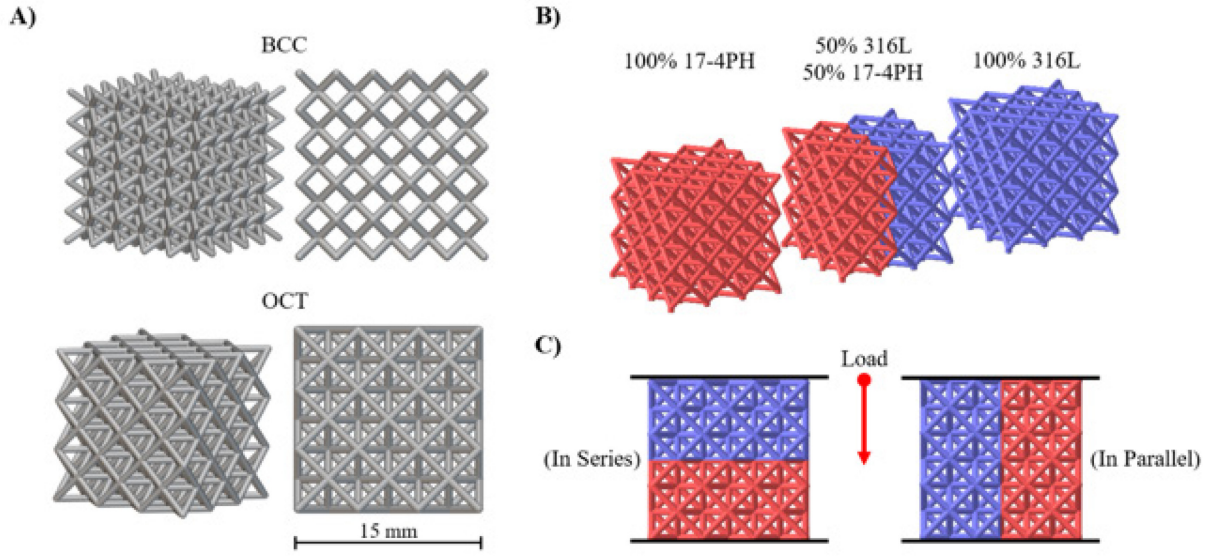

Figure 20 - A) BCC and OCT lattice designs. B) Three material states demonstrated with the OCT cell, including the bi-material which is split along its centre line. C) Test orientations for bi-material samples.

2.1.3.2 Manufacturing of multi-material lattice samples & heat treatment

Using a partitioning system in the powder feed, Concept Laser's traditional M1 machine was customized internally to manufacture intralayer multi-material samples for usage in all lattice configurations [60]. The same authors have previously published a detailed description of the experimental equipment utilized for intralayer multi-material synthesis [60], and Figure 21A) provides a representation of the printer configuration. The bi-material pieces are centered on the build plate along the interface of the two materials in Figure 21B), which illustrates an example of the manufactured samples.

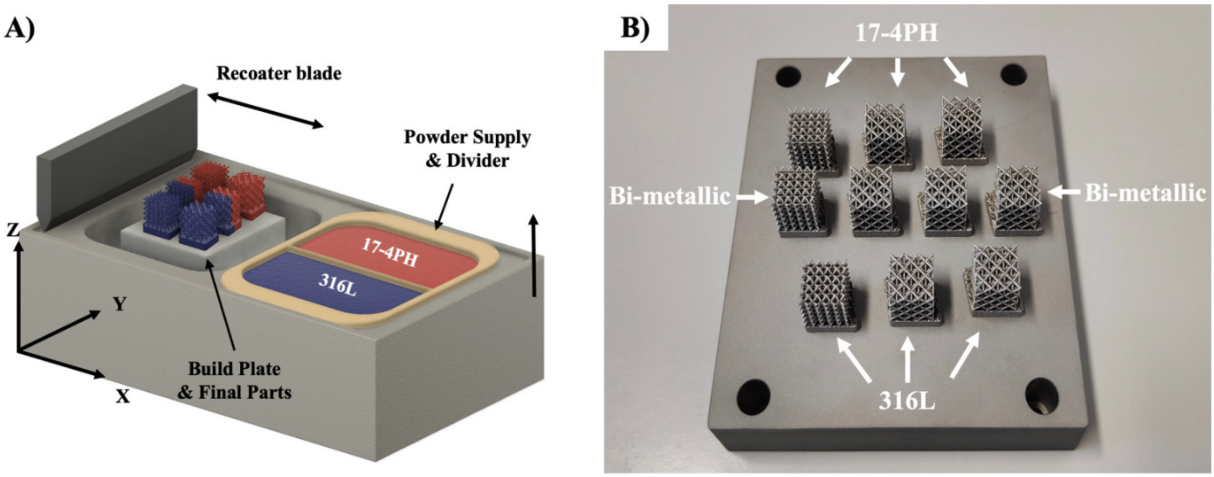

Figure 21 - – A) CAD diagram of the equipment used for the sample fabrication. B) Single & multi-material lattice structures after powder removal.

Aside from minor adjustments, the production machine (M1 Cusing, Concept Laser) was set up with process parameters gleaned from earlier experiments on the same materials [97,5]. This was done with consideration for the fact that certain geometries, like lattices with thin overhangs, require specific parameters in order to prevent distortion, subpar down-skin surface quality, and job failures. All samples, regardless of material, were subjected to the same set of procedure parameters, which are listed in Table 5. Furthermore, all samples were created utilizing the proprietary Concept Laser technique known as random island scanning strategy, which makes use of a square island structure with a side length of 5 mm. After that, each successive layer is oriented differently in the XY plane, with a 1 mm offset in each direction. As prior research has shown [192,110], these tactics were put into practice with the goal of reducing the heat stresses experienced throughout the PBF-LB process.

Table 5 - PBF-LB process parameters used for sample production.

Process Parameters	Value
Laser Power (W)	80
Exposure Speed (mm s^{-1})	175
Laser Focus Diameter (µm)	200
Hatch Spacing (µm)	140
Slice Thickness (µm)	40

For the whole printing process, the samples were created in a nitrogen-protected atmosphere to guarantee that the residual oxygen content stayed below 1%. The two materials in powder form are produced via gas atomization (in an argon atmosphere), and Table 6 provides information on the chemical makeup of the two materials as disclosed by their producers.

Table 6 - – Chemical composition of the individual elements characterising the two materials, as determined by the inductively plasma optical emission spectrometry and combustion analysis technology methods.

17-4PH [wt.%]					316L [wt.%]				
C	**Cr**	**Cu**	**Fe**	**Mn**	**C**	**Cr**	**Cu**	**Fe**	**Mn**
0.02	15.51	4.44	Bal.	0.59	0.016	17.80	-	Bal.	1.15
Nb+Ta	**Ni**	**P**	**Si**	**S**	**Mo**	**Ni**	**P**	**Si**	**S**
0.22	4.42	0.012	0.66	0.003	2.72	14.0	<0.02	0.34	0.007

Furthermore, samples are stress-reliveved at 650°C for the first time while still connected to the construction plate. Support structures are removed, and all samples are heat treated in accordance with the H900 standard for 17-4 PH. This involves air cooling to room temperature in between each stage of the heat treatment, which consists of a solution treatment at 1040°C for one hour and aging at 480°C for one hour.

2.1.3.3 Quality Inspection

2.1.3.3.1 Metallographic Inspection

For microscopy and density studies, a variety of bulk samples (10 mm solid cubes) and extra bi-metallic lattices are produced. In order to calculate density using Archimedes' principle, bulk specimens of each material condition are first created. Sectioning and microscopy come next. Prior to chemical etching, porosity is also determined by image analysis during the microscopic inspection. For picture analysis, FIJI [215], an open-source program, was utilized. Using methods recommended by the literature [216], bulk and lattice samples were painstakingly prepared for microscopy through cutting, embedding, polishing, and etching in order to determine their microstructural characteristics and to locate and measure any potential faulty areas. Various etching procedures are used on various samples to expose various microstructure phases. Microstructural examinations were conducted using an Eclipse MA200 inverted optical microscope (Nikon Corporation, Tokyo, Japan). Vilella's reagent (10 mL hydrochloric acid, 1-2 g picric acid, and 100 mL ethyl alcohol) was first used to etch bulk samples in order to evaluate the material interface in its as-built form (stress-relief treatment alone). The section plane employed for the examinations of the lattice structures (as-built state) is one that travels through the middle of the nodes, parallel to the specimens' build direction, and is etched using 10% oxalic acid electrolytic etching in accordance with ASTM E407. Kalling's reagent was used to generate a second batch of bulk bi-metallic samples in both the as-built and post-heat treatment states.

2.1.3.4 Results

Microscopy and CT scans are used to evaluate the lattices' dimensions and quality. Figure 22A) and B) display images of the lattices following the stress-relief and H900 heat treatment. Because of oxidation, there is a discernible color difference between the two materials at every stage. Figure 22C) displays a microscope picture of the material interface on the lattice surface, illustrating the transition between each material and the lattice struts with respect to the as-designed diameter dimension.

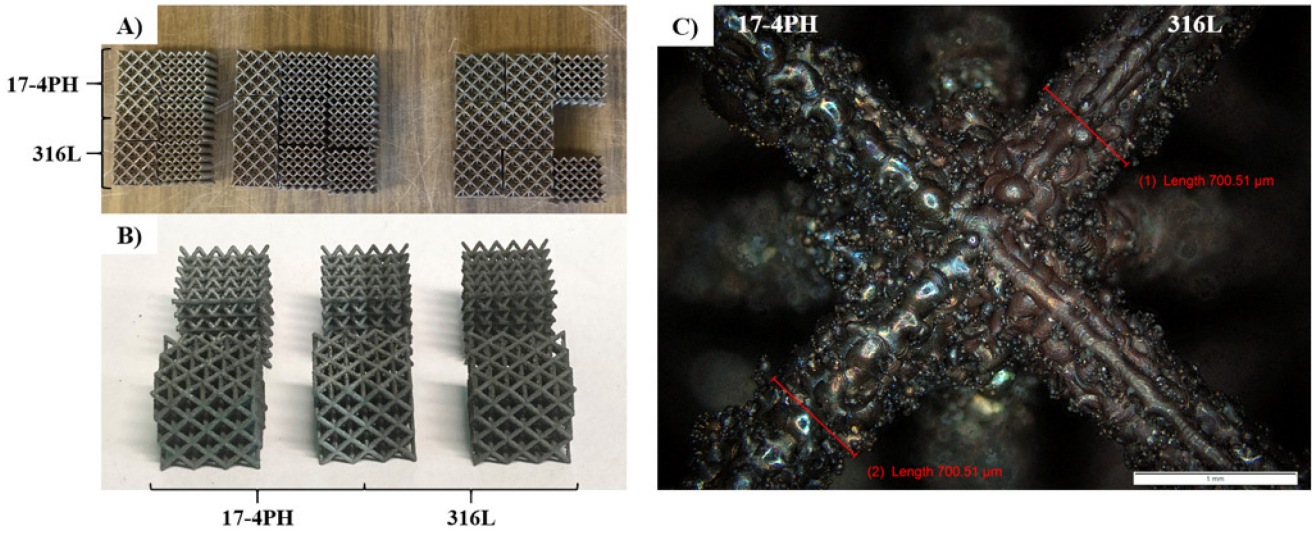

Figure 22 - - A) Image of lattice samples after stress-relief treatment only. B) Lattice samples after H900 heat treatment. C) Microscope image of the material interface at a strut intersection on the top surface of an OCT lattice (after stress-relief only). Reference dimensions of 700 microns (as-designed diameter) are included for comparison.

Using Archimedes' principle and image analysis of sectioned and polished samples, the porosity results of the bulk material samples are shown in Table 7. Although the final results differ for each approach, there is a discernible pattern showing that 17-4PH has a porosity that is around 1% higher than 316L. In the 17-4PH sample, the highest value recorded was 3.55% (per Archimedes). Figure 23 displays a sectioned bi-metallic sample. It shows the more frequent discontinuities in 17-4PH, which mostly seem to be caused by an uneven form indicating a lack of fusing. In essence, no other anomalies, such cracks, are seen in this region, and they don't seem to be clustered at the material contact. The material interface has a width of around 1 mm. Following etching, the material interface displays the square island pattern's hatchings, which were utilized as the scan route.

Table 7 - – Porosity of bulk samples determined via Archimedes' principle and image analysis of polished samples. Image analysis is performed on sectioned samples in two orientations.

Sample	**Archimedes' Principle** (% Porosity)	**Metallographic Image Analysis** (% Porosity)		
		Horizontal Section	Z-axis Section	**Average**
316L	2.67 %	1.239 %	1.051 %	1.14 %
17-4PH	3.55 %	2.193 %	2.346 %	2.27 %
Bi-metallic	3.22 %	1.711 %	2.264 %	1.99 %

Similar procedures were used to prepare bi-metallic lattice samples, but they were etched to disclose austenite; the resulting micrographs are shown in Figure 24. To display the material interface, the BCC and OCT lattices are both sectioned along the z-axis and along the lattice strut centerline. The lighter white areas are made of martensite and are 17-4PH. Austenite is present in the darker area, which is designated as 316L. One of the lattice nodes containing the interface of the two materials for the BCC and OCT specimens, respectively, is depicted in Figure 24B) and Figure 24D). The transition between one structural ingredient and another may be seen in these higher magnification photos inside a band that is about 1 mm wide. It should be noted that the BCC specimen's section plane is positioned at a 45° angle to the direction in which powder is spreading, making it unreliable for measuring the interface thickness directly. It is evident that the material interface appears to change with subsequent layers and is not perfectly aligned with the lattice nodes.

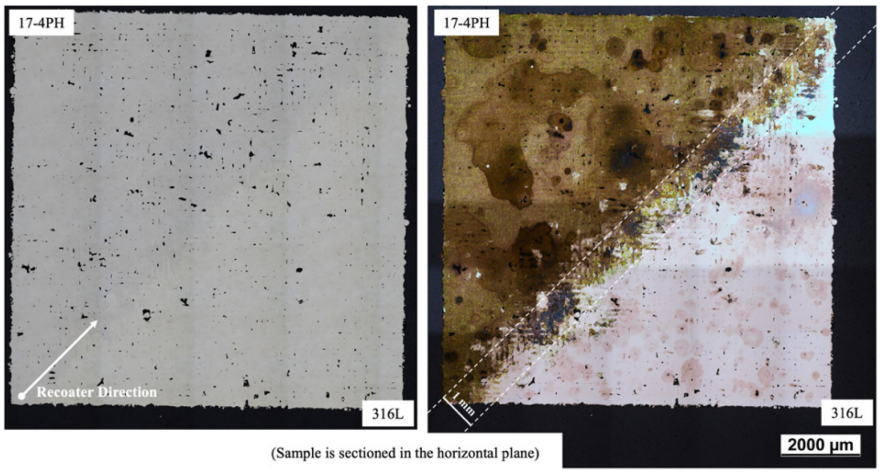

Figure 23 - - Bulk material sample before and after chemical etch with Vilella's reagent (sectioned in the horizontal plane). The samples were subject to stress-relief heat treatment only before preparation. The material interface is annotated by reference lines separated by 1mm.

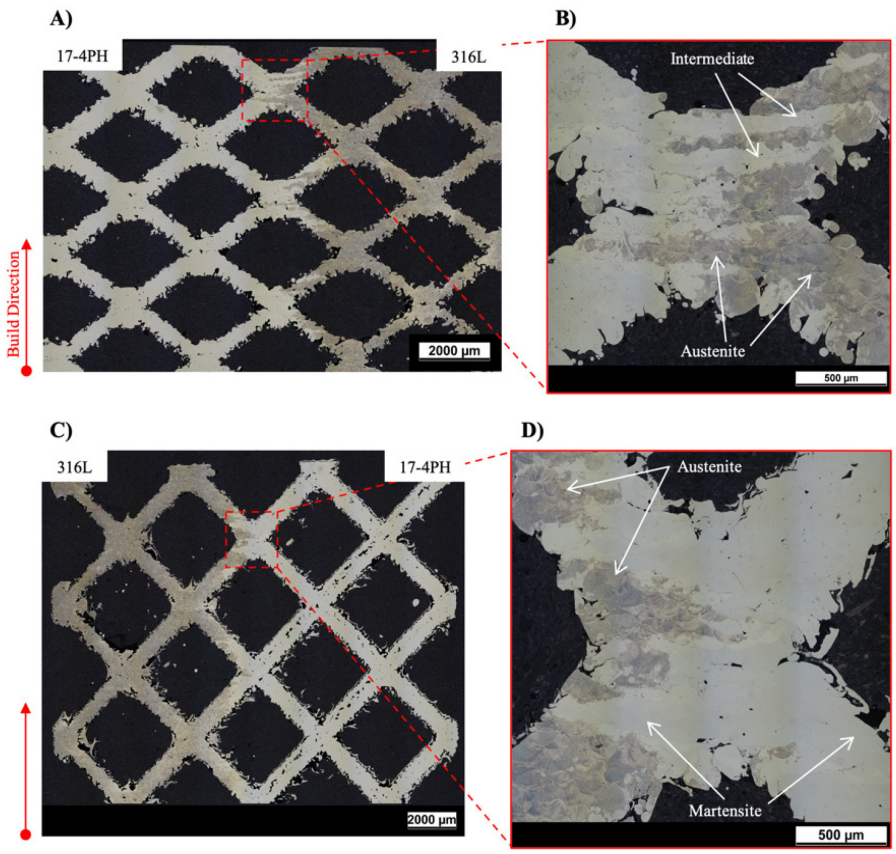

Figure 24 - - Micrographs of the specimens after electrolytic etching with focus on a strut intersection featuring the material interface. Both samples were sectioned along the z-axis and prepared after stress-relief heat treatment only. A) BCC lattice. The irregular roughness and apparent change in diameter is a result of an imperfect alignment of the sectioning plane with the centre of the struts. B) OCT lattice section. There is apparent surface roughness and debris from the sectioning process in the sample as grinding steps were reduced in sample preparation to preserve the cross section of the lattice.

Figure 25 displays bulk samples both before and after heat treatment so that the microstructure can be examined. Because the darker etched areas in Figure 24 are martensite, it should be noted that a different etchant was employed in this instance. Three distinct zones may be distinguished in the as-built state: the martensitic 17-4PH in dark grey/black, the as-built austenitic 316L in white, and an intermediate in light brown. The shape of the laser pass and the resulting melted pool structures are plainly visible. Following heat treatment, the martensitic 17-4PH grain size increases and shows apparent lighter colored areas, which are probably austenite or ferrite that has been maintained. The unique melt pool structures and laser trails are no longer visible, and the entire structure is more homogeneous.

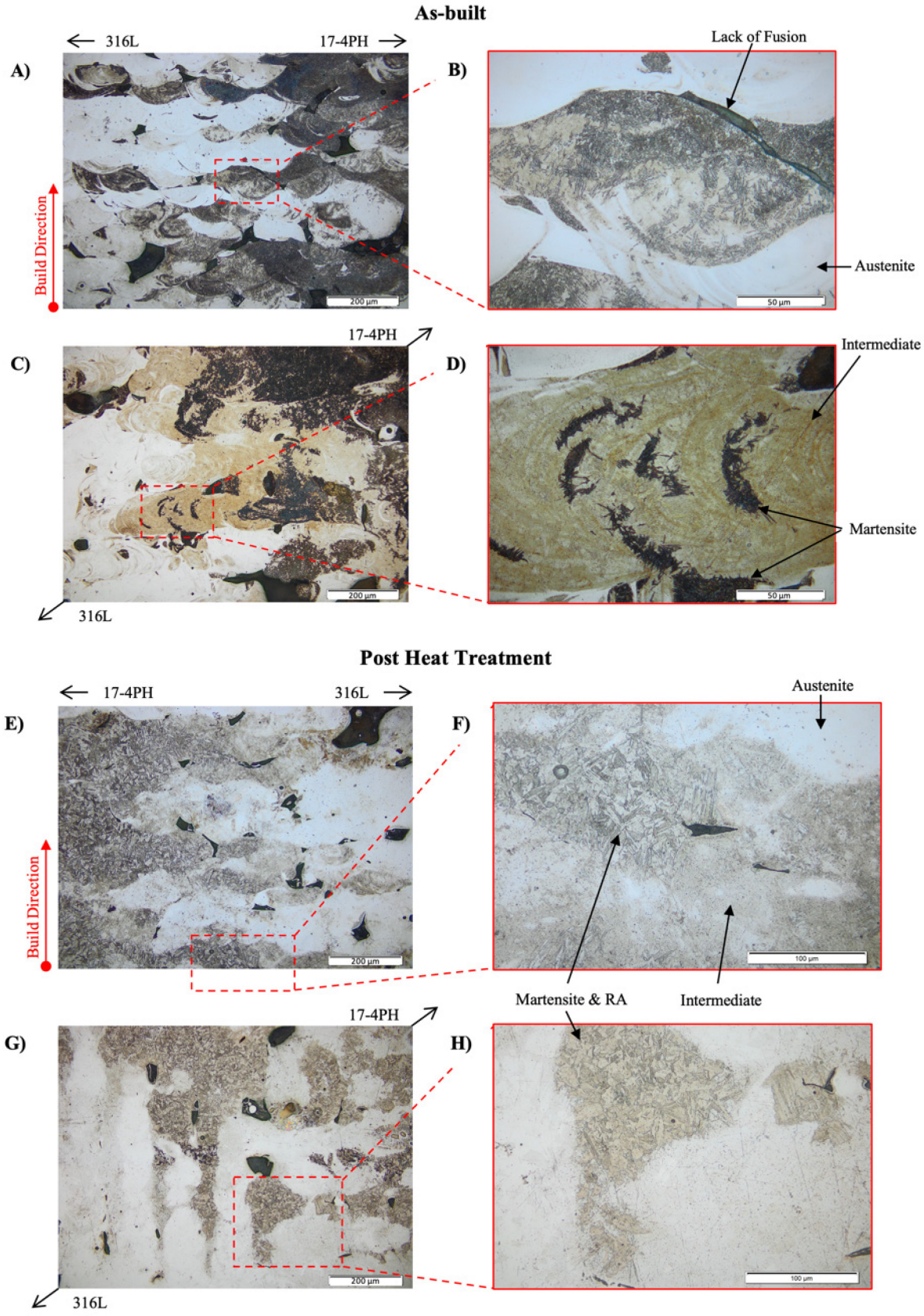

Figure 25 - – Micrographs of etched (with Kalling's) bulk specimen before (A-D) and after heat treatment (E-H). Samples A/B and E/F are cut along the z axis, while samples C/D and G/H are cut along the horizontal plane.

2.1.3.5 Discussion

Because only one set of parameters—which is better optimized for 316L—is employed, we find a difference in porosity between the two materials as well as a lack of fusion porosity on the samples. First, the measurements obtained using the metallographic and Archimedes' methods differ because, in image analysis, a threshold value must be chosen in order to differentiate missing material from the remainder of the surface under examination. This decision is based on subjective assessments, which may cause the measured value to differ from the actual value. The accuracy of the measured data might also be significantly impacted by the quality of the specimens' metallographic preparation [217]. The density attained, according to the authors, is less than the industry standard for single-material printing, but the numbers still fall within an acceptable range for the study's objectives. The lattice compression testing demonstrates that the bond is strong and that there is no specific concentration of flaws or pores around the material interface. Although more process parameter research is necessary, the various material and powder qualities make it more difficult to optimize these parameters for a variety of materials. Further complicating this process are geometries like lattices with narrow overhangs, which call for the right parameters to prevent distortion and poor down-skin surface quality.

Under the microscope, the two materials are completely fused together at the interface; no faults or cracks resulting from the mixing and solidification of the two steels are visible. Figure 25C) clearly illustrates the three separate zones that are seen along the interface: sections that are entirely austenitic and seem to consist exclusively of 316L, regions that are fine martensitic and consist only of 17-4PH, and intermediate places where both elements combine in the melt pool to form an intermediate that is most likely ferrite. Additionally, swirls are seen in the same region as a result of the Marangoni effect between the two dissimilar materials, which affects the melting pool and, in turn, the migration of the elements of the two alloys, creating an extremely strong link between them. The variable existence and width of the intermediate area across the interface implies that the degree of mixing between the two materials in the melt pool is similarly irregular. The materials used in this investigation result in complete fusion and an interface that is robust when subjected to mechanical testing. However, more control over this mixing may be desirable, and this could be accomplished by looking into different process parameters, scan strategies, and the use of a graded interface [61] with purposeful, gradual material mixing.

Even for single-material AM of this material, the heat treatment clearly reveals a larger percentage phase of non-martensite after 17-4PH, which is expected given that the material's

microstructure might change depending on feedstock and process parameters [218,219]. The interface's position is also observed to vary slightly from layer to layer as a result of the disturbance and powder spreading during the divider's removal. Because of the comparatively tiny sample dimensions, these deviations may be significant for minute structures like lattices and have an appreciable impact on the compression results. However, as it enables intralayer multi-material AM research and manufacturing on a typical PBF machine, the ease of use and low cost of this multi-material approach should also be acknowledged.

2.1.3.6 Conclusions

This work studied metal lattice structures using a unique multi-material powder bed fusion technique. To create the finished lattices, which are examined and tested, each component is processed concurrently as part of a single manufacturing phase. From this, we can draw the following conclusions:

• Strong and complete fusion is observed in the material interface and is demonstrated to be robust under compressive loading both in-series and in-parallel.

• Bi-metallic lattice structures of 17-4PH and 316L stainless steel are successfully manufactured using an intralayer multi-material powder bed fusion system.

• In multi-material lattices, the typical failure modes of lattice cell types and their parent materials carry over and remain unaltered.

2.1.4 Interfacial analysis by optical monitoring of layer level multi-material parts fabricated via Laser-Powder Bed Fusion

This experiment examined a high-resolution optical monitoring system's ability to give interface data between two distinct metallic powders that were utilized in tandem with one another during the PBF-LB process. The results obtained from optical monitoring were confirmed by conducting metallographic and chemical studies to investigate the contact between the sample materials. Results show that the optical monitoring system allows quality criteria to be verified in real time while combining diverse materials using PBF-LB techniques.

2.1.4.1 Materials and methods

Two steel powders were used in the interaction investigation between the two distinct materials. The first powder is AISI 316L austenitic stainless steel, which is supplied by Mimete Metal Powders and is frequently used in powder bed additive procedures to fabricate components. Maraging 18Ni (300) steel, supplied by GE Additive, is the second material. The powder chamber of a Concept Laser PBF-LB machine (M1 Cusing type) was filled with the two powders, which had particle sizes between 15 and 45 microns. An ad hoc piece of equipment that had already been tried and tested in other projects was utilized to ensure that the powders stayed well separated throughout charging. The powder loading chamber was split in half by this apparatus [53,60]. Later, by letting the granules come into contact with one another but preventing them from mixing, this division system was removed. The two materials then developed a clean, straight contact (see Figure 26).

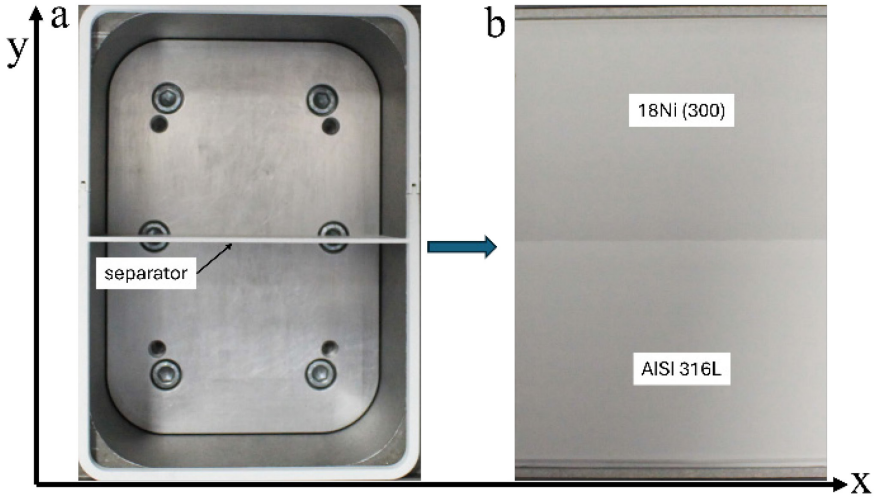

Figure 26 - (a) Powder loading chamber with the separator inserted into it; (b) Appearance of the two powders after separator extraction.

The machine employs a rubber knife that translates along the X direction to move powders from the powder platform to the construction platform and spread them in the shape of a bed of uniform thickness.

Selected process settings were employed for the specimen fabrication, drawing from earlier tests that produced specimens with no flaws and densities above 99% for AISI 316L steel [61].

A Canon EOS 5Ds camera aimed to frame the powder bed region impacted by the laser fusion process was used for optical monitoring. During the scanning of each layer, the camera was configured in bulb mode to record the radiation that the materials released as the laser beam made contact with them. Previous papers [42,190] have provided thorough descriptions of the monitoring approach used. An example of the images taken during real-time optical monitoring and used in the ensuing analysis process is presented in Figure 27. The resolution of the images was 35 μm/pixel.

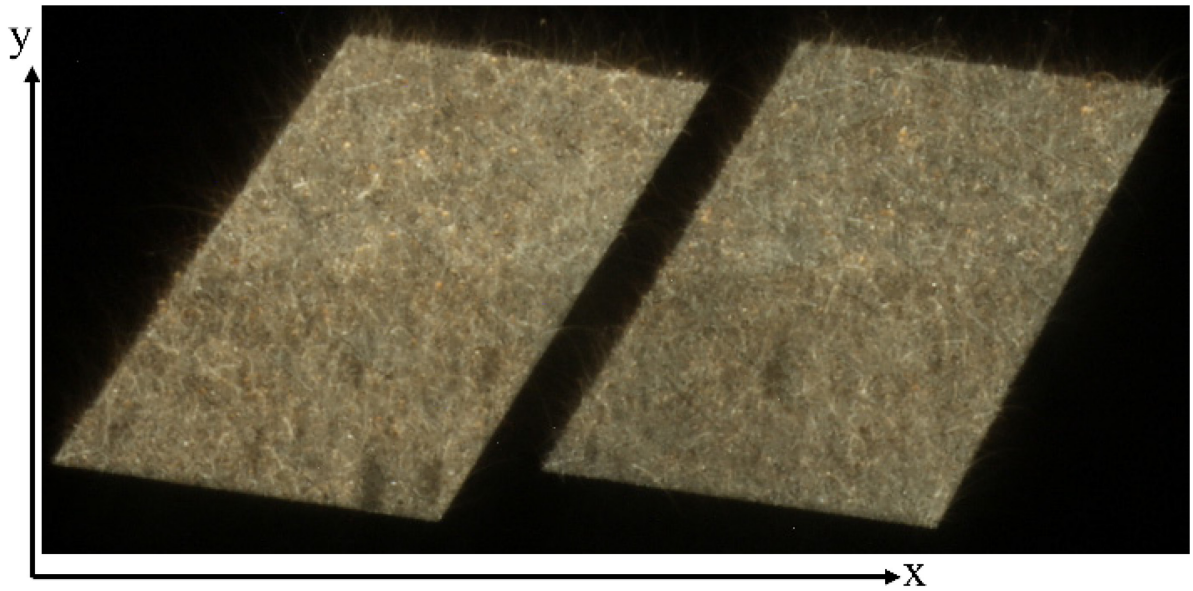

Figure 27 - Image captured during the scanning of a layer.

We made parallelepipeds that measured 25 x 60 x 5 mm. Following their removal from the construction platform, the specimens underwent examination under an electron microscope and an optical microscope.

2.1.4.2 Results

2.1.4.2.1 Image Analysis

The analysis of the images obtained from the optical monitoring was performed using Matlab and FIJI software and was divided into the following steps: perspective correction of the

images, color-based pixel segmentation, characterization of the interface between the two materials, and statistical analysis of the results (see. Figure 28)

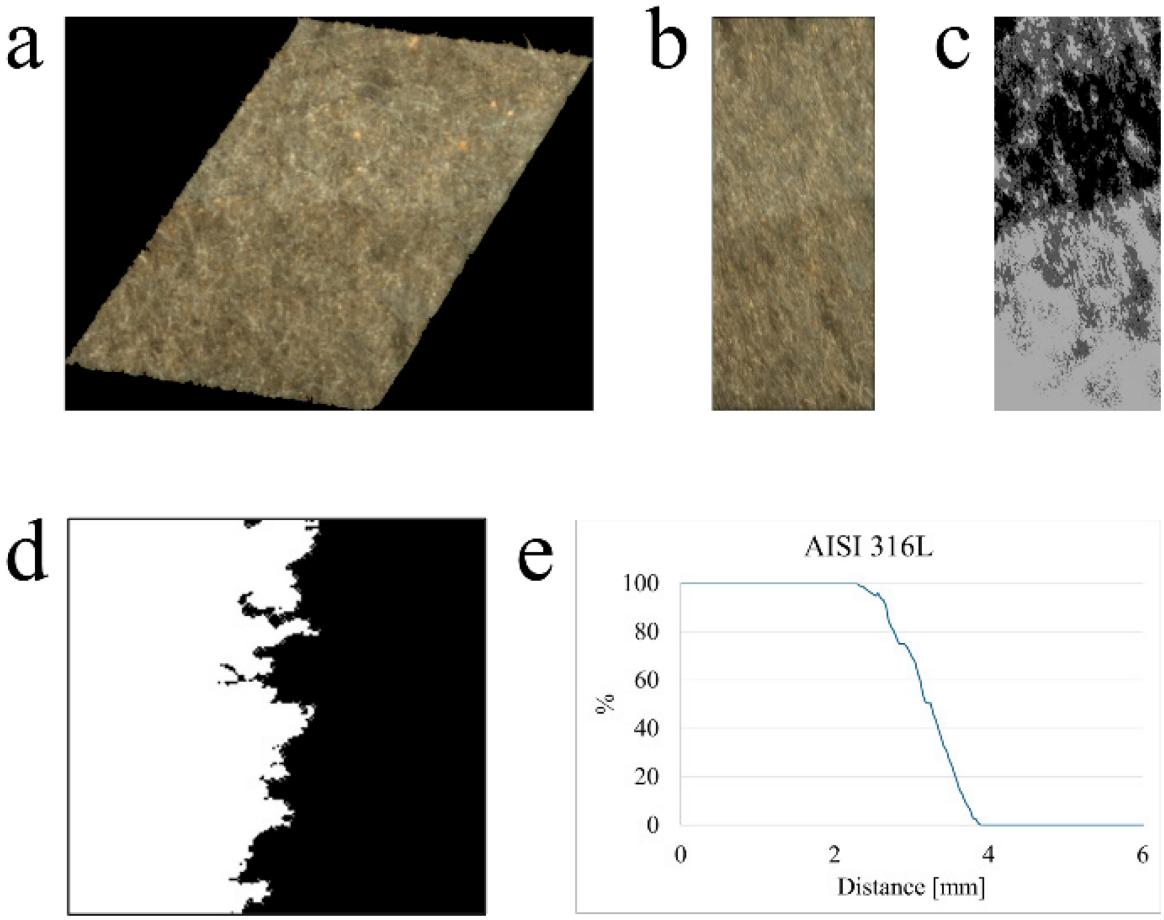

Figure 28 - Schematization of successive steps in image analysis: (a) original image; (b) perspective correction; (c) color-based segmentation; (d) enlargement of the interface between the two materials; (e) data analysis.

The process outlined above was carried out for a number of successive layers, and the various curves that represented the trends at the material interface were arranged side by side to create a surface that allowed for the observation of the change in material occurring at a spatial interval of roughly 1.5 mm (see Figure 29).

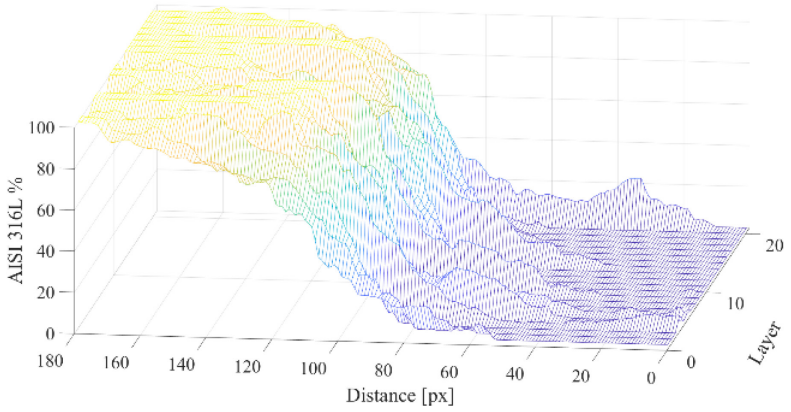

Figure 29 - Interface trend between materials obtained through analysis of monitoring images.

2.1.4.2.2 SEM Analysis

After the specimen surface was sliced and polished, a material interface examination was carried out using a scanning electron microscope (SEM) (mod. Zeiss Sigma 300 VP) fitted with an EDX microprobe for chemical analysis. Curves were derived to represent the trends in the concentrations of the two materials' distinguishing chemical constituents in the area across the interface (see Figure 30) for the case of the AISI 316L and the cobalt for the 18Ni (300) steel [151].

It is feasible to ensure that the measurement acquired by optical monitoring is in fact corroborated by the instrumental survey carried out using the SEM by looking at the graphs in Figure 30.

To visualize the degree of mixing between the two materials along the interface, a map was used for the same kind of inquiry. Figure 31 illustrates how the change from one material to another happens at a distance of roughly 1.5 mm.

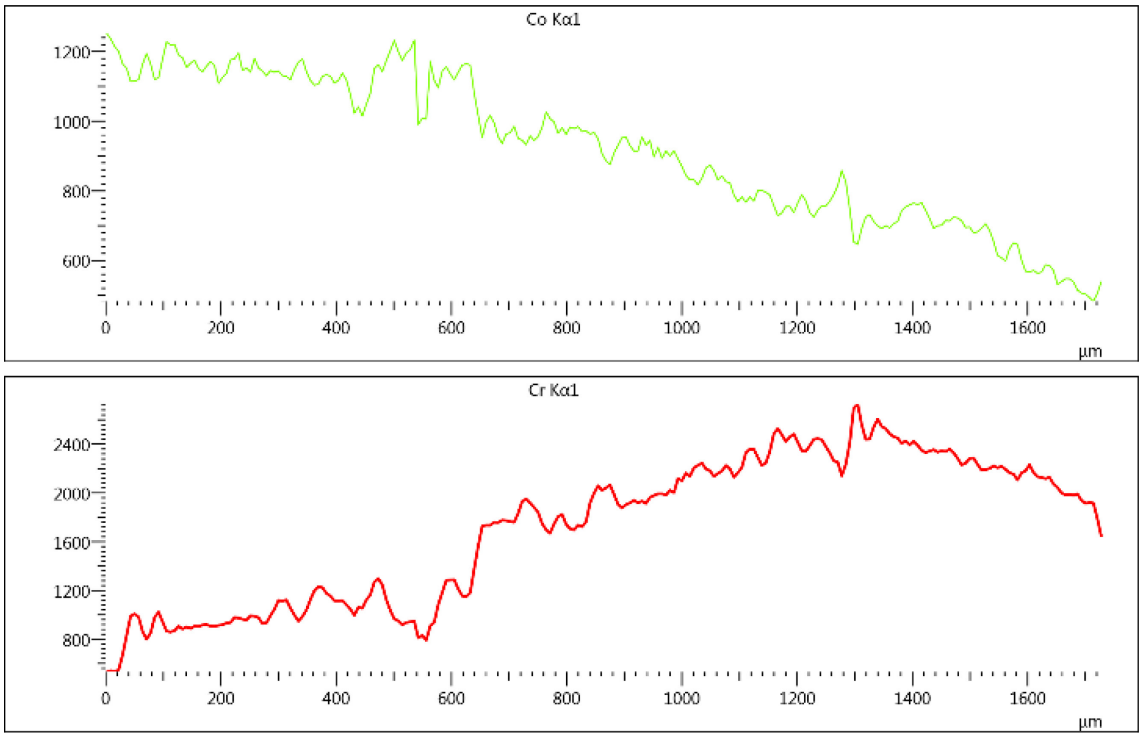

Figure 30 - Trend in Cobalt and Chromium concentration at the interface between materials. The vertical axis shows the counts of chemical elements detected by SEM.

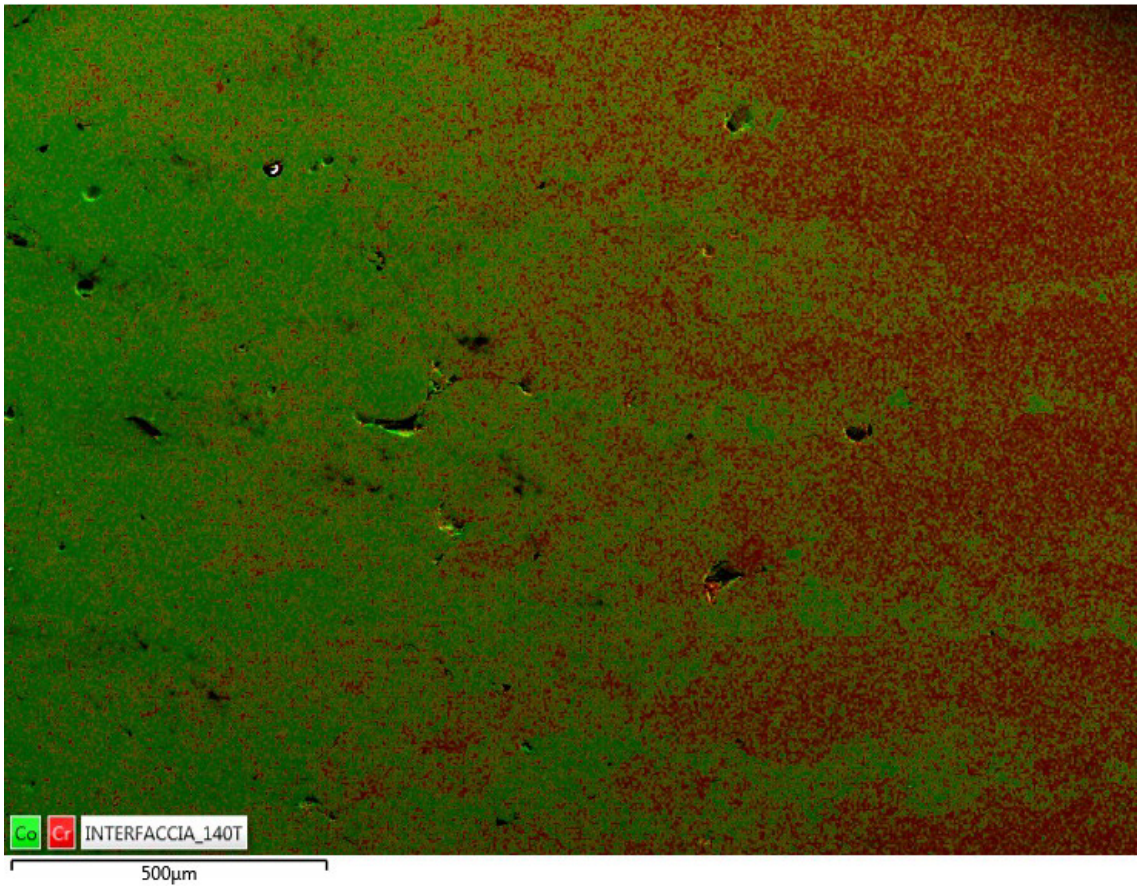

Figure 31 - Map of the concentration of the elements Cobalt and Chromium in the interface zone.

2.1.4.2.3 Microscopic examination

Using an optical microscope (Nikon Eclipse MA200 mod.), the artificial specimens were examined along axes parallel to the XY and YZ planes. To do this, the surfaces to be viewed were first prepared metallographically. Afterwards, a chemical etching was done using a reagent that included 10 milliliters of hydrochloric acid, 6 milliliters of acetic acid, 1 gram of picric acid, and 100 milliliters of ethyl alcohol.

It was possible to ascertain the two materials' microstructures, both close to and distant from the interface. The microstructure of the two may be clearly seen distant from the contact, as Figure 32a and Figure 32b demonstrate. For AISI 316L steel, austenite was clearly constituted, and for 18Ni (300), martensite.

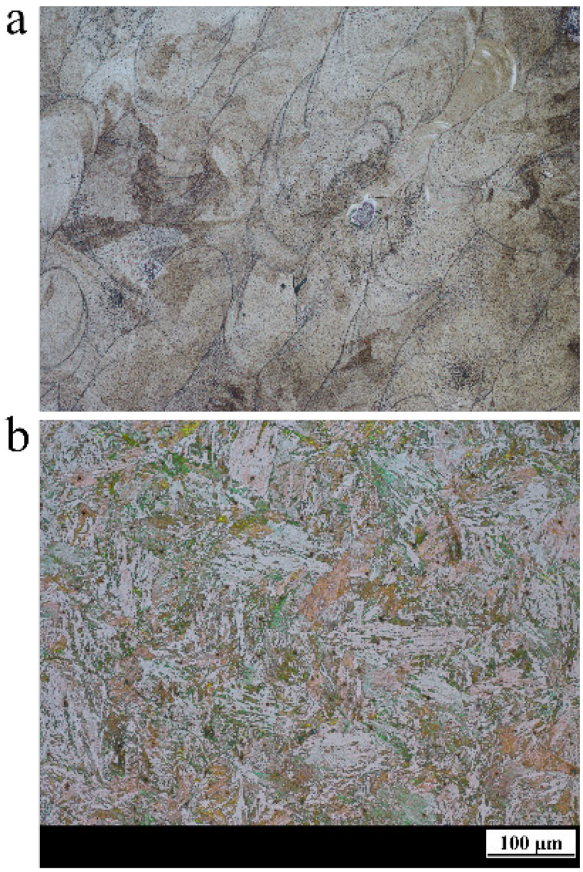

Figure 32 - Micrographs of single materials used acquired away from the interface: (a) austentic structure of AISI 316L steel; (b) martensitic structure of 18Ni (300) steel.

The region encompassing the steel-steel interface was analyzed in the XY (Figure 33a) and YZ (Figure 33b) planes. A band of material that appears to have a different microstructure than the steels that were analyzed individually can be seen in both sections. This band extends about 1.5 mm in the Y direction, which is consistent with the findings of the earlier tests.

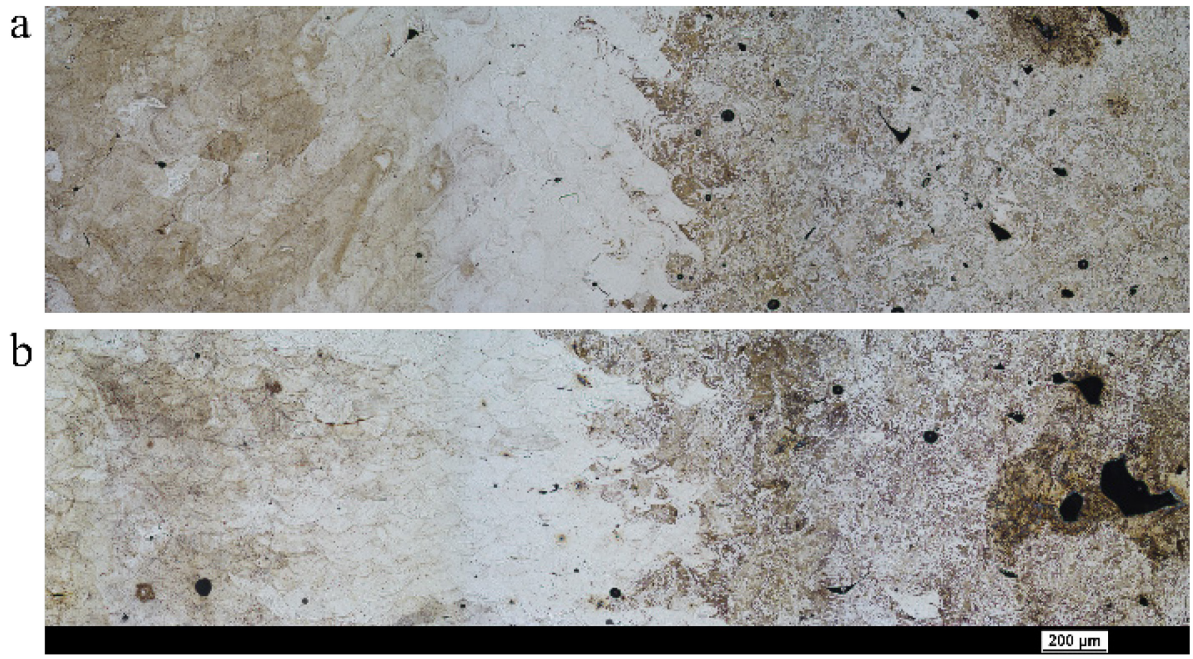

Figure 33 - Microscopic examination at the interface between materials: (a) section parallel to XY; (b) section parallel to YZ

2.1.4.3 Conclusions

• To evaluate compliance with PBF-LB process criteria, optical monitoring offers a variety of significant process data that may be extracted using image analysis techniques and statistically analyzed. Verification of the material transition's occurrence in a band with a width of roughly 1.5 mm was possible.

•If the imaging system's resolution is sufficient for the task, the outcomes can be quite similar to those that can be produced by techniques based on electron or optical microscopy.

•Even for multi-material components, optical monitoring is a practical substitute for more intrusive, expensive, and time-consuming approaches for geometric characterisation of parts produced by the PBF-LB process.

•As long as the materials react differently to the laser beam, optical monitoring of a multi-material PBF-LB process allows for the detection of cross-contamination between them.

2.2 Multi-material components with gradual transitions

2.2.1 Continuous Functionally Graded Materials (cFGMs) fabricated with PBF-LB technology at layer-level

Because the manufacturing sector operates in a highly competitive and customer-driven environment, it requires innovation to reduce costs and foster flexibility in order to achieve sustainable corporate growth. In order to do this, science and technology are continuously creating novel materials for cutting-edge applications for which conventional materials are unsuitable [220]. Indeed, metallurgists have created a generation of promising materials called composites for a variety of uses, including aerospace and the automobile industry [104]. Their incapacity to create parts with various chemical, physical, and mechanical qualities in a single structure, however, is their primary flaw. With so many potential uses, the ability to customize characteristics to individual requirements is becoming a very exciting challenge that is attracting the attention of both the scientific and industrial sectors [25,42]. In many industries, the need to combine opposing properties is growing, especially in high-stakes operational contexts including aerospace, biomedical implants, nuclear facilities, and more. The creation of innovative techniques and tools for the production of multi-material metal additive manufacturing (MMAM) components, both at the layer level and between layers ("very rare" considering the limitations and difficulties of realization), has filled this gap. These tools and methods are covered in great detail in the reviews by Wei et al. [20] and Feenstra et al. [9]. The ability to fabricate multi-material components with low compatibility metal alloys, such as toughness and hardness, is limited by recent multi-material fabrication, as has been widely reported in previous studies [104,49,98]. This is because the sharp boundary between the materials could result in the generation of brittle intermetallic phases, the concentration of thermal stresses, solubility limitations, thermal property mismatch, etc.

This experiment's primary goal is to provide a novel process for layer-by-layer production of continuous functionally graded materials (cFGMs) using a traditional blade-based Powder Bed Fusion – Laser Beam (PBF-LB) system. In this work, two steels with distinct mechanical, chemical, and physical characteristics—AISI 316L and 18Ni Maraging 300—were employed. To obtain the cFGM structure, a gradual continuous transition zone was formed between the two materials. This was accomplished by creating a working powder separation system that is simple to install on the PBF-LB machines that are currently in use. This work demonstrates that is possible the layer-level fabrication of a cFGM component using a traditional PBF-LB machine and a blade/roller powder distribution approach. This is significant because, as the literature [49,98] notes, this approach is very limited for intralayer multi-material fabrication.

Furthermore, this is the first experiment to monitor the presence of a graded transition zone between two materials layer by layer using an in-situ optical monitoring system. The viability of the intralayer fabrication approach developed and presented in this paper has been proved by the successful completion of mechanical, microstructural, chemical analysis, and optical monitoring tests on cFGM samples. Since these results may be obtained without changing the machinery and by using cheap extra equipment, they can be quickly and affordably adopted.

2.2.1.1 Materials and methods

2.2.1.1.1 Advanced experimental manufacturing method for FGMs: samples fabrication & materials

For the purpose of fabricating cFGM structures at the layer level, a detachable powder separation system that would be placed inside the powder platform was created (see Figure 34). The goal of this system's design was to create a zone of progressive and seamless transition between the two materials (Figure 35). The powder platform can be divided into two prismatic sections by tilting the wall that makes up the powder separation system with regard to the direction of movement of the blade (see Figure 34 and Figure 35). To provide a progressive transition zone with changing length, the wall was constructed with two different inclinations: Set-up 1, which has a 25mm interface width, and Set-up 2, which has a 10mm interface width. For instance, the controlled mixing of powders in the case study of the 25 mm interface length (Set-up 1) is depicted in Figure 34. As shown by the dotted lines, the mixing occurs within a precisely defined region of the powder bed with a 25 mm extension that was specified during the powder separation system's design. The powder bed is shown in the Figure 35 following the preparation of the powder chamber. The divider dictates the shape of the volumes formed, and the progressive and continuous transition zone between the two materials can then be obtained as the blade travels over the building platform.

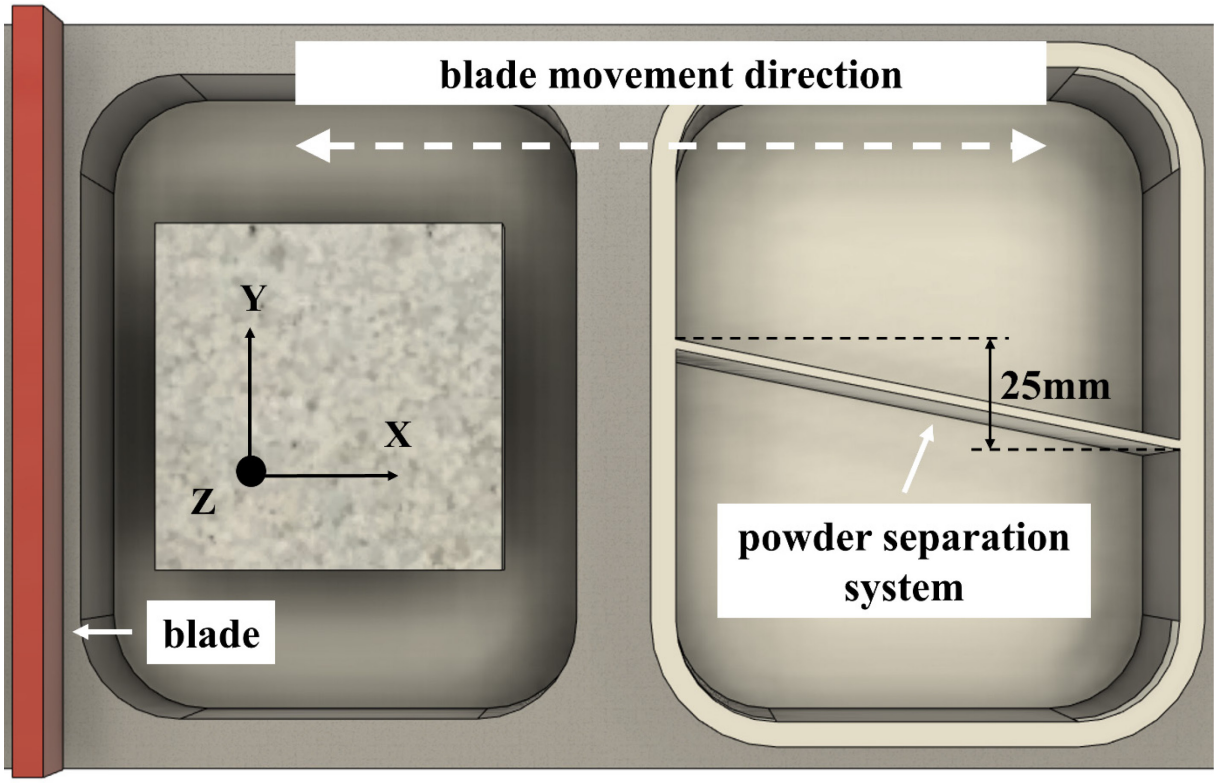

Figure 34 - Configuration 1 (with a 25 mm interface length) for the blade-based PBF-LB machine to fabricate continuous functionally graded materials (cFGMs) at the layer level.

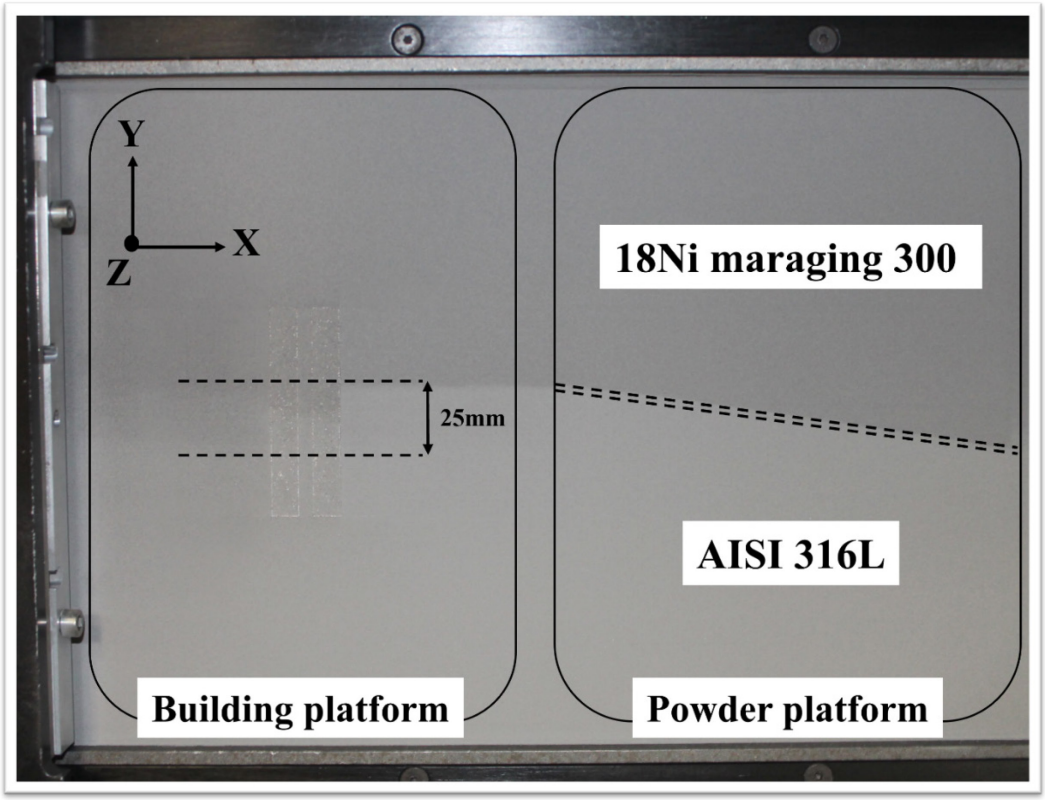

Figure 35 - The appearance of the powder bed after filling with powder and covering the blade, after removing the divider: the powders are well separated.

Initially, Set-up 1 was used to evaluate the performance, quality, repeatability, and efficacy of the used approach. Two 75x12x12 mm parallelepiped samples (Sample 1 and Sample 2 in Figure 36) were made with a traditional M1 Concept Laser machine. The PBF-LB testing system, in particular, features a diode-pumped Nd: YAG solid-state laser with a wavelength of 1064 (nm). The laser power output of the system may reach a maximum of 100 (W), with minimum layer thickness of 20 (μm) and maximum laser spot width of 200 (μm). These systems are severely constrained for the manufacture of multi-materials at the layer level because the PBF-LB system uses a powder feed system with a chamber from below and a powder spreading technique based on the employment of a blade [49,98].

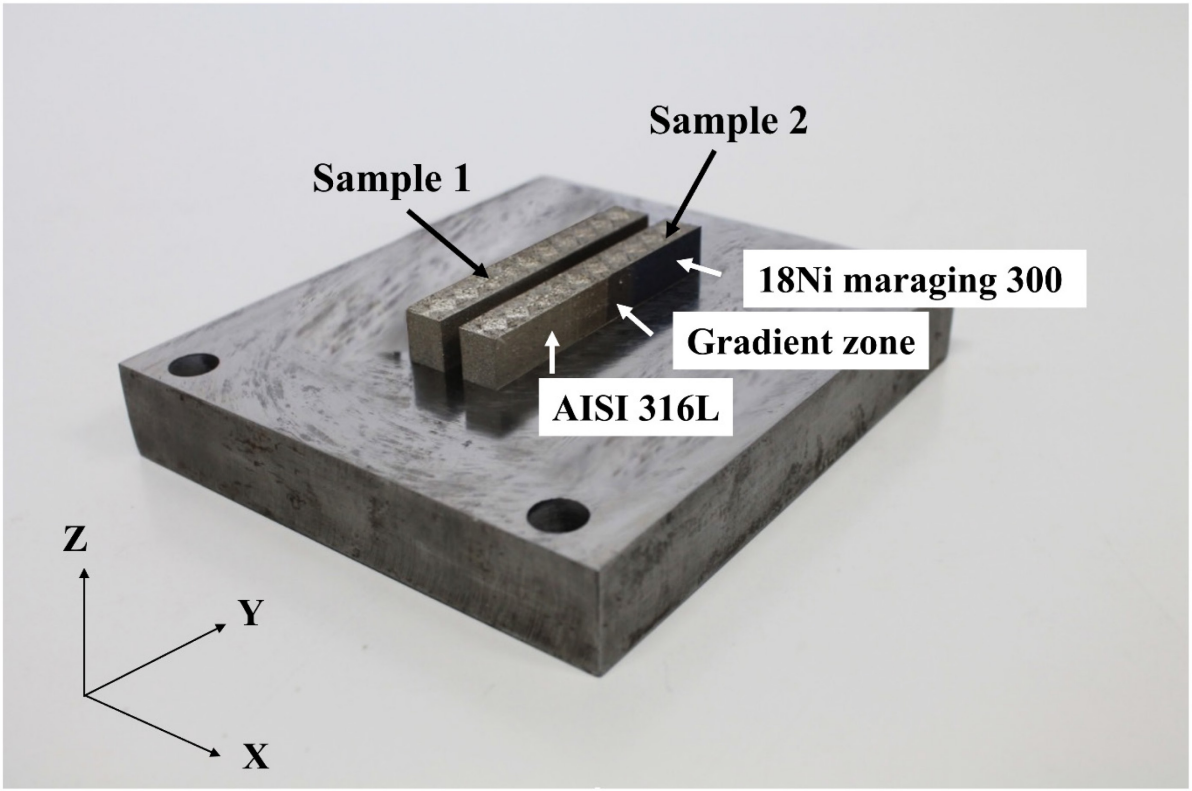

Figure 36 - Macrograph of printed cFGM specimens.

The same process parameters that had been improved in earlier studies were used to create each sample [60]. Therefore, the identical set of process parameters was applied to the entire laser-scanned surface in order to test the advanced experimental manufacturing approach described in this study, despite the fact that these are two unique materials. In particular, 100 (W) of laser power, 180 mm/s scanning speed, 200 μm laser spot size, 140 μm hatch spacing, and 30 μm layer thickness were employed. Furthermore, the 5 × 5 mm^2 samples were created using the random island scanning technique. The random approach and the island size were both selected

to lessen the thermal strains brought on the printing [129]. It was possible to fabricate specimens with a relative density > 99% using this combination of process settings.

Samples from Set-up 2 were also created later, after the methodology's suitability for testing on Set-up 1 had been evaluated, in order to compare the mechanical, metallographic, and chemical properties of the two configurations.

In particular, the final mechanical properties of the two cFGM configurations (Set-up 1 and Set-up 2) studied in this work were compared with the single materials and bi-materials that the same scientists had previously looked at [60]. Two batches of cFGM specimens with Set-up 2 (specimen ID: G10_n) and Set-up 1 (specimen ID: G25_n), with n being the number of specimens ranging from 1 to 5, were produced for this purpose, each batch containing five tensile specimens per interface length. Specifically, the dogbone-shaped samples were made in compliance with the ASTM E8-21 standard for powder metallurgy. To evaluate the mechanical quality of cFGM, a gradient zone was made at the middle of the specimens. In addition, a parallelepiped-shaped test specimen (10 x 10 x 30 mm) was created for chemical and metallographic analyses for each batch. The specimens created to conduct a thorough characterization of the sophisticated experimental cFGM generation process described in this paper are displayed in Figure 37.

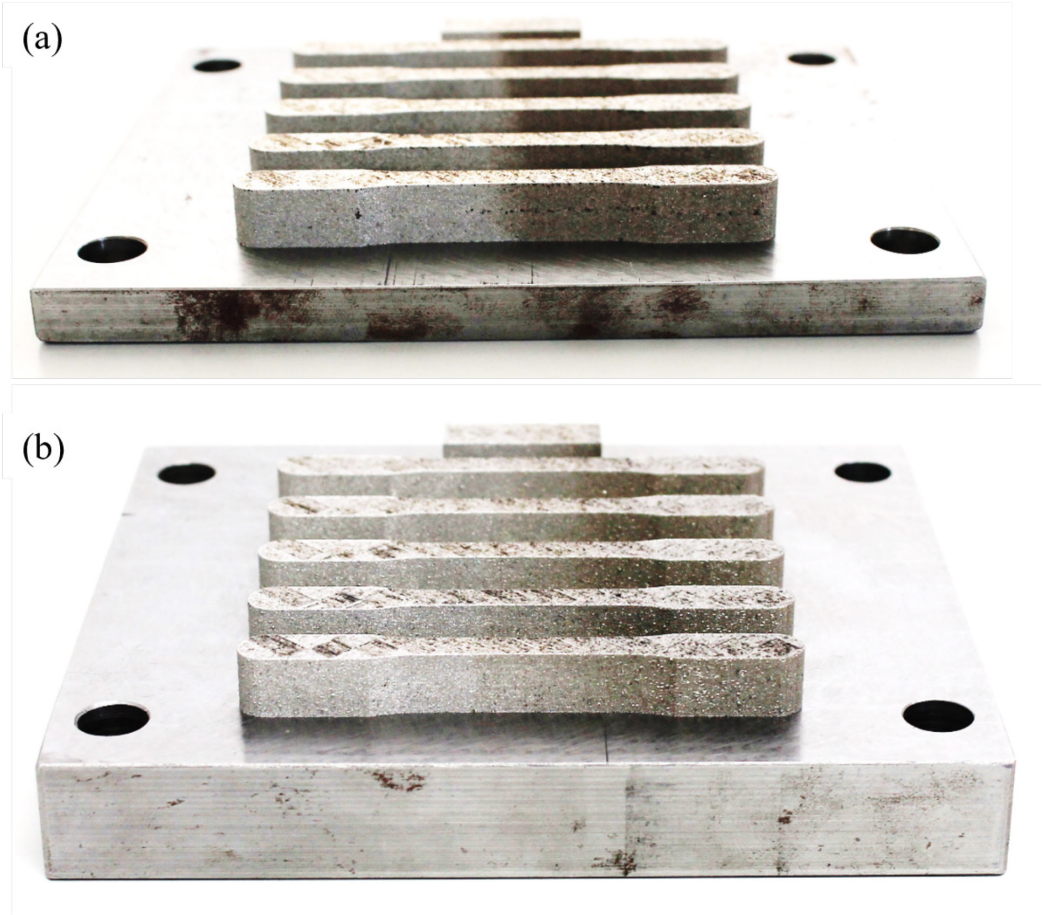

Figure 37 - samples of layer-level continuous functional graded material (cFGM) made using the PBF-LB technique. (a) 10 mm interface length cFGM specimens. (b) 25 mm interface length cFGM specimens.

The two materials that were looked into in this study for the creation of cFGM structures were AISI 316L stainless steel (powder supplied by Mimete Metal Powders) and 18Ni Maraging 300 steel powder, which was provided by GE Additive. The two materials are produced by gas atomization, using nitrogen for AISI 316L and argon for 18Ni Maraging 300, resulting in spherical powders with sizes between 15 and 45 μm. The spherical particles of the powder materials employed in this investigation are displayed in Figure 14. The nominal chemical composition of the two metals, as verified by the suppliers, is displayed in Table 2. The 18Ni Maraging 300 particles contain Co and Ti, which are not present in AISI 316L, but lack the chemical components Cr, Mn, and Si that are present in AISI 316L powders. The percentages of other elements, such as Ni and Mo, also vary significantly. The physical and mechanical qualities of these materials differ due to their distinct chemical compositions [188]. For example, the 18Ni Maraging 300 material exhibits greater wear resistance, whereas AISI 316L is non-magnetic and has strong chemical corrosion resistance [189,151]. Because 18Ni Maraging 300 steel has a higher strength and a lower ductility than AISI 316L stainless steel, its combination may provide a means of producing materials that are resilient yet still strong

enough to avert catastrophic failure. Additionally, it is challenging to fabricate the two materials as a single component without introducing manufacturing faults due to their extremely divergent thermal properties (heat capacity and coefficient of thermal expansion) [147]. A continuous and progressive transition zone was developed between the two materials that make up the final cFGM structure in this study in order to prevent manufacturing faults and to ease the concerns with thermal compatibility between the two materials. In order to improve the mechanical properties of the 18Ni Maraging 300 steel, all specimens were finally heat treated. Specifically, they were solution annealed at 815°C for one hour, followed by air cooling, and then hardened at 480°C for five hours, followed by air cooling. Ben-Artzy et al.'s research [147] indicates that this heat treatment has very little effect on AISI 316L.

2.2.1.1.2 In-situ optical monitoring system & novel image processing method

To confirm the overall stability of the process and identify any unusual deviation of the built layers, a high-resolution monitoring system (detailed in detail in [221]) was employed as real-time optical process monitoring. Specifically, a Canon EOS 5Ds camera with a 50 Mpx CMOS sensor fitted with a Canon TS-E 90 mm f/2.8L Macro lens was used. The Set-up 1 mentioned in Section 2.2.1.1.1 served as the subject of the investigation. In particular, in contrast to earlier research [221], a tilt-shift lens and a camera with a higher resolution (50 Mpx > 24.2 Mpx) were utilized in this study to observe the gradual transition zone between the two materials in greater detail. This allowed for the reduction of perspective distortion and the utilization of the distinct light emission resulting from the laser-matter interaction, which was made possible in this work by the presence of two different materials in a single layer. In order to get a deep depth of field and preserve the information within the layer, the camera's minimum aperture was also set to f/45 and the exposure duration was adjusted to match the single layer's scanning time. Lastly, to reduce the quantity of light recorded and, consequently, the amount of splatter or light interference not coming from the print, a Neutral Density (ND) filter with an ND value changeable from ND3 to ND1000 (1.5 to 10 f-stops) was mounted to the lens. To meet the desired goals, new techniques for image analysis have been created. The image analysis's specific goal was to examine the consistency and gradualness of the material mixing for each layer as well as the entire print. The analysis was performed with suitable algorithms created with Matlab (Image processing and Computer Vision Toolbox Release 2023) and ImageJ (https://imagej.nih.gov/ij/).

2.2.1.1.3 Metallographic and mechanical characterization of the printed samples

A metallurgical and mechanical assessment was carried out to explore and evaluate the viability of the cFGMs layered structure described in this work and to assess the final quality of the specimens generated utilizing this unique technological solution. To be more precise, in order to assess any flaws in the as-built specimens, the parallelepiped-shaped metallographic specimens were suitably prepared by cutting, mounting, and polishing processes (down to 0.04 µm polishing cloths). Metallographic preparation was done in compliance with the industry standard test procedure for assessing material microstructure (E 407). The cuts made to the Set-up 1 specimens are depicted in Figure 39, along with the matching sections that were obtained (transversal (YZ plane) and longitudinal (XY plane) with respect to the layer), on which all mechanical and metallographic analysis was done.

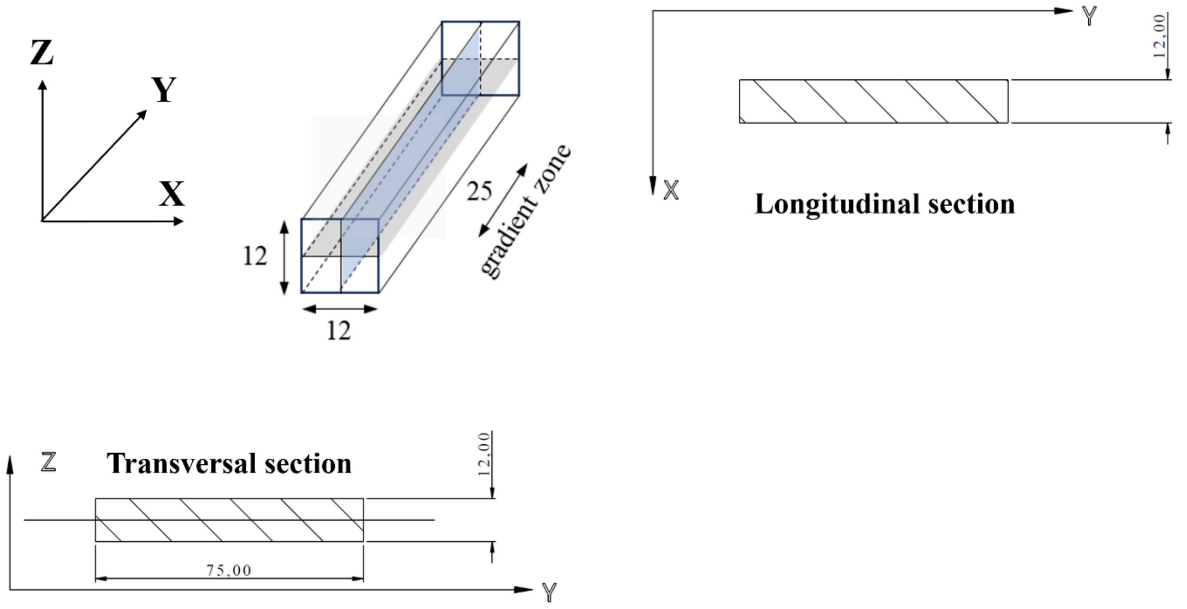

Figure 38 - Cut-up plans made on the test specimens to create the survey sections.

A digital camera was used to take pictures and a Nikon Eclipse MA200 inverted optical microscope was used to study the specimens that were created in this manner. The prepared specimens' discontinuities were assessed from the extracted micrographs; specifically, the specimens were split into six study areas, each of which corresponded to five millimeters of the specimen, and the discontinuities were assessed using image analysis algorithms created with ImageJ software. Sections that were longitudinal and transverse were both studied.

The same specimens were also subjected to microstructural, chemical, and phase analytical studies in order to evaluate the interfacial bonding between the two materials and analyze in detail the graded zone generated in the cFGM components. The samples underwent a two-step chemical etching procedure to highlight their microstructure. The martensitic microstructure of

the 18Ni Maraging 300 material was first highlighted with Nital 3%, and the austenitic microstructure of the AISI 316L material was next highlighted with Glyceregia reagent.

In accordance with ISO 6507-1, Vickers HV03 hardness tests were performed on the entire metallographically studied section using a Shimadzu micro-Vickers tester HMV-G to assess the mechanical property transition in the interface zone.

2.2.1.2 Results and Discussion

2.2.1.2.1 Optical monitoring analysis

Because the camera exposure period was chosen to match the amount of time required to finish scanning a single layer, as described in section 2.2.1.1.2, one image was taken for each individual layer during the manufacturing process without sacrificing any print information. To allow for independent analysis of the two samples, the photos were divided. The images were perspective corrected to account for the camera tilt from the direction parallel to the X-Z plane before the suggested image analysis techniques were used (see Figure 40a). Next, a 30 mm center slice was taken from the pictures in order to concentrate the study on the material mixing zone (which in Set-up 1 equals 25 mm) (see Figure 40b). A unique Look Up Table (LUT) was added to the images to increase the contrast between pixels in order to better highlight the color trend in the cFGM area due to the differing laser-matter interaction caused by the two different materials (see Figure 40c).

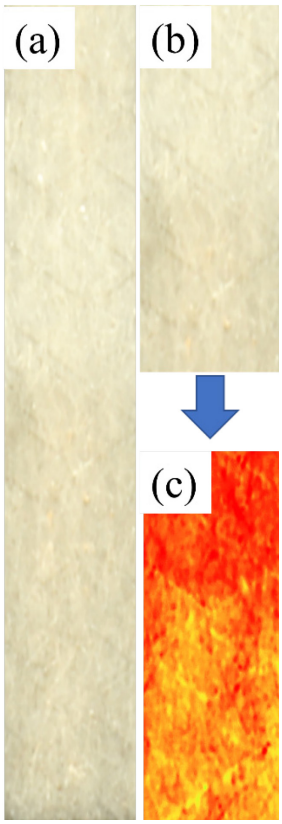

Figure 39 - (a) Image obtained from long-exposure photographic monitoring while scanning a layer. (b) Central 30mm portion of the image containing the material mixing zone. (c) Colour contrast enhanced using LUT.

Pixel clustering, or "color clustering" in machine learning, was used to segment all photos using the K-means technique. Based on the RGB levels of the pixels, which are divided into three grey scales—the lightest corresponding to 18Ni Maraging 300 and the darkest to AISI 316L—this color clustering method is carried out. Thus, the mixing zone between the two distinct steels is associated with the intermediate shade. Following image processing, each pixel displayed a value between 0 and 2, which corresponded to the three gray scales (Figure 41a). A numerical vector representing the percentage of material present in each plotted point was created by adding the values of the pixels in the segmented image taken in the column. Thus, a graph showing the trend of the 18Ni Maraging 300 steel percentage could be obtained (see Figure 41b).

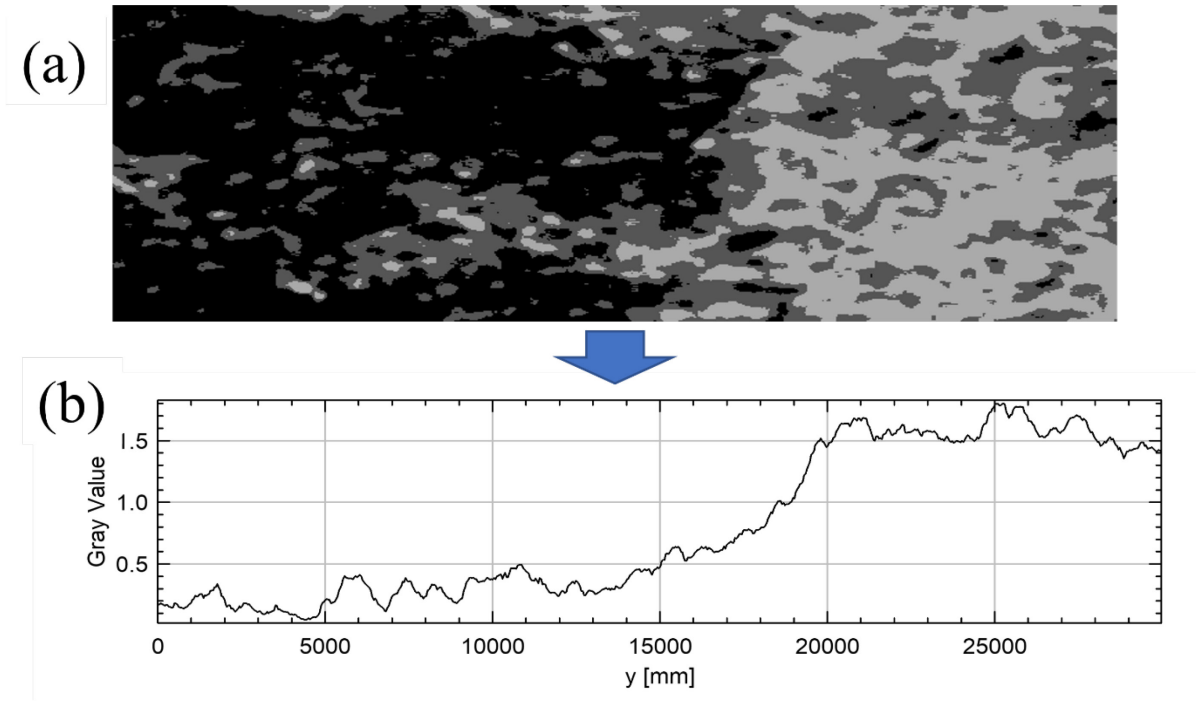

Figure 40 - (a) Result of applying the Color Clustering process to the monitoring image. (b) Trend of the layer composition obtained from the grey level analysis.

For both samples, the same analysis was conducted on 314 consecutive layers, and the outcomes were displayed on a mesh surface (see Figure 42).

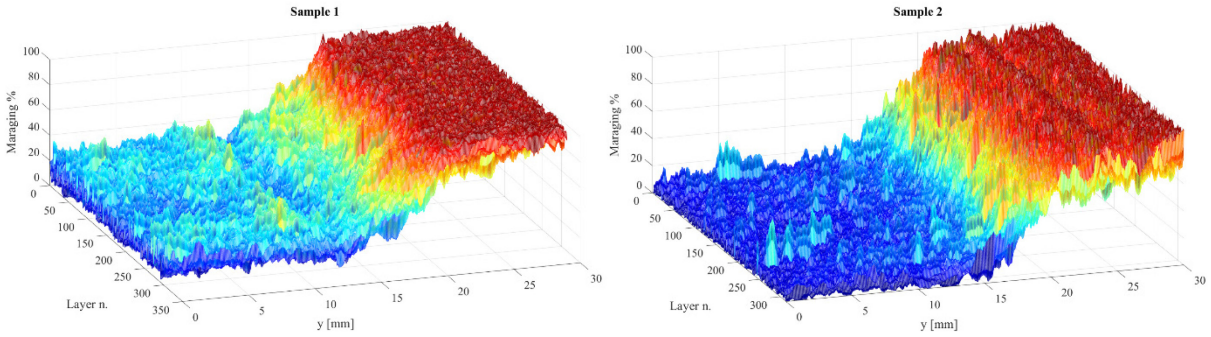

Figure 41 - Surface area obtained from the union of data collected on 314 consecutive layers.

The outcomes demonstrate how the materials respond to the laser light in various ways, making it possible for the camera sensor to discriminate between them. In all of the layers examined, the transition between the two materials is smooth and retains good repeatability, demonstrating the process' general stability and the lack of any aberrant deviation. To examine the results in further depth, the graphs of the first, middle, and last layers for each sample can be viewed (refer toFigure 43). In both situations, the three curves (Figure 43a-b) may be well

superimposed to show that the manufacturing process is kept steady throughout and that the optical monitoring done can quantify the range in which the observed values are placed. The difference between the maximum and minimum values of the curves in Figure 43a-b for each measurement point is actually displayed in Figure 43c-d. Considering the inherent variability of such a collecting and analysis method, the average variance between the highest and minimum values is roughly 11%, which is an acceptable result.

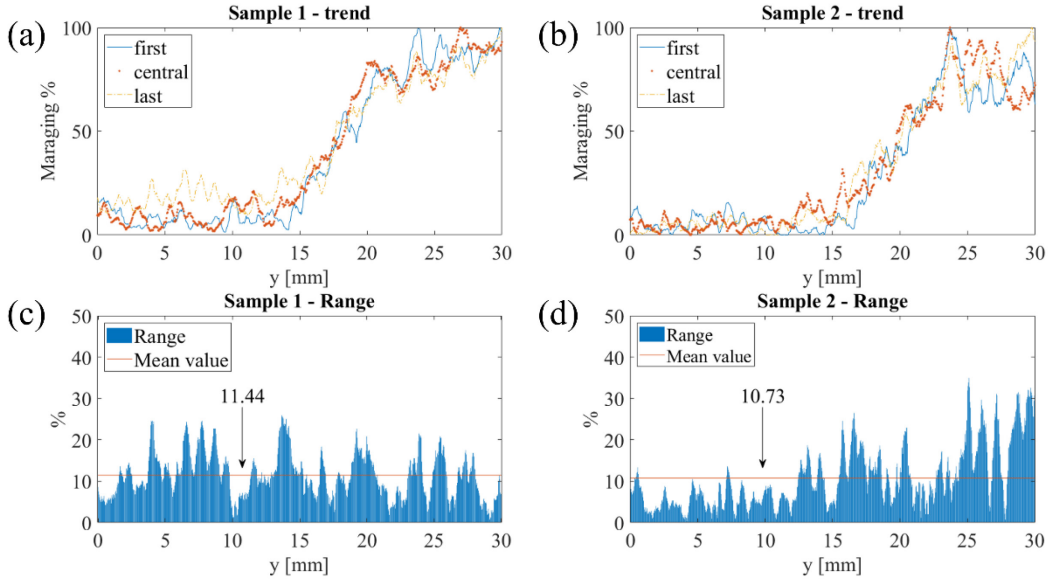

Figure 42 - (a-b) Graphs showing the trend of the percentage of 18Ni Maraging 300 steel evaluated by image analysis in the first layer, in the middle layer and in the last layer of samples 1 and 2, respectively; (c-d) Values of the intervals of variation of the concentration of 18Ni Maraging 300 for sample 1 and sample 2, respectively.

Analyzing the values in the middle of each layer on a plane parallel to the X-Z plane produced another intriguing finding (see Figure 44). In this position, 50% 18Ni Maraging 300 should theoretically be observed. The plots and computed averages show that the experimental data support this prediction. But contrasting the two specimens It is evident that the production process was unaffected by the two samples' placement on the building platform. It can also be stated that there was no inter-sample interference caused by the powder bed coating blade movement, which could have negatively impacted the production process's repeatability.

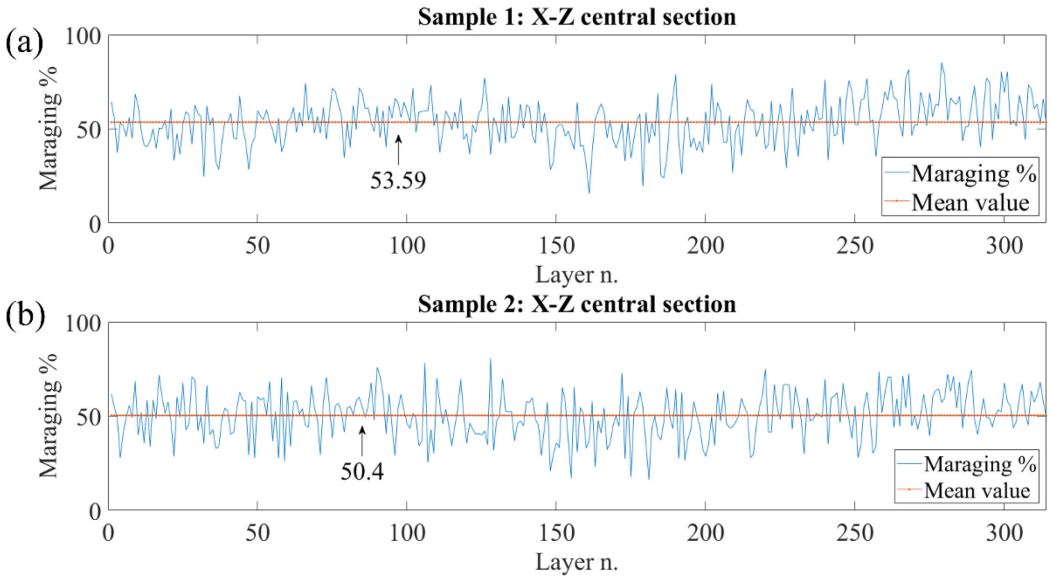

Figure 43 - (a-b) Trend of the percentage of 18Ni Maraging 300 steel measured in the section parallel to the X-Z plane and in the central position of each layer with the average value indicated.

2.2.1.2.2 Interfacial metallurgical and mechanical characterization

As can be seen from the optical microscopy pictures in Figure 45, the metallographic samples were inspected prior to etching to identify flaws such porosity or absence of fusion, which were categorized based on their location in the direction of the transition between the two steels. The average values of the samples created using Set-up 1 as detailed in Section 2.2.1.1.1 are the results shown inFigure 45. In order to encompass the intended 25 mm transition zone between the two materials, the examination area was limited to a rectangular region measuring 30 x 7.5 mm^2 and centered on the entire specimen. The graph in Figure 45a demonstrates how the porosity progressively decreases from 18Ni Maraging 300 to AISI 316L in both the longitudinal and transversal sections. It begins with a porosity value of 0.8% in the extreme left area, which corresponds to the area of 18Ni Maraging 300 alone, and ends at a value of 0.01% in the extreme right area, which corresponds to the area of AISI 316L alone (see Figure 45a-c). These findings are consistent with previous research [222,223]. The metallurgical link between the two materials created with the layer-level cFGM technique established in this study is confirmed by Figure 45b-c, which demonstrate that the interface area between the two materials is free from defects such as lack of fusion and adhesion, delamination, and cracks.

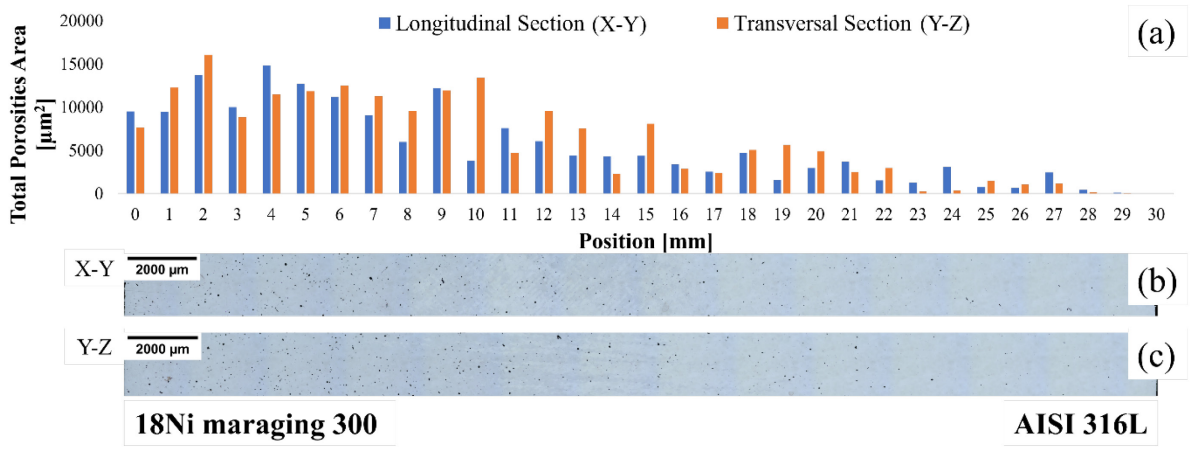

Figure 44 - (a) Porosity trend measured by image analysis on longitudinal (XY plane) and transversal (YZ plane) sections. (b) Optical micrograph of the longitudinal section (XY plane) in the as-polished state. (c) Optical micrograph of the transversal section (YZ)

The microstructural characterisation results for the same restricted area (i.e., the interface zone between the two materials) are displayed in Figure 46a-d. The samples' microstructure was made visible by a two-stage chemical etching process. First, the martensitic phase was exposed using Nital 3% (see Figure 46e). This finding validates the efficacy of the post-production heat treatment that was optimized in earlier studies [151] (see Figure 46a and Figure 46c). The austenitic phase was subsequently highlighted using the Glyceregia reagent (see Figure 46b, Figure 46d, and Figure 46f). As also shown in the study by Ben-Artzy et al.[147]), the micrographs in Figure 46 demonstrate the smooth transition between the microstructures of the two steels and the observation of an intermediate zone of dual-phase microstructure. At a higher magnification of 500x, the microstructure of each material is displayed in Figure 46e–f. The needle type's fine martensitic phase (grain size less than 1µm) can be seen in Figure 46e as a result of the age-hardening heat treatment that was applied, and the edges of the fused/re-solidified zones (roughly parabolic), which are typical of a structure produced by laser AM processes, can be seen in Figure 46f. Furthermore, Figure 46f displays the austenitic microstructure, which has an average grain size of 10 µm, which is comparatively greater than that of the martensitic phase.

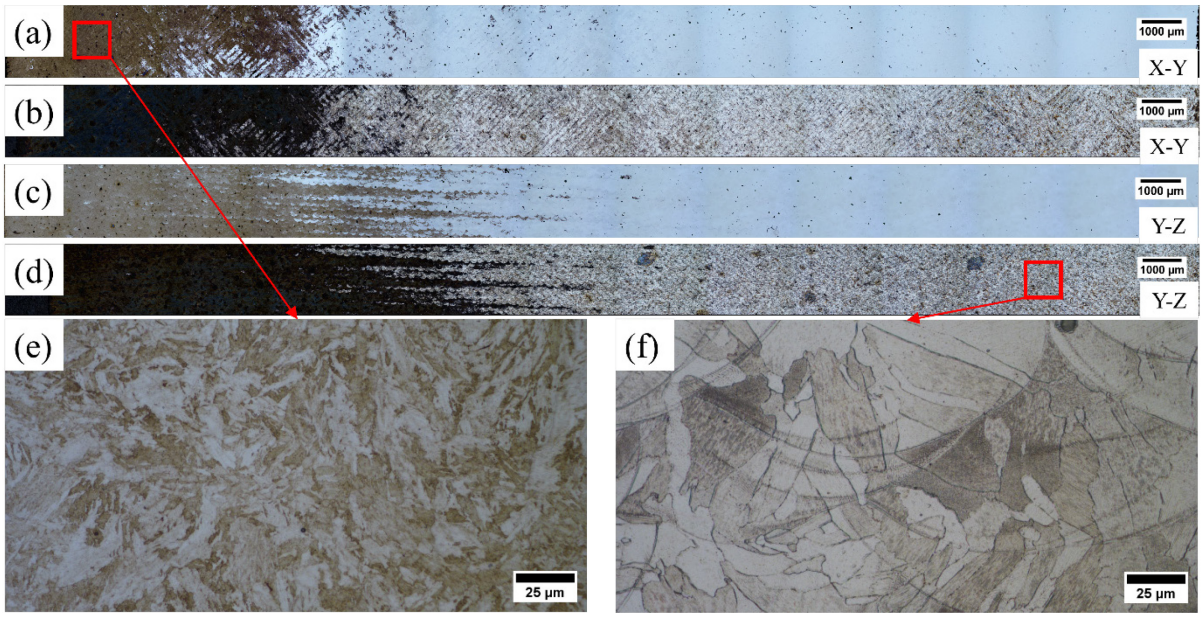

Figure 45 - (a) Optical micrograph of the longitudinal section (XY plane) in the first-step etching state. (b) Optical micrograph of the longitudinal section (XY plane) in the second-step etching state. (c) Optical micrograph of the transversal section (YZ plane).

The matching chemical concentration values of the elements that define the two materials can also be used to determine phase information. The average chemical composition, computed within the above-mentioned confined area of the samples, including the graded interface between the two materials, is displayed in Figure 47. The average values of the samples generated in the Set-up 1 as detailed in Section 2.2.1.1.1 are the results displayed in Figure 47. It is possible to confirm the existence of a continuous and gradual transition region between the two materials, very close to the desired slope of the powder separation system (Set-up 1: 25mm interface length), based on the conducted EDS microanalysis and the concentration values of the characteristic chemical elements of the two materials. In particular, the transition from a maximum value in the respective zones where the single material is present (right and left ends of the area studied) to a zero value at the opposite end where the elements are absent can be highlighted by examining the evolution of the elements Cr, Mn, and Si present in AISI 316L and absent in 18Ni Maraging 300, as well as the elements Co and Ti present in 18Ni Maraging 300 and absent in AISI 316L. The latter is a very good result since it demonstrates that it is possible to achieve zero contamination in the areas where the single material is present using the equipment described in this work. One of the restrictions listed in the literature [49,98] is the contamination issue. As a result, the fabrication of a cFGM component at the layer level with a blade/roller powder distribution approach and a conventional PBF-LB machine (with a powder chamber from below) is severely limited for the fabrication of intralayer multi-material components. Nonetheless, there are also minor variances in the weight percentages of Ni and

Mo around the region. As Figure 47 illustrates, inside the transition zone imposed by the powder separation system, the concentrations of these individual elements diffuse gradually and continuously, reinforcing the interfacial layer [224]. As evidenced by the studies of Wei et al. [36] and Tan et al. [105], the trends from the EDS microanalysis over the interface zone, displayed in Figure 47, verify a sufficient joining between the two materials.

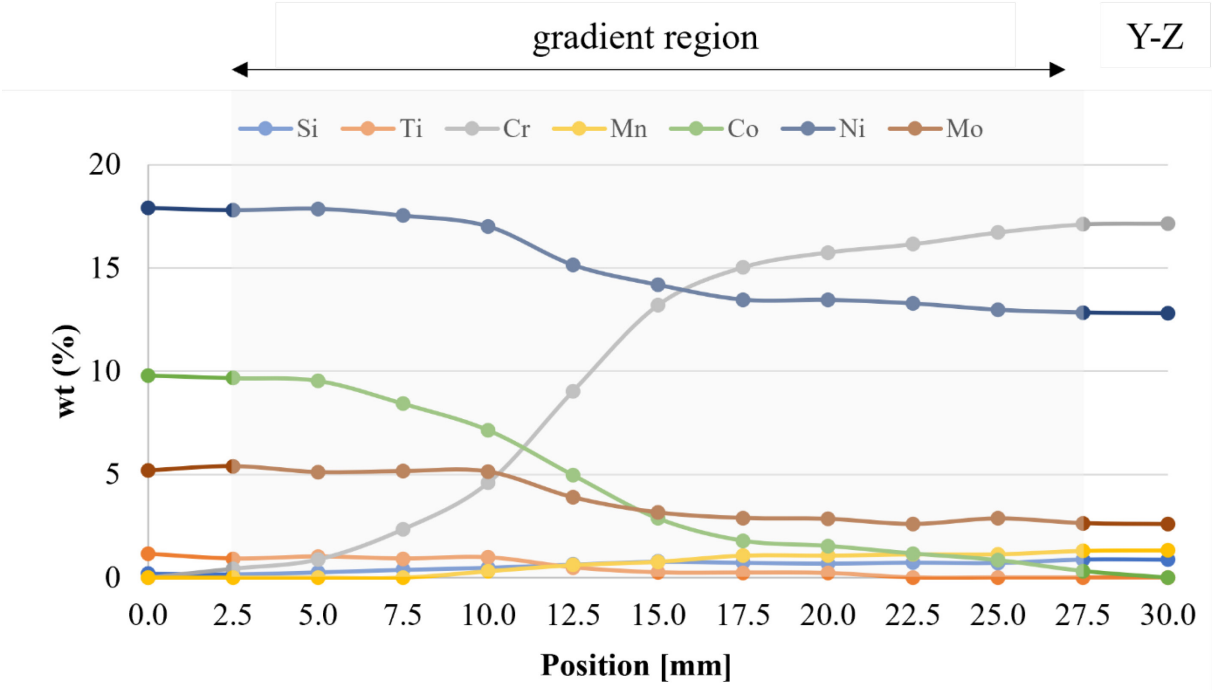

Figure 46 - Chemical composition analysis over the whole restricted area on transversal sections (YZ plane).

According to the reference system in use, the 18Ni Maraging 300 zone spans from 0.0 mm to 2.5 mm within the confines of the investigation; after that, a transition zone of 25.0 mm was established during the powder separation system's construction; and lastly, from 27.5 mm to 30.0 mm, only pure AISI 316L is present (refer to Figure 48). The sample mean values and standard deviations from Set-up 1 (explained in Section 2.2.1.1.1) are displayed in Figure 48. Specifically, the microhardness was measured over the full length of the 30 mm restricted region as well as at five different heights—1.5 mm, 3.0 mm, 4.5 mm, 6.0 mm, and 7.5 mm—within the previously described restricted area. Both the longitudinal (see Figure 48b) and transversal (see Figure 48a) sections were examined. The martensitic zone produced an average result of roughly 600HV, which is the expected value following solution annealing and aging, according to the data from both sections [225]. Additionally, the austenitic zone produced findings in the 210–230HV usual range for AISI 316L [226]. According to the work's results, the hardness in the intermediate zone decreases gradually and continuously from the martensitic to the austenitic zone, occasionally reaching softening zones (hardness near 200 HV). This softening, which occurs both before and after the heat treatment, is caused by a chemical change

that happens at a specific percentage combination between the two materials (~30% AISI 316L), which then affects the hardenability during the aging treatment (Co and Ti are the chemical elements that primarily influence precipitation hardening).

The values at the 5.0 mm position do, however, have a larger standard deviation, which is 52 HV in the transversal section and 38 HV in the longitudinal section, respectively.

The analysis's findings demonstrate that the material transitions gradually and within a range that is extremely similar to what the powder separation system's designer intended. This outcome provides additional evidence that the two materials were joined adequately.

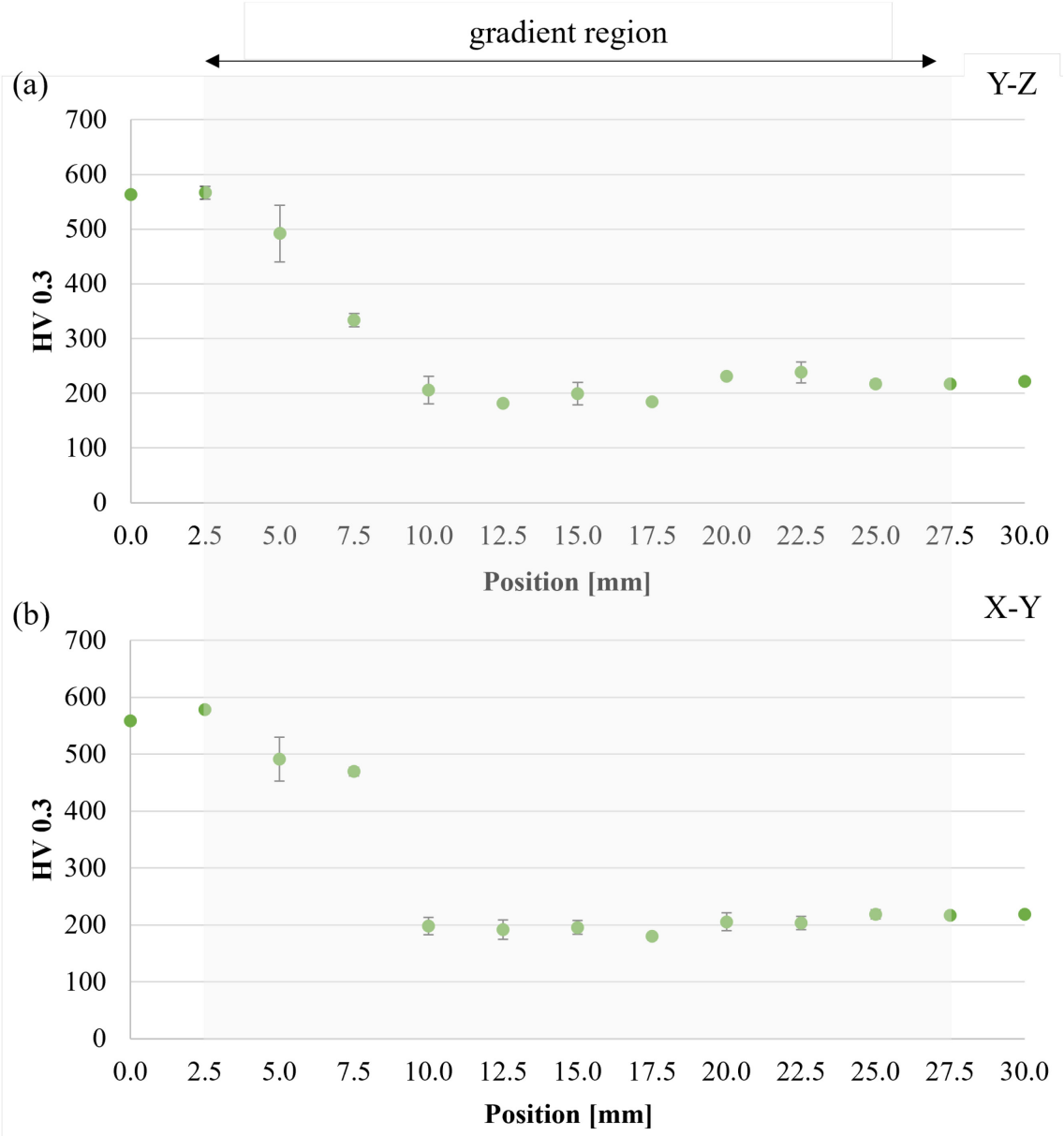

Figure 47 - (a) Microhardness trend over the whole restricted area on transversal sections (YZ plane). (b) Microhardness trend over the whole restricted area on longitudinal sections (XY plane).

Lastly, a comparative analysis was carried out between the final tensile mechanical properties of the two differentiated configurations of cFGM specimens, investigated in this work, and single materials and bi-materials previously examined by the same authors [60] in order to investigate this novel concept of a conventional PBF-LB machine. Two batches of cFGM specimens with 10mm interface length (specimen ID: G10_n) and 25mm interface length (specimen ID: G25_n), where n indicates the number of specimens ranging from 1 to 5, were produced for this purpose, with five tensile specimens per interface length. The specimen dimensions are in accordance with ASTM E8/E8M-15a. Prior to testing, the samples were polished to eliminate any possible surface flaws. Maraging samples failed wit h brittle failure and the cracks were observed to be perpendicular to the loading direction; thermal treatment makes it possible to raise the UTS by more than 40%. An average elongation at break (El) of 40%, an average UTS of 706 MPa, and a yield strength of around 607 MPa are achieved. Although the bi-material samples (B1 and B2) had a shorter plastic stage and a lower yield strength than the AISI 316L stainless steel, their stress-strain curves show comparable tendencies.

2.2.1.3 Conclusions

In this experimental work, a typical PBF-LB machine with a blade-based powder spreading method was used to create samples of continuous functionally graded materials (cFGMs) within the same layer for the first time. This was accomplished by dividing the powder chamber using specially engineered and constructed apparatus, which made it possible to alter the powder bed's typical composition and produce a seamless and gentle transition between the two materials (in this case, AISI 316L and 18Ni Maraging 300). With this accomplishment, machines and processes that are currently in use have advanced significantly. The goal was to integrate multi-material manufacturing at the layer level using an affordable, flexible, and simple-to-implement technology, thereby modifying the PBF-LB systems that were already in use and increasing their production capacity.

The following insights were revealed by the analysis's findings:

• The presence of a transition area that is equivalent to that intended by the powder separation system and the relatively gradual transition between the two materials were highlighted by optical monitoring, which also showed that there was no contamination in the zone of pure material. Excellent repeatability was also discovered in every layer that was analyzed, indicating that the process is generally stable and that there are no anomalous

variations; the outcomes also showed that the position on the fabrication platform has no bearing on the outcome;

• Two elongated areas along the layers, perpendicular to the direction of powder deposition, are produced by a fine dual-phase microstructure of austenite and martensite, as revealed by the metallographic analysis;

• The results of the in-depth microhardness tests verified the existence of a continuous and gradual transition zone, as intended by the powder separation system. These results further verify that the two materials were adequately joined;

• The cFGM specimens, as determined by the microstructure and composition gradient, exhibited ductile behavior with good strength (UTS between 650MPa and 700MPa) and ductility (elongation at break between 24% and 28%), similar to AISI 316L;

In summary, this study shows how traditional blade-based PBF-LB systems may be efficiently modified to generate functionally graded materials continuously at the layer level through a pragmatic, flexible, and economical method. This method extends the productive capabilities of this technology to applications where the presence of different properties within the same component tailored at different points is required, thereby overcoming one of the main drawbacks of multi-material AM fabrication: the incompatibility and appropriate joining of materials with quite different mechanical properties.

2.2.2 Residual stress measurements in layer-level cFGMs components fabricated by PBF-LB process

By integrating various and customized qualities in a single structure with a high degree of design freedom, additive manufacturing (AM) offers a way to overcome the constraints of existing materials for the creation of advanced multi-material metal components [20,9]. Particularly, functionally graded materials (FGMs) that are produced using additive manufacturing and offer a seamless transition between two different materials are becoming more and more common [107]. By doing this, problems arising from a sharp interface between the two materials with disparate physical attributes are reduced. These problems include the development of brittle intermetallic compounds, solidification cracking, and the formation of more severe residual stress as a result of the abrupt change in thermal characteristics [20,54].

Measuring residual stresses in cFGM structures made of AISI 316L steel and 18Ni Maraging 300 that were produced using PBF-LB, where the continuous compositional fluctuation occurs within the same layer, is the primary goal of this work. The contour method, a destructive measurement approach that may produce a 2D map of residual stresses normal to a section plane, was employed to accomplish this purpose [227]. Due to its insensitivity to microstructural gradients, this measurement approach has been particularly popular for measurements on welds and is especially well-suited for AM components [109,227,228,229]. Furthermore, compared to other methods offering detailed data, such as synchrotron X-ray diffraction or neutron diffraction, it is easier to obtain [230,231]. Furthermore, the impact of solution annealing and aging heat treatment—both necessary to enhance the mechanical characteristics of martensitic steel—on residual stresses was examined. Lastly, the effect of using material-differentiated process parameters on the residual stress field has been investigated by adjusting the scanning speed.

2.2.2.1 Materials and Methods

2.2.2.1.1 Experimental procedures & materials for sample preparation

It was possible to create a continuous, functional gradient between two steels with dissimilar mechanical and metallurgical characteristics. In particular, AISI 316L austenitic steel and 18Ni Maraging 300 martensitic steel were examined. Due to their spherical shape and origin in a conventional gas atomization process, these powder materials are appropriate for use in the PBF-LB method. The powders were sieved to produce particles with a size range of 15–45 μm before printing. The producers supplied the chemical composition of both, which is displayed in Table 2. The paper [151] has more details on the materials that were studied.

Four parallelepiped-shaped specimens measuring 75x10x12 mm were created to examine the development of residual stresses in components composed of cFGMs within the same layer. The height of the specimens was selected in order to minimize distortion following the removal of the build platform [232,233]. The cFGM samples were manufactured using Concept Laser's conventional M1 machine, which was internally modified to create cFGM samples in the same layer [61]. The 75 mm dimension was partitioned into three areas, each measuring 25 mm. The middle section featured a seamless graded transition from 18Ni Maraging 300 to AISI 316L.

The PBF-LB procedure for fabricating the samples involved maintaining constant process parameters, except for the laser beam scanning speed. This speed was changed within the same sample, resulting in three different situations. Figure 49 illustrates that specimen AM-1 was split into two processing zones and produced using two distinct scanning speeds: V1, which was 180 mm/s on the AISI 316L side, and V3, which was 120 mm/s on the 18Ni Maraging 300 side. The scanning speed V1 remained constant for specimens AM-2 and AM-3. Specimen AM-4 was divided into three processing zones and fabricated using three distinct scanning speeds. The AISI 316L region was produced with a scanning speed of V1, the 18Ni Maraging 300 region with a scanning speed of V3, and the continuous functionally graded region with an intermediate scanning speed of 150 mm/s (V2).All samples were processed using consistent parameters, including a laser power of 80 W, a laser beam width of 200 μm, a layer thickness of 30 μm, and a track spacing of 140 μm. Figure 49 illustrates the three separate case studies that were acquired, including the replication for the second example (AM-2 and AM-3).

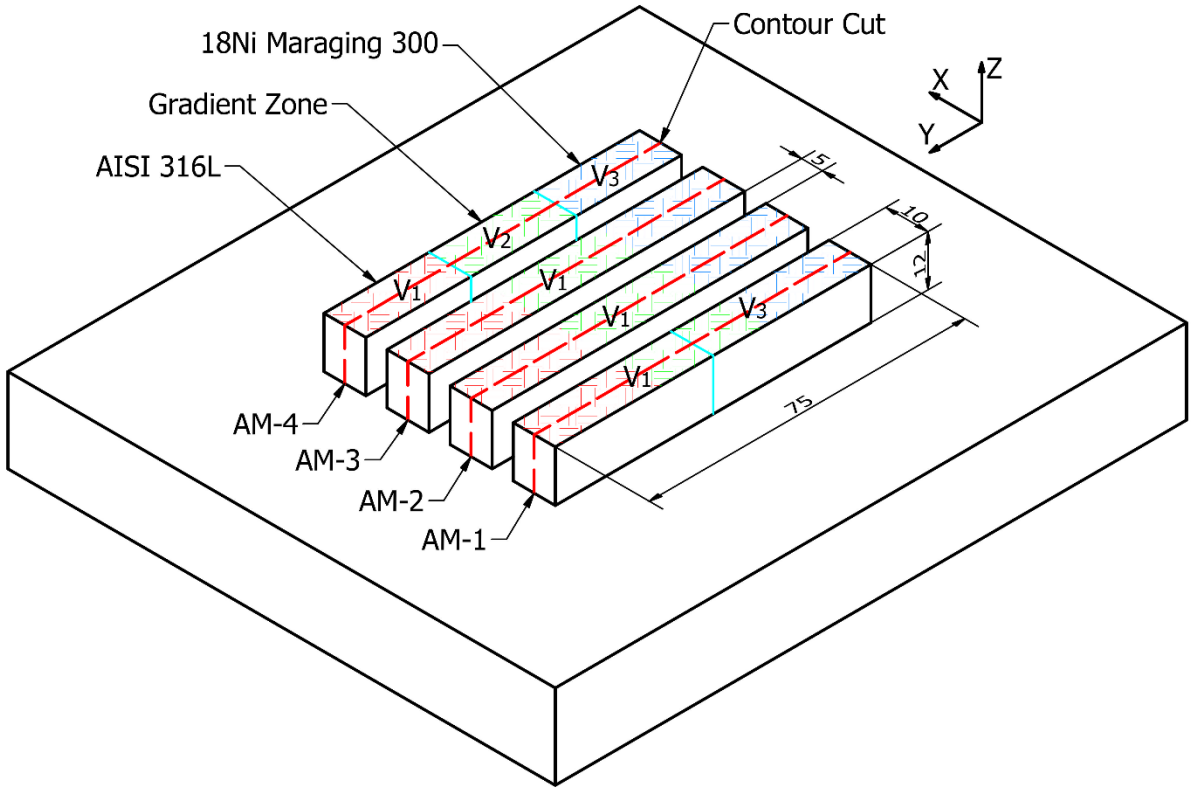

Figure 48 - Schematic illustration of cFGM sample dimensions and the three case studies. The island strategy is visible on the specimens' surface with three colors identifying the three composition zones: light red for zones wholly composed of AISI 316L, light bl

The process parameters utilized for the fabrication of the samples were optimized in previous works by the same authors on the same materials, resulting in a final density of the manufactured samples greater than 99% (confirmed by Archimedes' method) [5,191]. In addition, all samples were created utilizing Concept Laser's proprietary random island scanning approach, which uses a square island size with one side equal to 5 mm. Furthermore, between the different layers, the islands incur a fluctuation in the XY plane with an offset of 1 mm in both directions. These solutions attempt to lower the thermal stresses created during the PBF-LB process, as has been established in the literature [109,110,129,192].

All specimens produced, except for sample AM-2 (see Figure 49), were heat treated to improve the mechanical properties of the martensitic steel. In accordance with earlier research in the literature [151,147,234], a solution annealing treatment was done at a temperature of 815°C for 1 hour followed by air cooling, and then an aging treatment was performed at a temperature of 480°C for 5 hours followed by air cooling. Figure 50 displays a snapshot of the specimens produced.

Figure 49 - Image of cFGMs specimens fabricated by the PBF-LB process

2.2.2.1.2 Metallographic characterization

In order to evaluate the quality of the joint obtained in the four samples generated, the latter were submitted to metallurgical investigations, such as macro- and microstructural analyses and chemical exams. The metallographic characterisation was done on the cross sections (YZ plane) of each specimen. The specimens were constructed ad hoc to analyze the distribution of faults, such as porosity, and to describe the interface area by evaluating the likely presence of lack of fusion along the grading direction between the two materials, which could damage the joint. The specimens were viewed using an inverted optical microscope (Nikon Eclipse MA200, Nikon Corporation) and a digital camera. The investigations were carried out in image analysis tools such as ImageJ and Matlab, with ad hoc methods designed to acquire the necessary results.

Subsequently, a microstructural investigation was done on the same samples by chemical etching in order to disclose the phases present in the different zones and especially in the gradient zone. The chemical reagent employed to expose the microstructure was composed of nitric acid, hydrochloric acid, and lactic acid in a ratio of 1:2:6.

Finally, the samples were chemically analyzed to reveal the possible presence of contamination in the areas of pure materials and the progressive and continuous evolution of the chemical composition between the two materials. For this goal, a microanalysis using an energy-dispersive X-ray spectroscopy (EDS) probe was undertaken to allow a quantitative pointwise analysis of the chemical composition of the cFGMs specimens generated. The chemical examination was conducted along the YZ plane. Characterization was performed using a scanning electron microscope (SEM, ZEISS GeminiSEM 500) paired with an Oxford Instruments X-Max Extreme EDS detector.

2.2.2.1.3 Residual stress measurement set-up and procedure

The residual stresses were estimated utilizing the contour approach, which creates a two-dimensional map of residual stresses perpendicular to a cross-section with a single measurement [227]. This measurement method, as in other destructive procedures, leverages tension relaxation following material removal, causing detectable displacements. In the contour method, stress alleviation is obtained by correctly sectioning the component using wire electrical discharge machining (WEDM). The contours of the two newly created surfaces are measured using high-accuracy techniques, and after processing this data, a finite element analysis is employed to infer the stresses previously existed along the cut plane, imposing the measured displacements as boundary conditions [227,230,231]. For a more thorough description of this measurement technique, read [230].

Prior to measurements, the cFGM specimens were removed from the construction platform with a single WEDM cut and finishing cutting parameters. Detachment from the build platform might induce distortion in the component or alteration in residual stresses. Nevertheless, in [232,233] it has been shown that specimens with a thickness more than 10 mm experience dramatically reduced distortions compared to thinner specimens. In addition, it has been reported in [235,236,237] that for parallelepiped-shaped specimens residual stress relaxation subsequent to detachment is more pronounced in the longitudinal direction, while the stress component in transverse direction is minimally impacted and remains present even at high values. Furthermore, Clausen et al. in [238] claimed that for samples without internal features, residual stress variations due to build platform removal decrease monotonically with increasing distance from the cut surface, in accordance with the St. Venant's principle [239].

In this research work, transverse residual stresses were determined by cutting the specimens along the YZ plane, as represented by the dashed red lines in Figure 49. Consequently, the contour method allowed for the investigation of residual stresses along the plane with the composition gradient. At the same time, the stress component least influenced by the build platform removal was measured. The material composition gradient, in fact, influences on the degree of residual stresses on such direction. Furthermore, as previously stated, the AM-2 sample was evaluated prior to heat treatment to investigate its effect on the residual stress state of the cFGM components.

2.2.2.2 Results and discussions

2.2.2.2.1 Characterization of Interfaces through Metallurgical and Chemical Analysis

Observation of the polished samples using an optical microscope revealed the presence of discontinuities inside the manufactured volume. For each specimen, a region with a height of 3.5 mm and a width of 35 mm centered on the transition zone between the two materials was photographed and subsequently evaluated by image analysis. A binary filter (threshold) was applied to the images to maximize the contrast between the discontinuities and the material surrounding them.

Figure 51a÷d shows the studied photos after the application of the threshold and the results of the analysis. The discontinuities discovered may all be characterized as porosity or lack of fusion based on their morphology and no cracks were noticed.

Figure 50 - Appearance of the metallographic specimens after threshold application.

The porosities were analyzed according to their amount (Figure 52a) and their area (Figure 52b). Using a bin width of 5 mm for both plots, the first and last bins represent the results obtained in 18Ni Maraging 300 and AISI 316L, respectively. The remaining five center bins, on the other hand, illustrate the trend of porosity inside the mixing zone and are an indicator of its gradualness. On the left vertical axis of Figure 52a are the percentages of the number of discontinuities for each bin compared to the total number of discontinuities for each sample, which can be read from the bar graph, while on the right vertical axis are the quantities for each bin, represented by the line graph. The same type of representation has been employed in the graph in Figure 52b. All trends show that there is a gradual reduction in the number of

discontinuities and their extent as one advances from 18Ni Maraging 300 to AISI 316L. The lone exception is specimen AM-1, which exhibits a large concentration of discontinuities at the area where the process parameters change, in the midst of the mixing zone. It is also significant to notice that unlike the AM-1 specimen, the AM-4 specimen does not display any peaks in the pore distribution, even though it was generated utilizing varying process parameters.

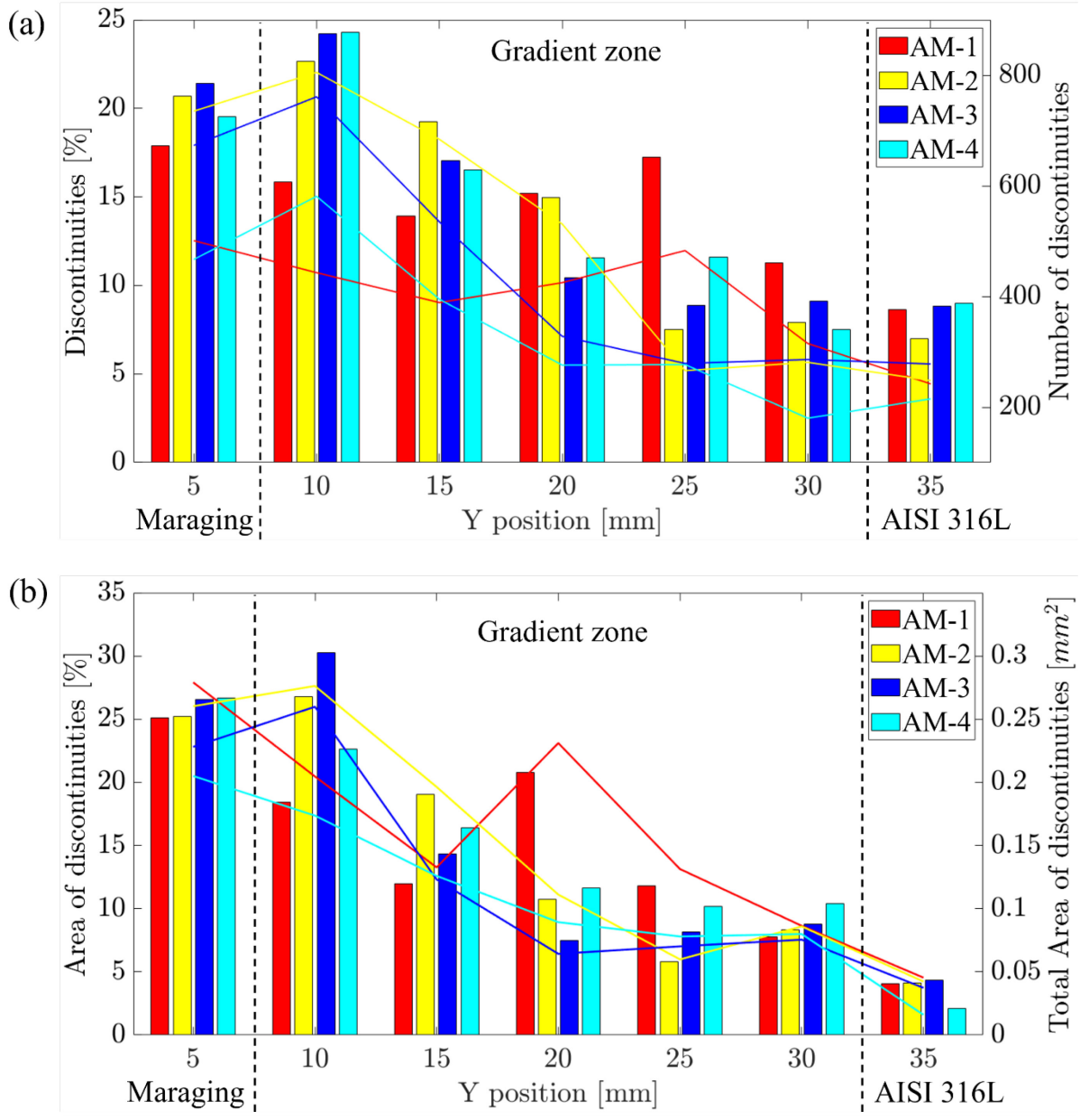

Figure 51 - trend of discontinuities (a) and their extent (b) detected in the metallographic specimens along the Y-direction with 5 mm interval. The bars indicate the percentage for each interval of the total for each specimen, the lines indicate the absolute amo

Information about the different phases can also be derived by studying the chemical concentrations of the components in the two materials involved. Figure 53 illustrates the chemical composition determined in the middle portion of samples AM-1, AM-3 and AM-4.

The analysis was conducted on the cross sections (YZ plane) of each sample. The research area is equal to 30 mm along the Y-direction and includes within it the graded interface equivalent to 25 mm between the two materials. From the findings of the chemical analysis by Energy Dispersive Spectroscopy (EDS), it is able to confirm the existence of a progressive and continuous transition of chemical characteristics between the two materials, which is very similar to the desired transition in the process of powder separation. In particular, by analyzing the evolution of the concentrations of chromium (for AISI 316L) and cobalt (for 18Ni Maraging 300), a transition can be observed from maximum values corresponding to the zones of each material (on opposite sides of the area studied) to zero values at the end, where these elements are absent.

		Y position [mm]											
		Maraging		Gradient zone								AISI 316L	
		0 ÷ 2.5		2.5 ÷ 5	5 ÷ 7.5	7.5 ÷ 10	10 ÷ 12.5	12.5 ÷ 15	15 ÷ 17.5	17.5 ÷ 20	22.5 ÷ 25	25 ÷ 27.5	27.5 ÷ 30	
Cr wt%	AM-1	0.00	0.00	0.20	2.88	3.98	9.22	13.79	15.15	15.66	16.08	17.17	17.22	17.15
	AM-3	0.00	0.43	0.88	2.34	4.59	9.03	13.20	15.03	15.75	16.15	16.72	17.11	17.15
	AM-4	0.00	0.02	0.64	2.54	4.15	9.00	12.88	14.95	15.15	16.00	17.02	17.10	17.22
Mean		0.00	0.15	0.57	2.59	4.24	9.08	13.29	15.04	15.52	16.08	16.97	17.14	17.17
Co wt%	AM-1	9.89	9.91	9.66	7.77	7.57	4.91	2.33	1.80	1.33	1.25	0.70	0.10	0.00
	AM-3	9.80	9.67	9.54	8.43	7.15	4.97	2.87	1.79	1.54	1.17	0.85	0.32	0.00
	AM-4	9.55	9.50	9.52	8.22	7.22	5.00	2.55	1.89	1.25	1.22	0.66	0.15	0.00
Mean		9.75	9.69	9.57	8.14	7.31	4.96	2.58	1.83	1.37	1.21	0.74	0.19	0.00

Figure 52 - Chemical composition analysis of the cross section of samples AM-1, AM-3 and AM-4, within the restricted area of the YZ plane

This result is crucial because it shows that the equipment developed in this work can prevent contamination in the different single material zones. Contamination is a well-known problem in the literature [49,98] that limits the fabrication of functionally graded material components at the layer level utilizing a standard PBF-LB system (with a powder platform from below) and a blade/roller powder distribution approach. In addition, as shown in Figure 53, the concentrations of these components gradually spread within the transition zone generated by the powder separation system, leading to the strengthening of the interface [224]. The results

of the EDS analysis presented in Figure 53, reveal a robust and beneficial connection between the two materials, in keeping with what has been reported in the research of Wei et al. [36] and Tan et al. [105]. Finally, it is crucial to observe that the measurement results obtained from the three separate samples overlap, showing a consistent distribution of the different phases in the individual samples prepared.

2.2.2.3 Conclusions

In this investigation, the transverse residual stress field was evaluated in cFGM specimens made of AISI 316L and 18Ni Maraging 300 by applying the contour method. These samples were generated via PBF-LB and the continual variation in composition was realized within the same build layer. Furthermore, the study examined the influence of solution annealing and aging heat treatments on residual stresses. Finally, this research evaluated the impact of altering the process parameters for each composition region, namely 18Ni Maraging 300, AISI 316L, and the continuous gradient zone between them, on the residual stress field, the discontinuities distribution and the chemical composition.

Optical microscopy demonstrated a gradual reduction in the number and breadth of discontinuities from 18Ni Maraging 300 to AISI 316L. However, specimen AM-1, separated into two processing zones and produced utilizing different scanning speeds, revealed a considerable concentration of porosity in the region where the processing parameters were modified. In contrast, specimen AM-4, which was created with differential process parameters for each of the three composition zones, did not display any concentration of discontinuities in locations where scan speeds changed.

The results of EDS examination at the contact revealed the high grade of metallurgical bonding between the two materials. Moreover, the trends in the transition region were gradual and continuous for all the different samples collected, demonstrating overlapping distributions.

Residual stress analysis, applying the contour approach, indicated that in specimen AM-2, created with a single scanning speed of 180 mm/s and without heat treatment, the residual stress field exhibited tensile stress concentrations positioned at the top and bottom surfaces. These were counterbalanced by compression at the center, and the greatest significant stress was discovered on the top surface of 18Ni Maraging 300, measured 850 MPa. Moreover, the application of heat treatment resulted in a decrease of peak residual stresses detected on the specimen's upper surface. And notably, the base material 18Ni Maraging 300 exhibited the biggest stress relaxation, resulting in an almost 50% decrease in maximum tensile stress, from 850 MPa to 450 MPa. Additionally, the use of two different scan rates in instance AM-1 resulted

in a reduction of the maximum tensile stress to 700 MPa. Furthermore, in specimen AM-4, the maximum tensile stress was further lowered to roughly 560 MPa. Notably, a decrease in residual stresses across the component was found. This was done through the application of three separate process parameters for each of the three composition zones, combined with suitable heat treatment.

2.2.3 Study on the Influence of Setup in the Fabrication of Bi-Material Components using the PBF-LB Process

The major purpose of this study is to assess the ability of a low-cost system, adaptable to PBF-LB machines presently on the market, with a coater or roller for powder bed spreading, to make components with continuously varying characteristics in each layer (cFGMs). Also, the link between specific chosen factors in the production design and the result obtained in terms of metallurgical and mechanical qualities and chemical composition was studied. Hence, this is the first systematic experimental investigation on the influence of the mutual position of the different materials within the powder chamber during the distribution of the powder bed by the coater or the roller. Analyses were done to examine if the initial position of the powders impacts the creation of the powder bed and, eventually, the qualities of the fabricated components. In addition, the influence of the shape of the auxiliary equipment, designed to allow the appropriate separation of different types of powders during machine set-up, on the mechanical and metallurgical properties of the samples produced was studied. In order to get the desired qualities of the samples, experiments were undertaken utilizing two materials - a nickel-based superalloy and a stainless steel - each with differing chemical, physical, and mechanical capabilities. According to the results of post-process characterisation acquired from metallographic, chemical, and mechanical investigations, the relative locations of the materials and the geometry of the developed equipment have a limited effect on the sample's manufactured properties.

2.2.3.1 Materials and Methods

2.2.3.1.1 Materials and Equipment

This experimental study was carried out using the same machine described in Chapter 2.1.1. The machine is equipped with a Nd:YAG laser source with a wavelength of 1064 nm. The machine uses a rubber coater as a powder dispenser, which moves from the powder chamber to the build platform. The initial material used for the study was AISI 316L austenitic steel supplied by Mimete Metalpowders (Osnago, Italy). The other alloy was a nickel-based superalloy supplied by Praxair (Danbury, CT, USA). Both powders were produced by a gas atomisation manufacturing technique and sieved to select particle sizes between 15 and 45 μm. The diameter of the sieved particles was evaluated by SEM image analysis to confirm the sieving quality (Figure 54).

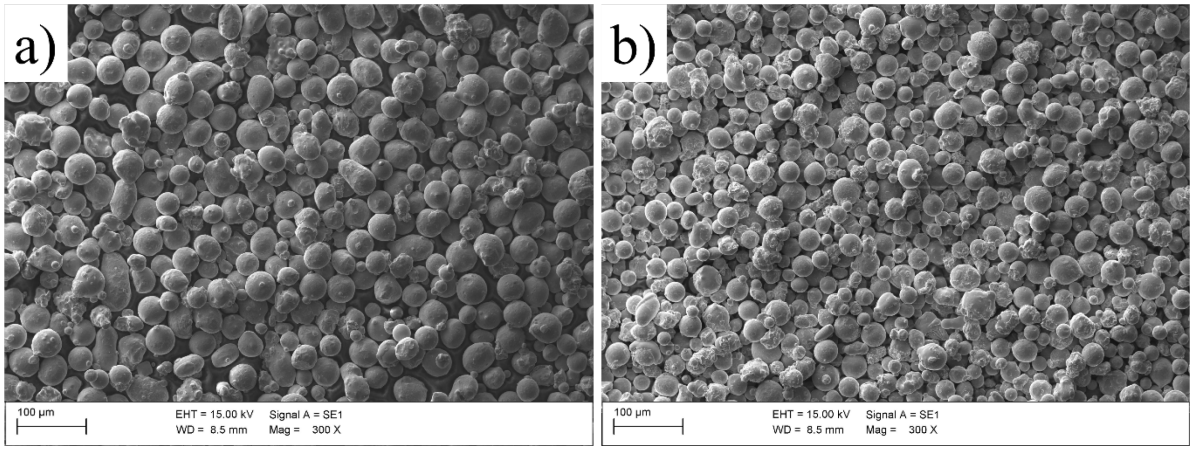

Figure 53 - SEM micrograph of the appearance of the powders used in the experiment: (a) AISI 316L steel and (b) nickel superalloy.

The chemical composition of the two powders was assessed by EDX microanalysis using a scanning electron microscope, the results of which, comparable to the nominal values given by the suppliers, are given in Table 10. The SEM study also showed that the powder particles of both materials had a well-defined spherical shape, with few anomalies such as satellites or elongated particles that could impede the proper development of the powder bed (Figure 54).

Nickel Superalloy [wt.%]					**AISI 316L [wt.%]**				
C	**Ni**	**Cr**	**Mn**	**Co**	**C**	**Ni**	**Cr**	**Mn**	**Co**
0.16	Bal	15.60	-	10.73	0.02	10.10	16.70	1.00	-
Mo	**Al**	**Ti**	**W**	**Fe**	**Mo**	**Al**	**Ti**	**W**	**Fe**
1.20	2.98	5.17	2.11	-	2.04	-	-	-	Bal.

Table 8 - Chemical compositions of the two materials' elements from EDX microanalysis.

In order to properly separate the two components during machine set-up and then to achieve their mixing in a well-defined horizontal band on the building platform, specific auxiliary equipment was designed and manufactured. This equipment essentially consists of two vertical thin walls inclined at an acceptable angle α to the direction of movement of the coater (Figure 55). The angle was chosen to create a 20mm wide mixing zone between the two materials. In this zone, the composition of the mixture moved gradually from the first material to the second, according to a theoretically linear law. This method produced a component called Continuous Functionally Graded Material (CFGM).

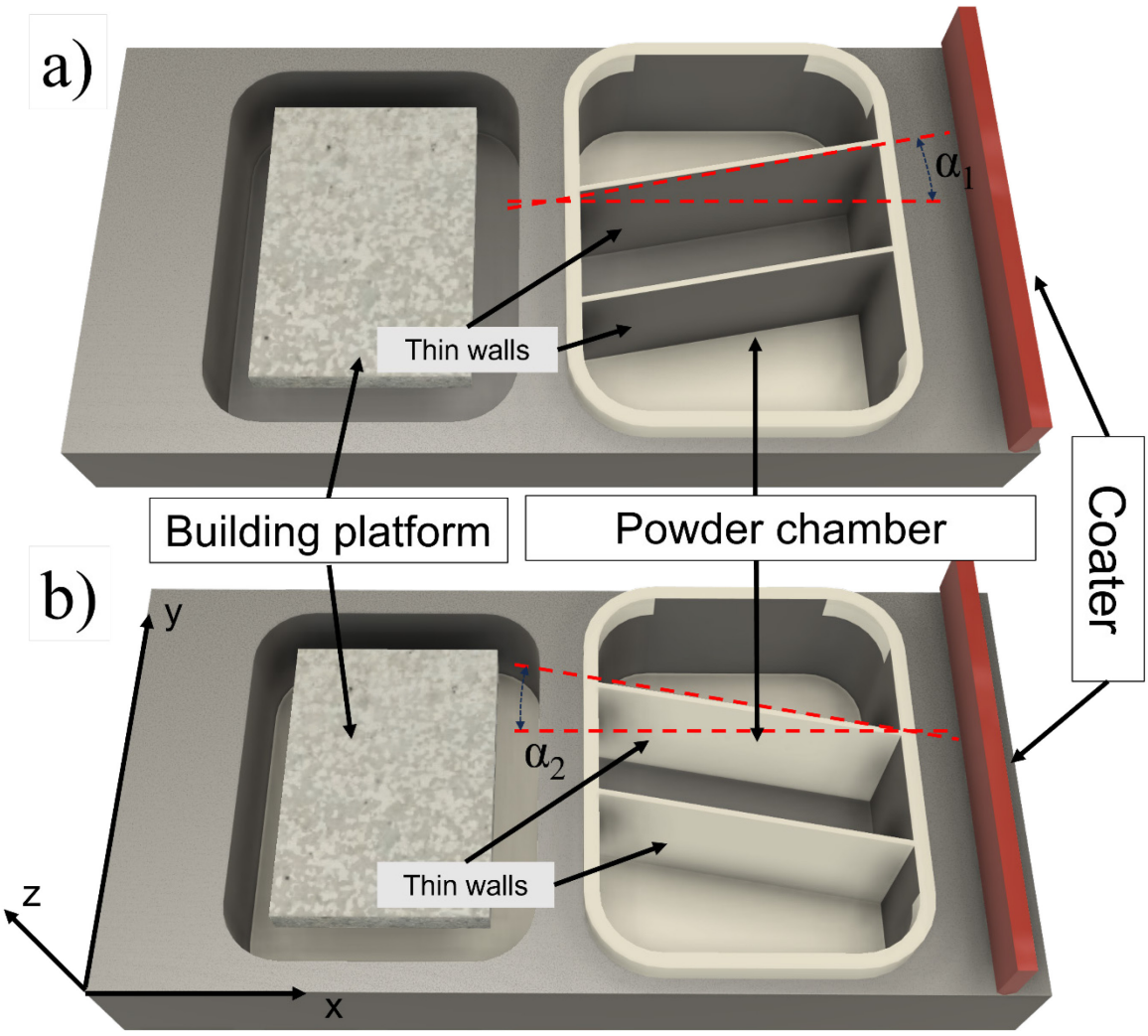

Figure 54 - Sketch of the setup used for experimentation showing the two types of dividers: (a) α1-type divider and (b) α2-type divider.

2.2.3.1.2 Experimental Plan and Process Parameters

To maximise the results of each test, two dividers were used, each with two parallel walls. Thus, two different combinations were evaluated in the same production batch. In fact, in Figure 55a, it can be observed that the walls of the divider were inclined by the angle α1 with respect to the direction of movement of the coater. This inclination determined the mixing mode between the powder outside the two walls, AISI 316L (hereafter referred to as A), and the powder between them, nickel superalloy (hereafter referred to as B). The angle α1 causes material B to be drawn over material A in the band formed by the top wall of the partition. The mixing mode of the materials is reversed in the zone of action of the lower wall of the same partition, so that here material A is pulled over material B. Figure 55b shows that the walls of the second partition are inclined in the opposite direction to the previous scenario, resulting in an opposite effect in the distribution and mixing of the materials. The experiment then involved the construction of four

types of specimens, differing in the angle of wall inclination and the order in which the components were mixed. The specimens had a total length in the plane (XY) of 30 mm, with a 5 mm zone consisting of AISI316L at one end and a 5 mm zone consisting of the nickel superalloy at the other end. The total height of the specimens along the Z axis and the length along the X axis were 10 mm. Between these two zones there was a transition zone of 20 mm in length where materials A (AISI316L) and B (nickel superalloy) gradually mixed. A schematic of the composition of the sample is shown in Figure 56.

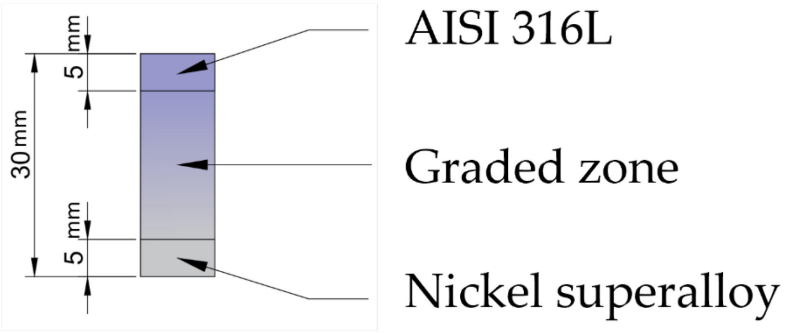

Figure 55 - Schematic representation of specimen composition.

For each type of specimen, a reproduction was made in each print to allow further research. Finally, Figure 57 shows a sketch of the specimens produced with the identification used (the sign " ' " indicates that it is the replication of the specimen with the same name).

Process parameter values optimised in previous work were used to produce all specimens [42]. Furthermore, the same set of process parameters was applied to the entire laser-scanned surface, despite the presence of two different materials. The parameters used were 100 W laser power (corresponding to the maximum power of the laser source) and 200 µm laser spot size (not modifiable on the equipment used). The layer thickness of 30 µm, the hatch spacing of 140 µm and the scan speed of 200 mm/s were chosen because it has been found that this combination of parameters allows the porosity in austenitic steel to be reduced to less than 1% [5,192]). In order to minimise the thermal stresses generated during printing, the specimens were prepared using the random square island scanning method, with each square having a side of 5 mm.

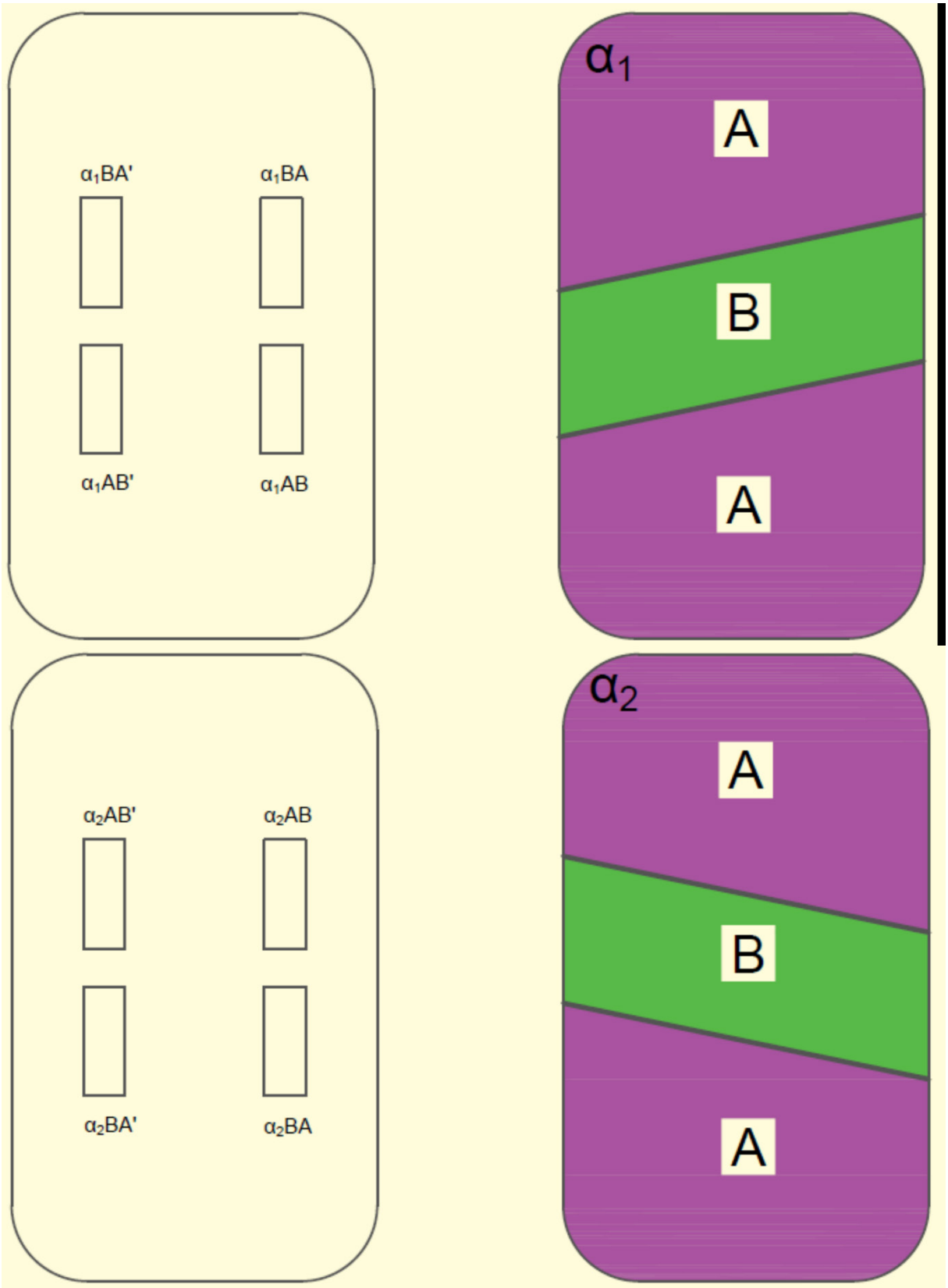

Figure 56 - Sketch of the position of the specimens during their manufacture showing the ID assigned to each of them.

2.2.3.1.3 Metallographic and Hardness Test

In order to qualitatively and quantitatively assess the quality of the samples produced and to evaluate the influence of the various combinations studied (mentioned in section 2.2.3.1.2) on the final properties of the components produced, extensive metallurgical (defect, microstructural and chemical analysis) and mechanical (microhardness tests) characterisation was carried out on all the samples produced. The metallographic examination was carried out by cutting the specimens in a metallographic cutting machine, hot mounting the sections in resin and polishing them with abrasive papers and diamond pastes. The specimens were then viewed in the polished state to allow easy estimation of porosity and to detect the likely presence of other defects such as cracks and lack of fusion. A Nikon Eclipse MA200 (Nikon Corporation, Tokyo, Japan) inverted optical microscope was used for this purpose.

The test specimens were subjected to chemical etching to highlight the microstructure and more clearly observe the result of cFGM-oriented production. Glyceregia was used as the chemical reagent. This etching solution consisted of lactic acid, hydrochloric acid and nitric acid in a ratio of 6:2:1. The analysis of the images obtained was carried out using the open source software ImageJ ver.1.54f, which allowed the extraction of quantitative information, which was then processed using Matlab R2023a.

To determine trends in the composition of the samples, chemical elemental analysis was performed using a GeminiSEM 500 scanning electron microscope (SEM) (Carl Zeiss Microscopy, New York, NY, United States) equipped with an OXFORD EDS Oxford Aztec Live with Ultim Max 100 detector (Carl Zeiss Microscopy, New York, United States).

The Vickers HV1 mechanical hardness test was performed using a Shimadzu HMV-G microhardness tester (Shimadzu, Kyoto, Japan) on the identical specimens used for metallographic examination.

2.2.3.2 Results and Discussion

2.2.3.2.1 Metallographic Examination

Metallographic studies to determine the metallurgical grade and microstructure of the specimens were carried out by sectioning in both the XY and YZ planes. With reference to Figure 57, the identification of the metallographic specimens is given in Table 11.

Samples ID	Metallographic Specimen ID	Cut Direction
α_1AB	4T	YZ plane
α_1AB′	4L	XY plane
α_1BA	3T	YZ plane
α_1BA′	3L	XY plane
α_2AB	1T	YZ plane
α_2AB′	1L	XY plane
α_2BA	2T	YZ plane
α_2BA′	2L	XY plane

Table 9 - Metallographic specimen identification.

After polishing the mounted section surfaces, they were examined and photographed using a light microscope, which revealed the presence of a central band on the specimens that extends along the Y direction (Figure 58). Figure 58 shows that in all four situations and in the respective replicates, the transition zone between the two materials was free of defects such as lack of fusion and delamination, indicating the good quality of the equipment used in this study for the manufacture of cFGM [42].

However, micrographs without chemical etching showed that the two materials behaved differently towards the PBF-LB process. The nickel superalloy, which is consistently on the left in the different photographs, was damaged by multiple cracks, which normally plague materials that are not highly resistant to rapid melting and resolidification cycles [240]. The austenitic steel, on the other hand, was free of cracks and showed only a small amount of porosity, which is considered physiological in the PBF-LB process.

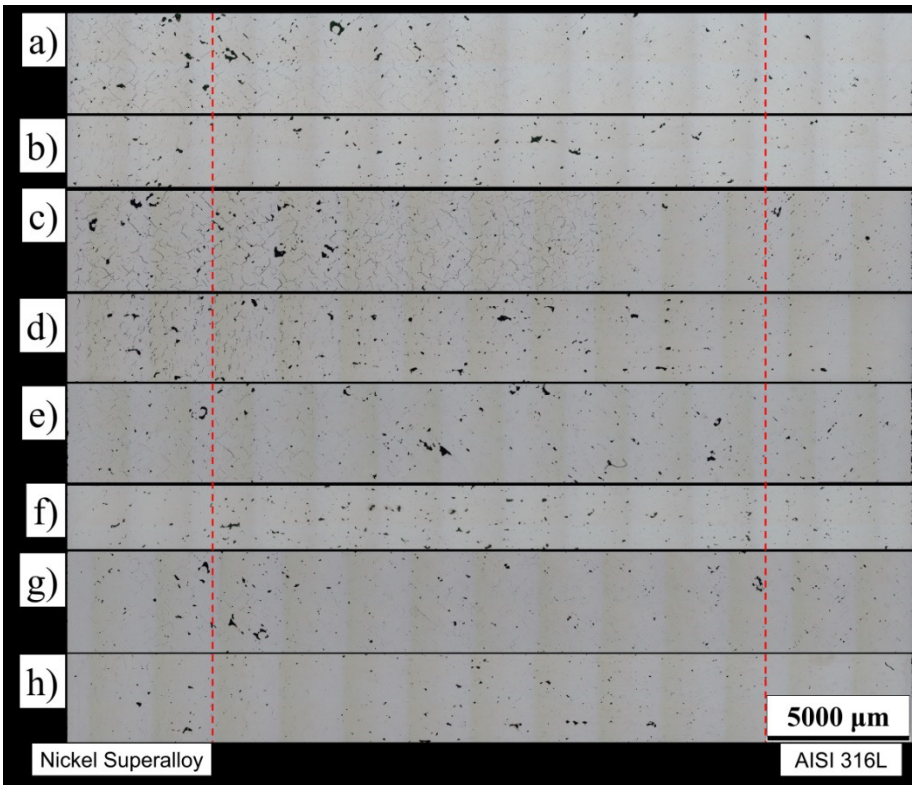

Figure 57 - (a–h): Micrographs of the polished surfaces of test specimens 1L, 1T, 2L, 2T, 3L, 3T, 4L, and 4T, respectively.

Figure 59 shows the distribution of the number of discontinuities along the XY and YZ planes. The examined sections were divided into 2 mm wide bands and in each band the identified discontinuities were counted without regard to their size. This distribution appears to follow the same trend as the proportion of nickel superalloy powder, with a high value at the left end and tending to decrease towards AISI 316L (see Figure 59a). However, this behaviour was not quite the same when the wall angle was changed. In fact, in metallographic specimens 3 and 4 (see Figure 59c), this tendency is less pronounced and the total number of discontinuities is similarly reduced compared to those in specimens 1 and 2 (see Figure 59b).

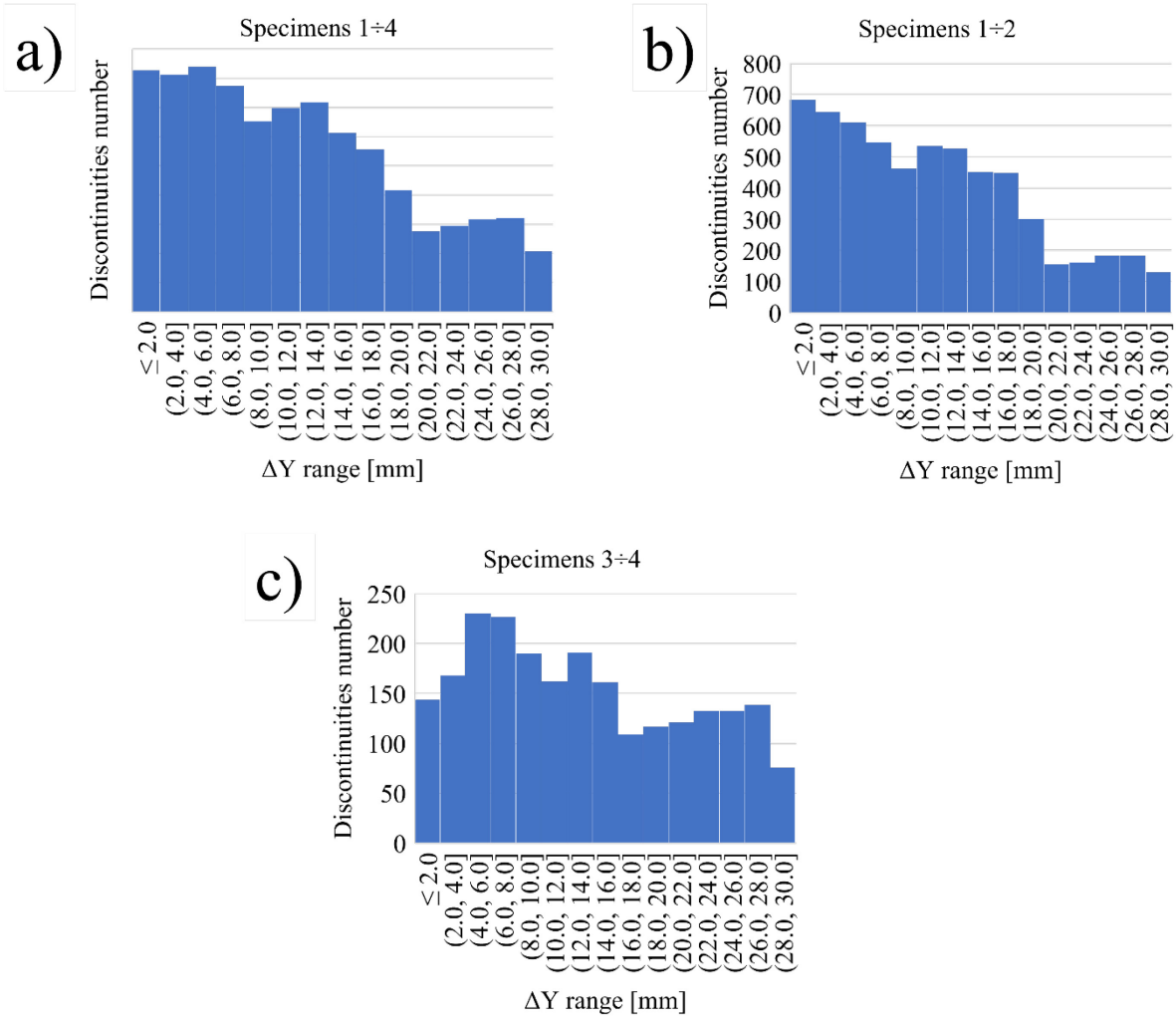

Figure 58 - Distribution of the number of discontinuities along the XY and YZ planes: (a) distribution in the eight specimens, considering the 4 combinations and (b) distribution in specimens 1 and 2 and (c) in specimens 3 and 4.

After etching, each section of the specimen made from one of the two materials showed the usual microstructures of that alloy. In fact, Figure 60a shows an austenitic structure. In addition, in the region parallel to the XY plane, the edges of the 45° laser passes are visible, in accordance with the square island approach used in production. Figure 60c, on the other hand, shows the microstructure of the nickel superalloy found in the cross section, characterised by a dendritic morphology [185]. Figure 7b shows the appearance of the microstructure within the mixed zone, where features of both materials have been detected [147].

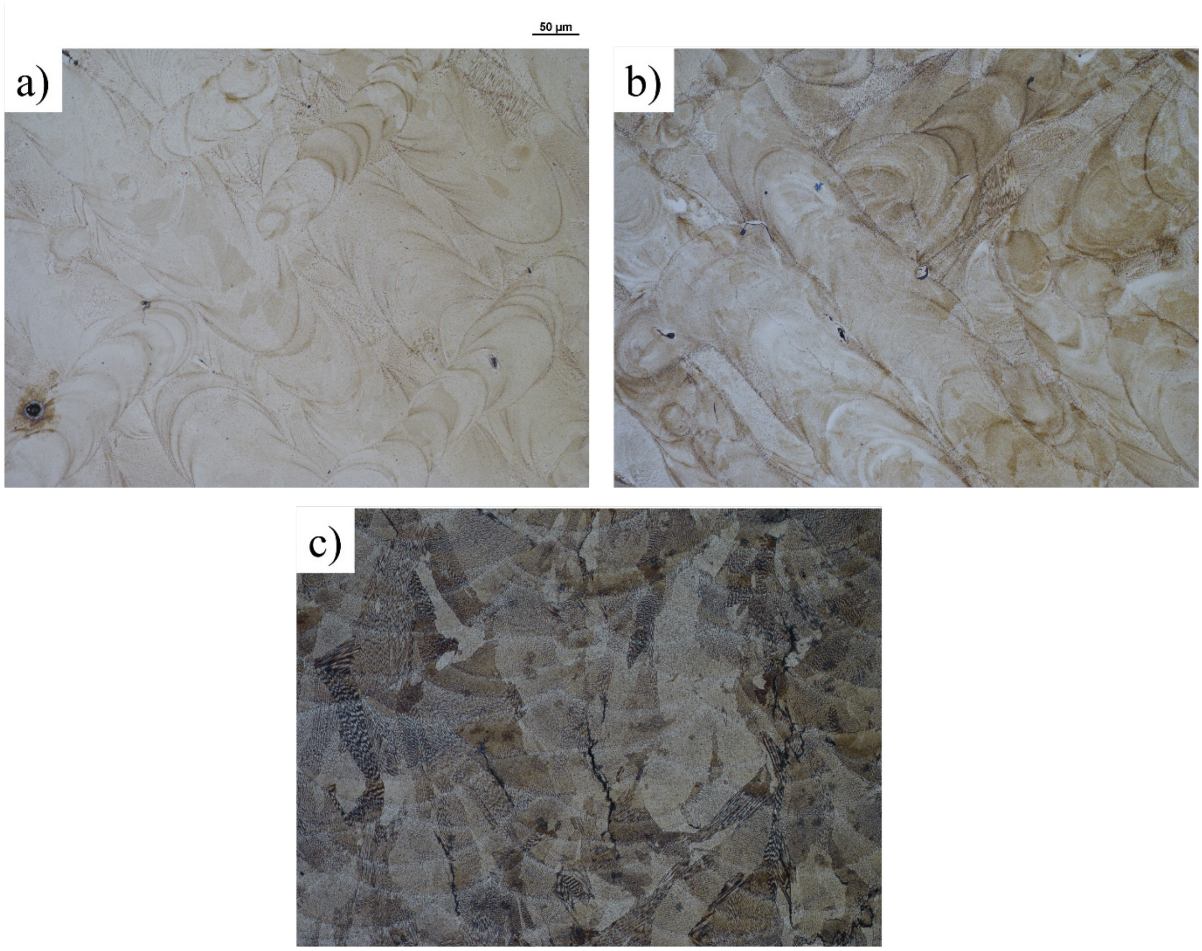

Figure 59 - Images of the microstructure of the analyzed samples: (a) 4L specimen in the AISI 316L zone; (b) 3L specimen in the mixed composition zone; and (c) 4T specimen in the nickel superalloy zone.

2.2.3.2.2 Hardness Test

The Vickers HV1 hardness test was carried out in accordance with the international standard ISO 6507-1 [241] using a load application time of 15 seconds on the surface to be tested. Each specimen listed in Table 11 was evaluated in six separate equispaced zones along the principal direction of the specimen, as shown in Figure 61.

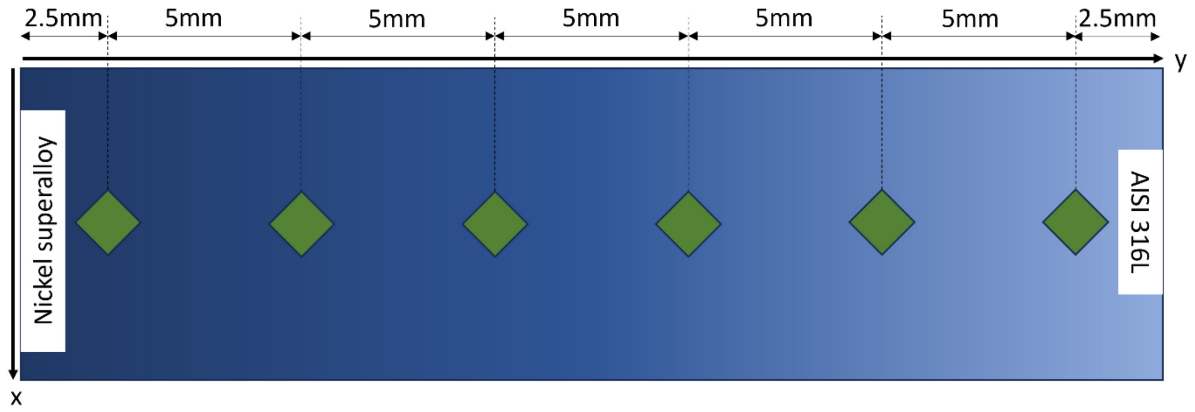

Figure 60 - Schematic diagram of hardness measurement positions on the specimen surface.

Three tests were performed at each measurement position and their mean and standard deviation were determined in order to statistically compare the data and validate the influence of different factors on hardness (see Figure 62 and Figure 63). In particular, an attempt was made to determine how the angle of the divider wall and the reciprocal position of the powders could affect the mechanical properties of the specimens. However, the comparison between the XY plane and the YZ plane sections was not carried out as the PBF-LB manufacturing process results in an anisotropic structure in the fabricated components. Therefore, it is obvious that there are also variations in the hardness values measured on perpendicular surfaces. The results showed that although in all cases there was a steady decrease in hardness towards AISI 316L, from ≈370 HV to ≈220 HV, both the angle of the divider and the relative position between the powders had an influence on the evolution of the values. The values obtained were consistent with the idea that the average hardness can be estimated as the sum of the hardness values of the different phases multiplied by their volume fractions [242].

Figure 62 illustrates the summary graphs of the hardness trends observed in the different examples studied, comparing the hardness values of the specimens produced with the different pitch angles. Comparing the graphs, it can be seen that the hardness of the AB type specimens produced with angle α1 tended to remain higher than that of the AB type specimens produced with angle α2 up to half the length tested (see Figure 62a,c). Since the higher hardness is due to the greater presence of nickel superalloy, it can be deduced that it was carried along the Y-direction to a much greater extent when the α1 angle divider was used than in the other case (as for the AB-type specimens). This difference is not observed in the case of the BA type specimens produced with both angles, because the hardness values obtained in the different circumstances were comparable (see Figure 62b,d).

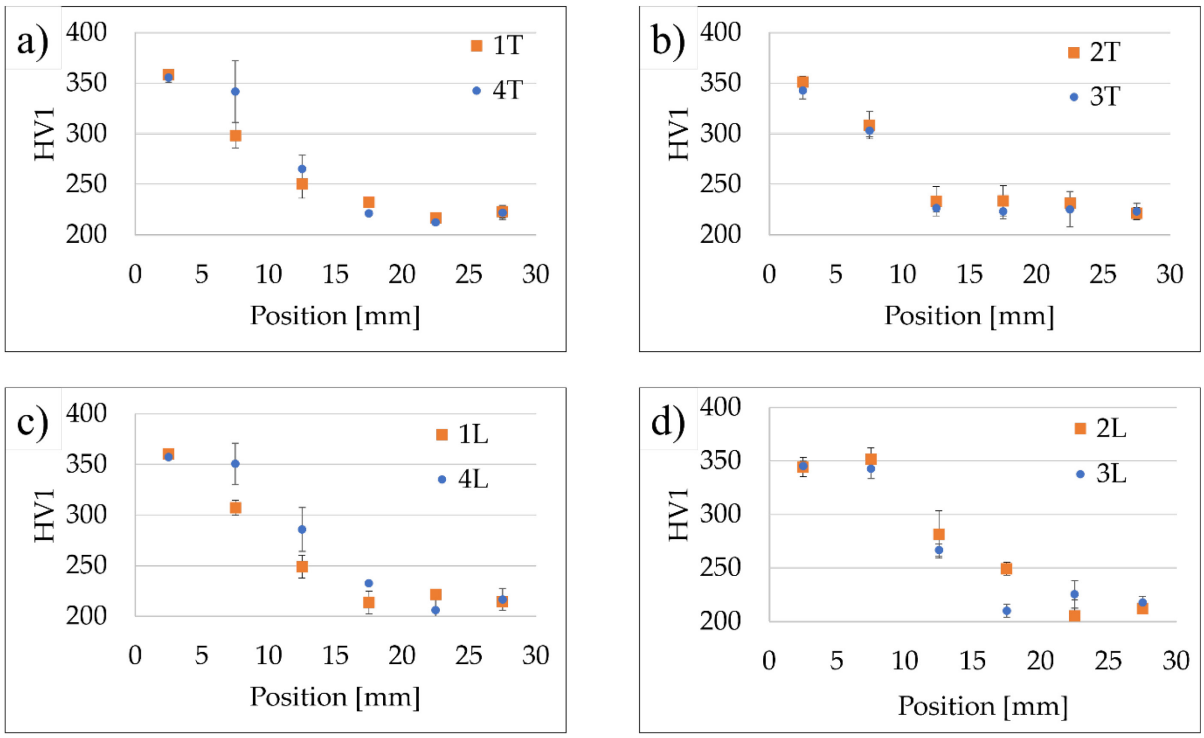

Figure 61 - Comparison of hardness values of specimens with different divider angles: (a,c) hardness results of AB-type specimens and (b,d) hardness results of BA-type specimens.

Figure 63 shows the summary graphs of the hardness trends observed in the different examples studied, comparing the hardness values of the specimens produced with different mutual positions of the materials during the dispersion of the powder bed. Comparing the graphs, it can be seen that in the case of the α2 divider (see Figure 63a,c), the BA type specimens showed a greater extent of the area affected by the nickel superalloy. This result was due to higher hardness values for approximately half of the material (a result that was more visible in the case of the XY plane sections). In the case of the α1 divider (see Figure 63b,d), the same type of behaviour is found in the AB type specimens (particularly in the specimens derived from the sections along the YZ plane). The results show that the conditions included in the experiment had a limited influence on the hardness of the specimens produced.

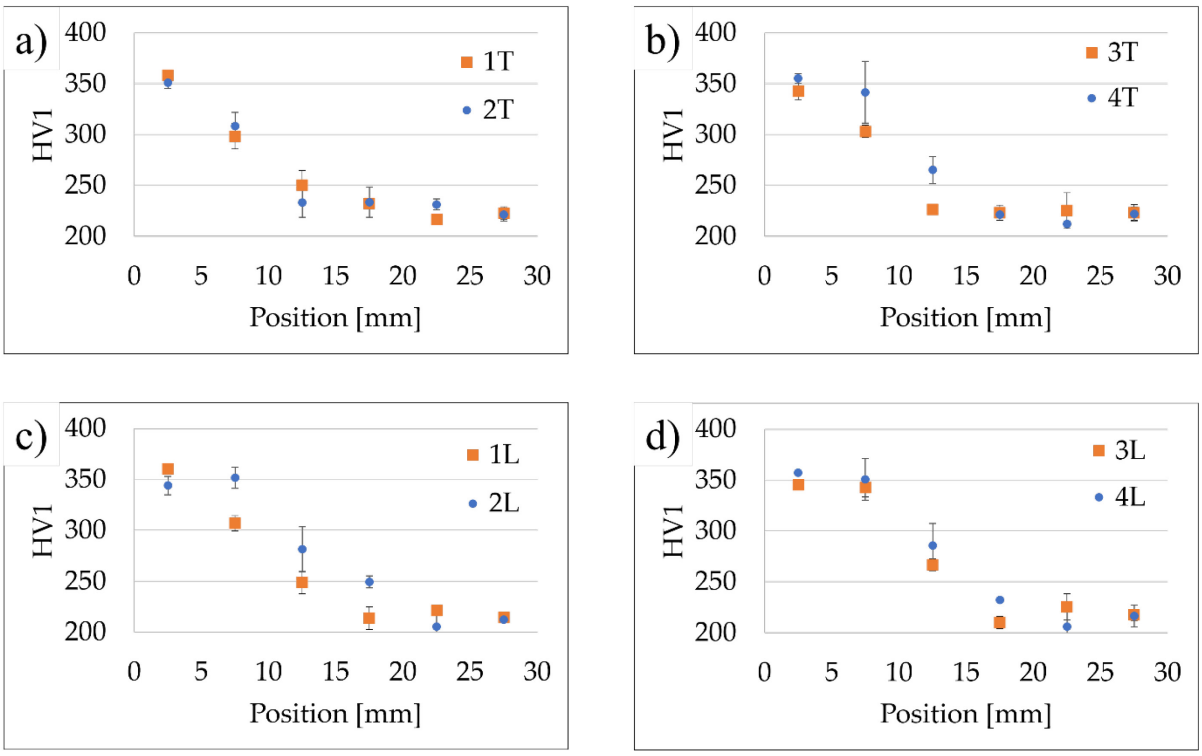

Figure 62 - Comparison of hardness values of specimens with different mutual positions of the materials during the distribution of the powder bed: (a,c) hardness results of α2 type specimens and (b,d) hardness results of α1 type specimens.

2.2.3.2.3 Chemical Analysis

Chemical analysis using a scanning electron microscope was carried out on the YZ plane of all samples at 2.5 mm intervals. The weight concentration of the chemical elements distinguishing the two materials was tested to verify that the theoretical linear variation imposed by the shape of the divider was validated by instrumental analysis. The elements present in one sample and absent in the other were analysed. Specifically, the elements Mn, Fe (present in AISI 316L and absent in the nickel superalloy), Co, Al and Ti (present in the nickel superalloy and absent in AISI 316L) were investigated. To further show the patterns of chemical concentrations, the values corresponding to the maximum measured value for each chemical element were plotted. As can be seen from the graphs in Figure 64, in all four examples tested, all the chemical elements measured showed a weight % that followed the expected trend. The first three measurement points, relating to the area where only AISI 316L steel was present, showed a flat trend precisely because this was a component of the sample not affected by the cFGM. The same result was observed for the last three points, which related to the area where only nickel superalloy was present.

These results were the same for all the samples examined. In other words, the apparatus designed made it possible to obtain components with a gradual change in chemical composition within a preset range and within a well-defined bandwidth, avoiding any form of contamination in the other areas. This is a good result compared to the results already published in the scientific literature. In reality, as indicated in the review by Wang et al [49], PBF-LB machines already on the market with a bottom-down powder chamber and a coater-based powder distribution system are severely limited for multi-material production within the same layer due to high contamination difficulties.

From the results shown in Figure 64, it can also be seen that the BA type specimens, in both α1 and α2 cases, showed a less gradual trend; in fact, as can be seen in both Figure 64b,c, which refer to the 2T and 3T specimens, respectively, there was a sudden change in the chemical concentration of the elements in the 20 mm-25 mm range (along the Y direction). On the other hand, for the AB type specimens, in both situations of α, the change in chemical concentration of the representative elements was more gradual throughout the specimen. This result showed that the relative position between the materials in cFGM production is significant at the layer level and is a parameter that can be considered, while the varied angle of the divider is negligible, at least from the point of view of chemical analysis.

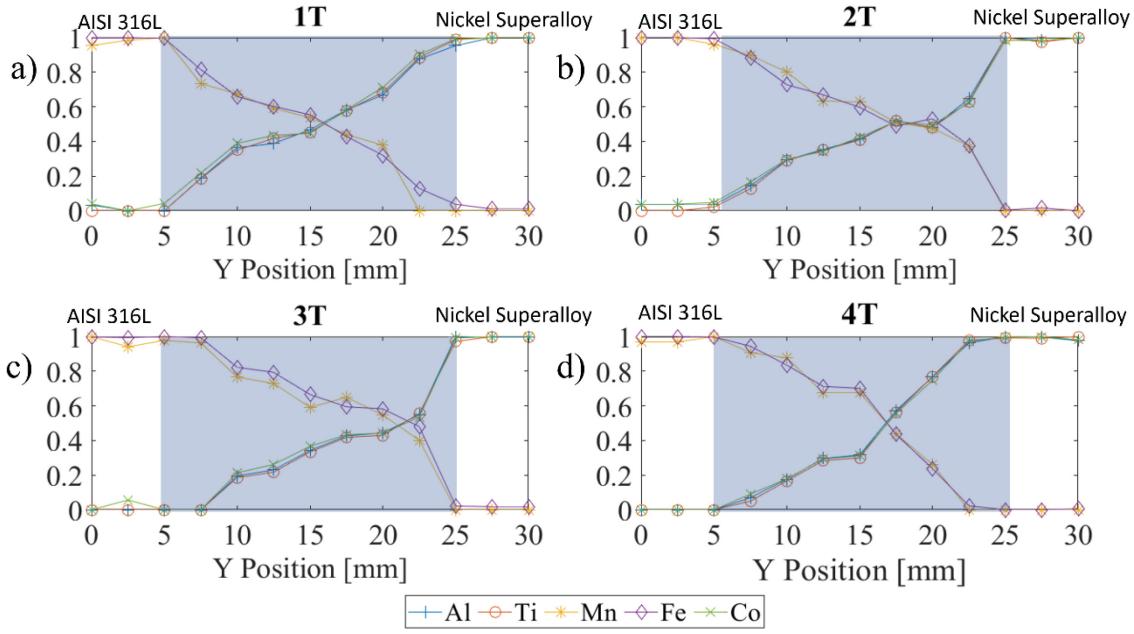

Figure 63 - Results of chemical analysis performed on sample: (a) 1T, (b) 2T, (c) 3T, and (d) 4T.

The results of the chemical analysis were compatible with the results of the hardness tests. It can be seen that in the case of the BA type specimens, a piece of the specimens approximately 20 mm long had a hardness value very close to that of AISI 316L (see Figure 62b). This finding was consistent with that seen in Figure 64b,c where approximately 20 mm of the specimen had a chemical composition extremely close to that of AISI 316L. The AB type specimens showed a steady change in both mechanical properties as determined by hardness tests (see Figure 62a) and chemical properties (see Figure 64a,d).

2.2.3.3 Conclusions

This experimental work provides a comprehensive investigation into the production of multi-material parts at the layer level using the Laser-Powder Bed Fusion technique. Specifically, this study has attempted to determine the potential of an affordable system, compatible with PBF-LB machines already on the market, to produce components with continuously varying qualities in each layer. It also investigated the relationship between some selectable parameters in the production design and the result achieved in terms of metallurgical and mechanical properties and chemical composition. The factors evaluated were the relative position of the different materials within the powder chamber and the shape of the equipment used to produce the cFGMs components. The analyses carried out and the main conclusions reached are presented below.

- The metallographic examinations have demonstrated the feasibility of producing cFGMs components at the layer level with the system presented in this work; in fact, the interface of the samples produced appeared to be free from defects such as lack of fusion and delamination, which is synonymous with the good metallurgical bond created between the materials studied in this work.

- The hardness tests showed the presence of a graded zone equal to that defined by the divider (20 mm, along the Y direction), within which there was a continuous and gradual change in mechanical properties. In addition, the hardness test results showed a limited influence of the two components studied on the final mechanical properties of the samples produced.

- The chemical analyses showed that the chemical properties of all the samples produced varied along the grading direction; however, the same analyses also revealed that the factor of the relative position between different powders had a certain influence on the final result.

According to the results of the post-process evaluation obtained through metallographic, chemical and mechanical studies, it can be said that the divider used could be configured in

several configurations without significantly altering the qualities of the samples produced. The parameters of the FGM zone depend on the type of powders used and its extent correlates with that determined during the design of the divider.

Further development of this work could include (i) the study of the tribological characteristics of the powders used and how the contact between chemically and geometrically different particles affects the powder bed coating, also using numerical simulations, and (ii) the study of the homogeneity of the FGM zone along the X-axis using materials with significantly different thermo-physical properties (density, melting temperature, etc.) and particle sizes.

Chapter 3. Multi-material AM techniques and applications in Direct Energy Deposition process

3.1 Study of the interaction between AISI 316L substrate obtained by PBF-LB process and maraging steel deposition performed by L-DED

The principal objective of this study was to create a novel 18Ni (300) maraging steel DED coating on an PBF-LB AISI 316L substrate, followed by a heat treatment, in order to provide excellent mechanical surface qualities for the finished product and lower tool and mold manufacturing costs. Numerous studies in the literature have shown how much more affordable additive technologies are when compared to traditional technologies when producing parts for high-tech industries like automotive and aerospace [243,244,245]. From an economic and sustainable standpoint, however, the convergence of many technologies to create the aforementioned components might mark a further industry revolution. Complex structures like lattices and components with conformal cooling channels are made possible by PBF-LB technology. Conversely, DED technology might be utilized to simply create functional coatings by altering the material composition to achieve the desired characteristics. Combining the PBF-LB and DED technologies seems to be a workable way to create components with both complicated geometry and strong mechanical qualities, assuming that technological advancements lead to dependable solutions.

Through the use of an optical monitoring system and real-time image processing, the work evaluated the manufactured coatings' quality in-process. Furthermore, a comprehensive microstructural and chemical metallurgical investigation of the interface between the PBF-LB component and the DED coating was performed. Finally, in order to verify the high mechanical performance of the final component surfaces, low-force Vickers hardness tests were conducted on both the as-deposited and heat-treated coatings. The outcomes demonstrated the viability of a novel, affordable, stable, and high-performing DED coating on an PBF-LB component, which could be helpful for applications on intricate geometries in the future. Additionally, the findings of this experimental investigation may be used to create effective repair methods for worn-out parts as a substitute for replacing them.

3.1.1 Materials and Methods

3.1.1.1 DED Coating and Monitoring Setup

Utilizing a DED approach, a prototype Cartesian system with a fiber laser (YLS, λ = 1070 nm and a maximum laser power of 4 kW) was used to materialize the coatings. A process fiber with a diameter of 100 µm was used to provide the beam, which was then directed through a motorized optical collimator with a focal length of 100 mm and a focusing lens with a focal length of 200 mm. A carrier gas flow (argon) transports the metal powder from the powder feeding system to a coaxial nozzle, where it is utilized in the process.

A CCD camera that was mounted in the displacement head and utilized for both positioning and in-process analysis of the melt pool's shape was also employed to monitor the process. The DED coating process design and the used monitoring system are shown in Figure 65.

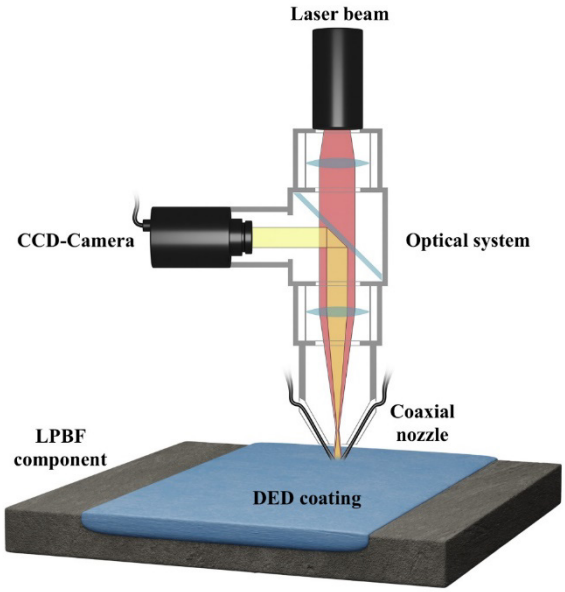

Figure 64 - Schematic overview of the Directed Energy Deposition system and monitoring setup used for coating.

3.1.1.2 Materials and Heat Treatment

As shown in Figure 66a, the coating was made of commercially available spherical powdered 18Ni (300) maraging steel. The substrates were made of AISI 316L stainless steel plates using the PBF-LB method. The AISI 316L spherical powder utilized in the production of the PBF-LB substrates is depicted in Figure 66b. Table 2 displays the size and chemical distribution of the metal powders (manufacturer-certified data) utilized for the substrate and coating. While Mimete Metal Powders manufactured and approved the AISI 316L gas atomized stainless steel powder, GE Additive Company produced and certified the 18Ni(300) gas atomized maraging steel powder. The substrates depicted in Figure 67 were produced by PBF-LB using a set of procedure parameters that had been refined in earlier studies [190,5]. In order to improve the mechanical properties, the resultant coatings underwent a subsequent two-step heat treatment based on the literature [234,33,3]: solution annealing (815°C for 1 h, air-cooled) followed by aging heat treatment (480 °C for 5 h).

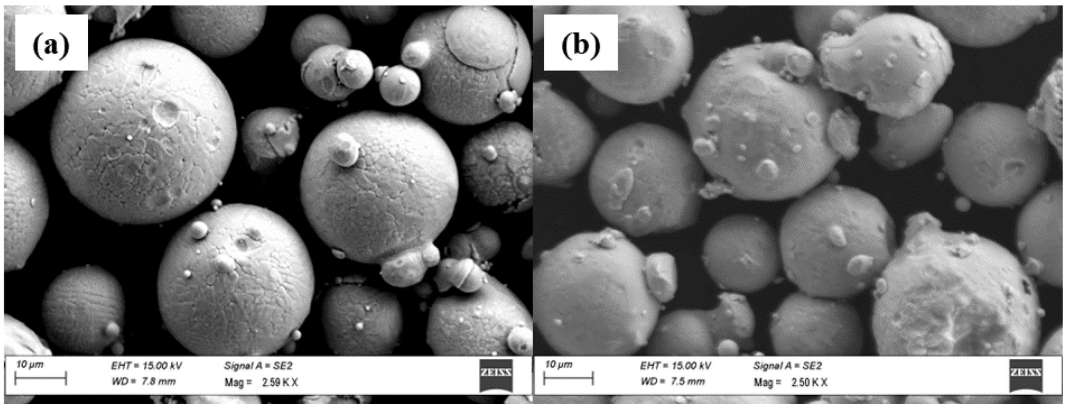

Figure 65 - Metal powder morphology displayed by Scanning Electron Microscopy: (a) 18Ni (300)—coating; (b) AISI 316L—substrate.

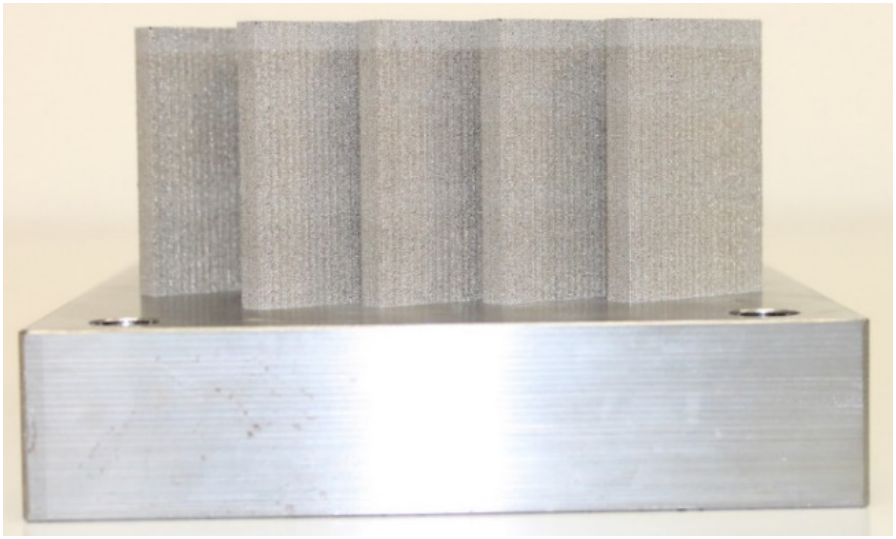

Figure 66 - AISI 316L substrates manufactured by using PBF-LB technology.

3.1.1.3 Experimental Details

As seen in Figure 68b, various numbers of layers - 1, 3, 5, and 10 - were used to create the DED coatings. These were applied using a one-way deposition technique with 30 seconds of dwell time in between each track and layer on four PBF-LB substrates (refer to Figure 68a). The terminology used for specimen identification is N_C and N_T, where N stands for number of layers, C for as-coated, and T for treated.

The following process parameters were used to deposit the coatings: hatch distance along y-direction = 0.906 mm, step height along z-direction = 0.096 mm, laser power = 400 W, spot diameter = 1.5 mm, scanning speed = 1000 mm/min, powder feed rate = 5.0 g/min, carrier gas flow rate = 10 l/min. Following initial single-track testing on PBF-LB substrates and subsequent geometrical characterization, these process parameters were determined. Table 13 lists the preliminary tests, which are based on a Taguchi orthogonal L36 experimental plan. In the work mentioned above, the methodology used to determine the ideal process parameters that produced a high-quality coating was thoroughly explained [5].

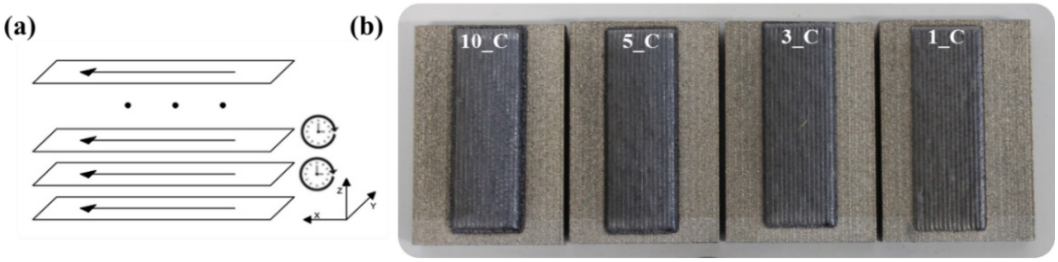

Figure 67 - (a) Schematic representation of the deposition strategy; (b) DED coatings on PBF-LB substrates.

Table 10 - Taguchi orthogonal L36 preliminary single-track experimental plan.

Process parameter	Units	Factor Levels		
		1	2	3
Laser power	W	400	600	-
Spot diameter	mm	1.5	2.0	2.5
Scanning speed	mm/min	1000	1500	2000
Powder feed rate	g/min	2.5	5.0	-
Carrier gas flow rate	l/min	10	15	-

3.1.1.4 Analysis and Characterization Procedure

Through the use of an optical monitoring system and an image analysis methodology, the manufactured coatings' quality was evaluated in-process. A CCD camera housed in the deposition head was used to watch the production process in detail. This apparatus made it possible to observe and track the shape of the melt pool coaxially with respect to the laser beam because of a dichroic mirror (see Figure 65). The camera was configured with a resolution of 1024 x 768 pixels (about 5 μm) and an acquisition frequency of 40 frames per second. An image processing method was used to extract the manufacturing process-related frames from each movie and analyze the progress of the melt pool.

Three processes make up the workflow for the image analysis methodology: frame extraction, image processing, and video capture. The latter is carried out in the MATLAB environment with the Region-Based Active Contour (R-BAC) picture segmentation algorithm.

A chemical etching (Etchant: 6 mL acetic acid, 10 mL hydrochloric acid, 1-2 g picric acid, and 100 mL ethyl alcohol) was then conducted to determine the ideal set of process parameters and to examine the coatings' final quality in terms of geometrical characteristics, microstructural attributes, and chemical composition. In addition, the coatings were meticulously prepared through cutting, embedding, and polishing steps. The Nikon Eclipse MA200 inverted optical microscope and the Zeiss Sigma 300 VP scanning electron microscope, in conjunction with EDX spectroscopy, were utilized for microstructural studies. Lastly, the HMV-G by Shimadzu

hardness tester was used to conduct low-force Vickers hardness tests on the as-coated and heat-treated coatings in accordance with the ISO 6507-1 test method (0.3 kgf of load and 10 s of residence time).

3.1.2 Results and Discussion

3.1.2.1 Optical Monitoring of the DED Process

An iterative technique that can assess an image's brightness gradient and generate regions with similar attributes is called Region-Based Active Contour. Driven by the minimization of an energy function, the algorithm begins with an initial mask in the form of a closed curve and iteratively modifies its shape and size to adjust to the brightness of the image (see Figure 69a). The efficacy of this approach has been demonstrated in the examination of the melt pool during the laser deposition process, with the aim of ascertaining its size progression and detecting possible production errors [246]. The outcome of calculating the melt pool area using the R-BAC algorithm on the 11,000 frames taken from the video that was collected during the creation of specimen 1_C is displayed in Figure 5b. When the laser is turned off, the algorithm can activate throughout the laser deposition phase and return null values during the dwelling intervals between tracks.

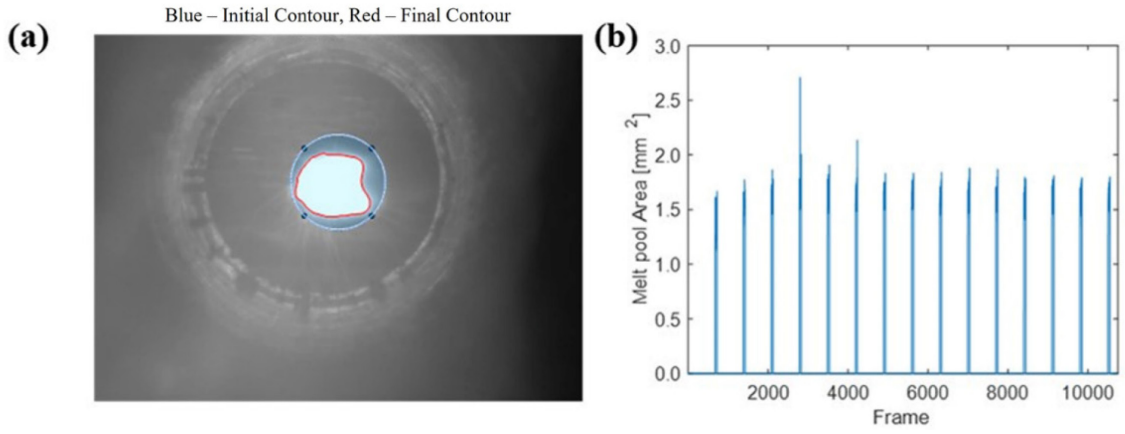

Figure 68 - (a) Initial mask (blue) and final contour (red) of R-BAC algorithm; (b) melt pool area of specimen 1_C.

The melting pool area fluctuation during layer manufacturing is depicted in Figure 70a. The plot shows that the area's average size in the first track is 1.42 mm2, but from the second track onward, when the layer consists of 15 traces, it grows and stabilizes around the value of 1.65 mm2. Furthermore, it should be mentioned that the box plot height's reduced dimension suggested the low value variability and, consequently, the coating process's good stability. The

analysis's outliers, which are frequently linked to flaws in the DED process brought on by variations in powder flow, were shown by the red crosses. An additional aspect that defined the stability of the deposition process was the distance between the outliers and the average values.

The trend that the melt pool assumed during building multilayer components 3_C, 5_C, and 10_C, respectively, is depicted in Figure 70b-d. As previously demonstrated, the average melt pool area for each layer could be reliably estimated thanks to the minimal divergence of the computed value during the deposition of single traces, which was mostly caused by the implementation of the dwelling times between each track. The 15 tracks that make up each layer's summary values revealed a relatively small range of fluctuation with the occasional outlier. This provided more evidence that the deposition process remains stable even when producing multilayer coatings.

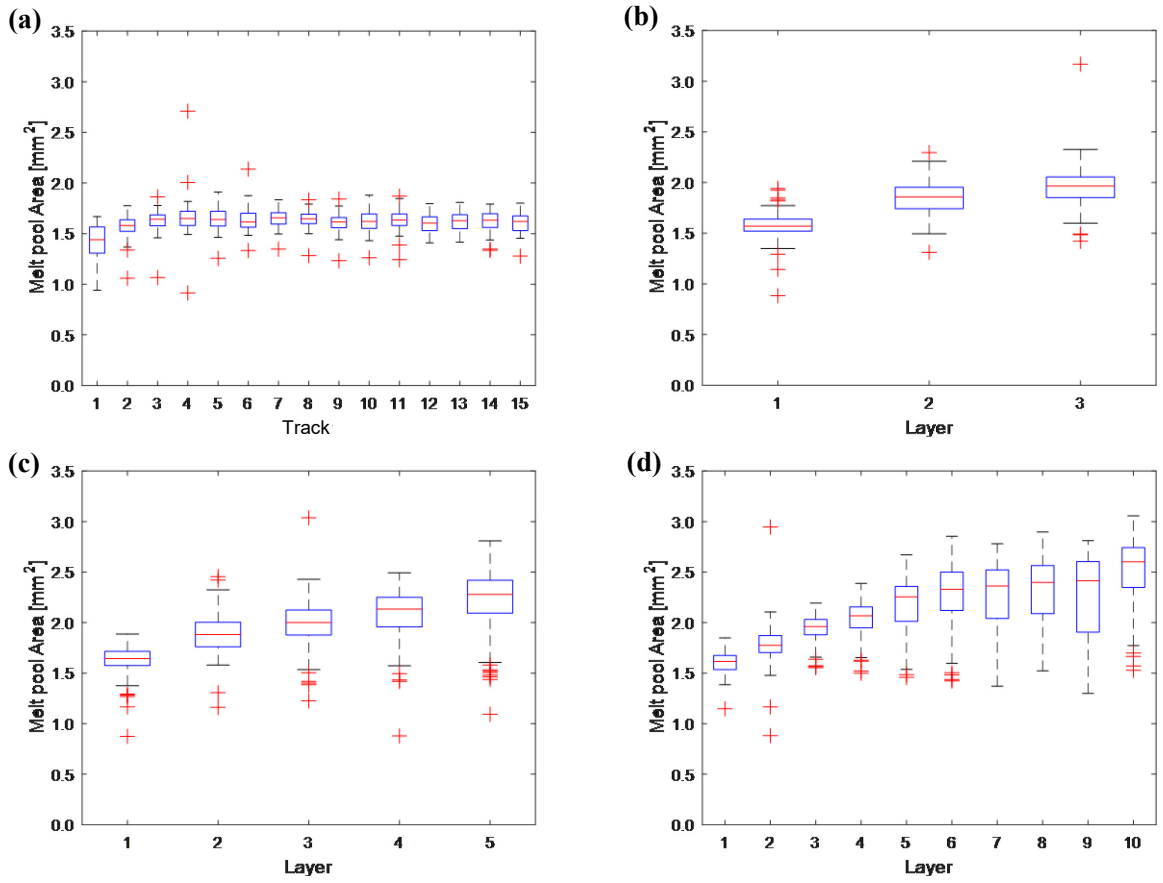

Figure 69 - Trend of the melt pool area: (a) sample 1_C; (b) sample 3_C; (c) sample 5_C; (d) sample 10_C (c).

It was simple to see from the graph analysis that the melt pool area was trending upward as the number of layers rose. A shift in the process's heat transfer conditions is responsible for this outcome [247]. In particular, the largest heat dissipation and the creation of a smaller melt pool area than the succeeding layers were achieved in the initial layer through deposition on a room temperature substrate. Moreover, the difficulties in dispersing the heat generated during laser

deposition and its accumulation in the coating area contributed to the steady expansion in the melt pool area. Despite using the same process parameters, this led to an increase in the average temperature of each layer and an increase in the area of the melt pool.

3.1.2.2 Microscopic Examination and Chemical Analysis

The SEM analysis showed that in as-coated specimens are present precipitates with moderate dimensions constituted by a Ti-rich phase (Figure 71a and Figure 71b) since the content of this element in the powder is 1.15% wt (Table 12). Differently, in the heat-treated specimens, this category of precipitates first dissolved in the metal matrix during the heating stage and then reprecipitates during the cooling stage. This segregation mechanism is characterized by more finely dispersed precipitates, most of which are not observable un-der optical microscopy. Only a small fraction of slightly coarser spherical particles is visible, as can be seen in Figure 71c and Figure 71d. The precipitation of small-size Ti-rich particles leads to an improvement of the hardness value in the heat-treated specimens [248].

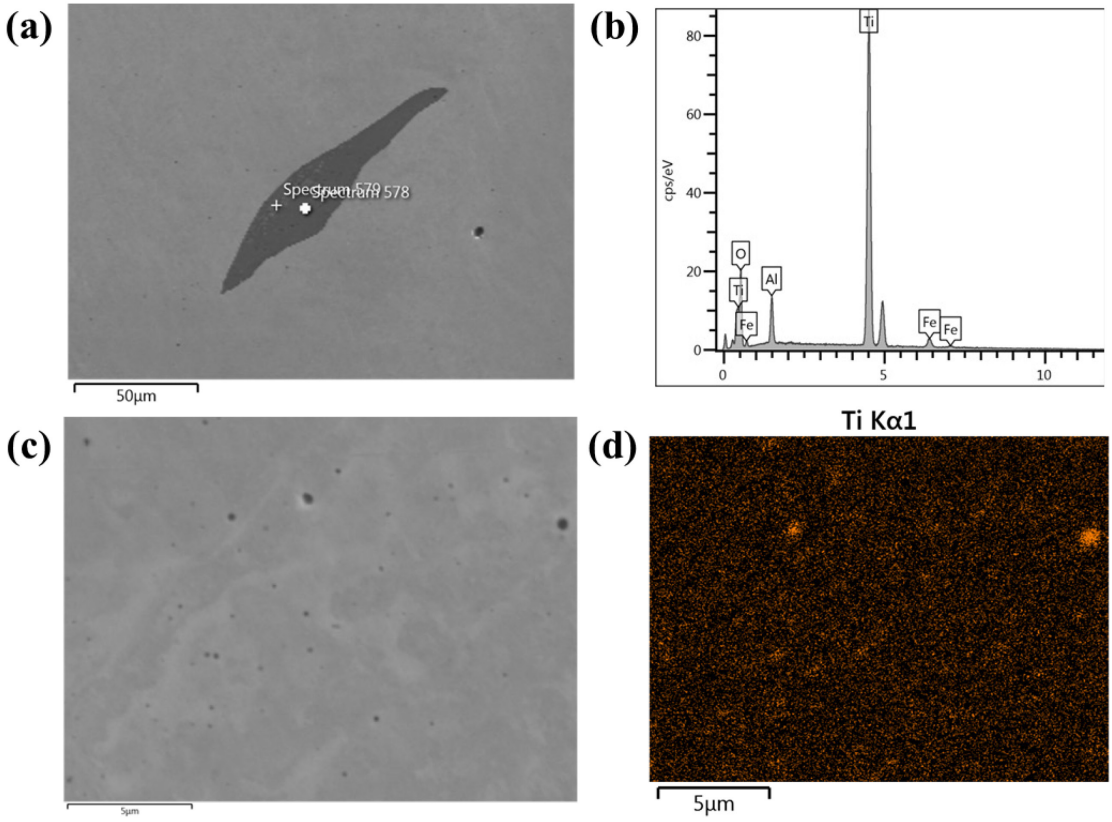

Figure 70 - SEM analysis of precipitated particles in the as-coated specimen: (a) SEM image of precipitated particles and (b) spectral distribution of chemical species. Ti particles dispersion after heat treatment: (c) SEM image of Ti particles dispersion and (d).

An EDX microprobe was used for the chemical analysis. It has been determined that the chromium has a tendency to go from the substrate, or parent metal, to the first layer (Figure 72). Marangoni convection [249] during the deposition process provides an explanation for the high concentration of chromium in the initial layer. As a result, a Cr-rich area formed in the coating's initial layer more easily due to the Marangoni convection effect and elemental diffusion at the interface between the two materials (see Figure 72b and Figure 72d). Furthermore, Figure 72c and Figure 72e show that Co likewise displays a transitory distribution between the substrate and coating. Excellent adhesion is achieved at the interface as a consequence of the preceding results. These occurrences show that age treatment has no effect on Cr and Co distributions because they were observed on specimens that had been heat-treated as well as those that had been coated.

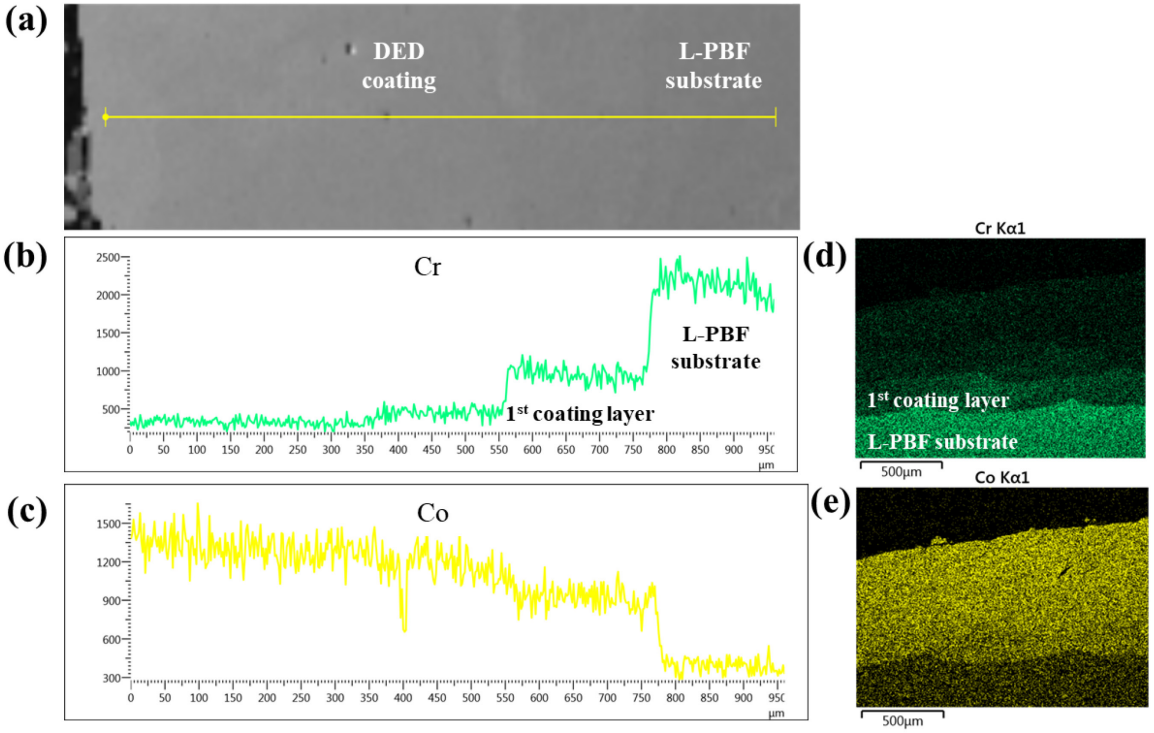

Figure 71 - Chemical composition assessed by EDX microanalysis of Cr and Co concentration in 3_T specimen: (a) SEM image of coating and substrate zone, (b) EDX line scan of Cr distribution, (c) EDX line scan of Co distribution, (d) EDX scan map of Cr distribution

Before the chemical etch, optical micrographs of the specimens showed spherical discontinuities with dimensions between 10 and 30 µm (Figure 73), which are acceptable for this kind of production procedure [250].

Figure 72 - Optical micrograph of 5_C specimen showing porosity.

Specimens were chemically etched to expose the material's microstructure. The distinction between the microstructure of the heat-treated specimens' initial layer and subsequent layers is an intriguing finding. Micrographs demonstrate how the material's treatability was adversely impacted by Cr dispersion. With the exception of the first coating layer, all coating layers displayed a distinct martensitic transformation caused by the precipitation of intermetallic compounds (Figure 74). Visible austenite regions were scarce and far between. Additionally, the metallurgical interface (see Figure 74 and Figure 75) could be seen to be regular and devoid of noticeable flaws. There were no discontinuities such as delamination, fusion and adhesion failure, fractures, or notable porosity in any of the samples. Moreover, there were no intermetallic precipitates. Moreover, Figure 75 illustrates the absence of an extended heat-affected zone (HAZ) and the presence of a fusion line at the substrate-coating interface zone. This is because the Directed Energy Deposition technique is characterized by localized heating and rapid cooling.

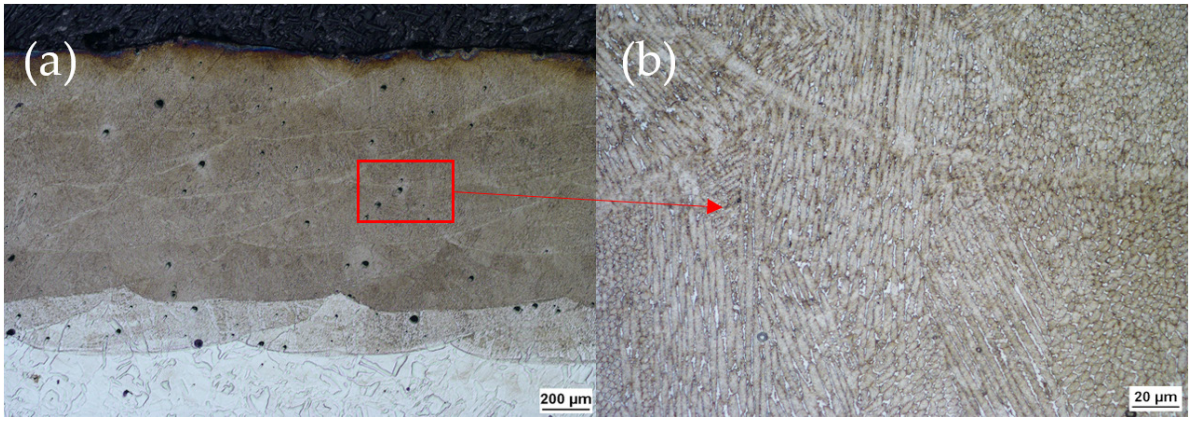

Figure 73 - 5_T specimen showing (a) different microstructures in the coating, between the first and subse-quent layers, and (b) complete martensitic microstructure in the upper layers.

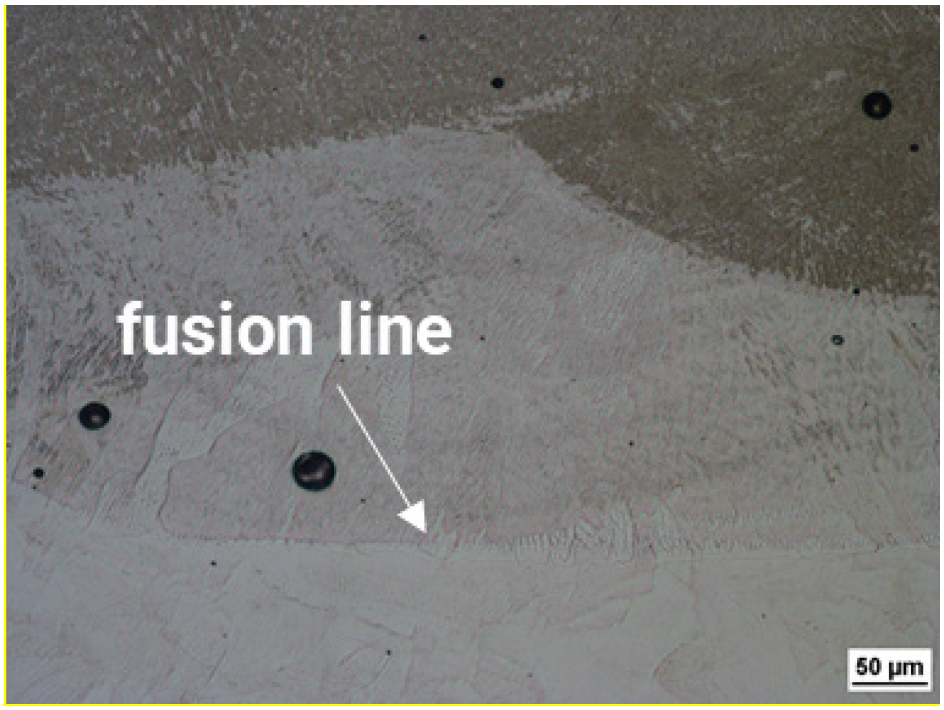

Figure 74 - Optical micrograph of the interface zone in specimen 5_T at 200X magnification.

The microstructure of the 1_T specimen is reported in Figure 76, which indicates only a partial transition, most likely as a result of the inhibitory impact of Cr. It is a well-known fact that the Cr effect on iron-based materials lowers the temperature at which martensite starts to develop (Ms), which in turn promotes the creation of austenite during the solidification process [251] and inhibits the transformation of martensite during the aging treatment step. Furthermore, because of the dissolution of Cr in the first layer, which formed Fe-Cr austenite, the aggregation of a significant amount of Cr improved the austenite stability in this location.

Figure 75 - 1_T specimen microstructure showing the incomplete martensitic transformation.

The heat treatment also had an impact on the AISI 316L substrate (Figure 77). Actually, the laser traces of the PBF-LB process were clearly visible in the as-coated state, but they vanished in the heat-treated substrate due to recrystallization that took place during the heat treatment.

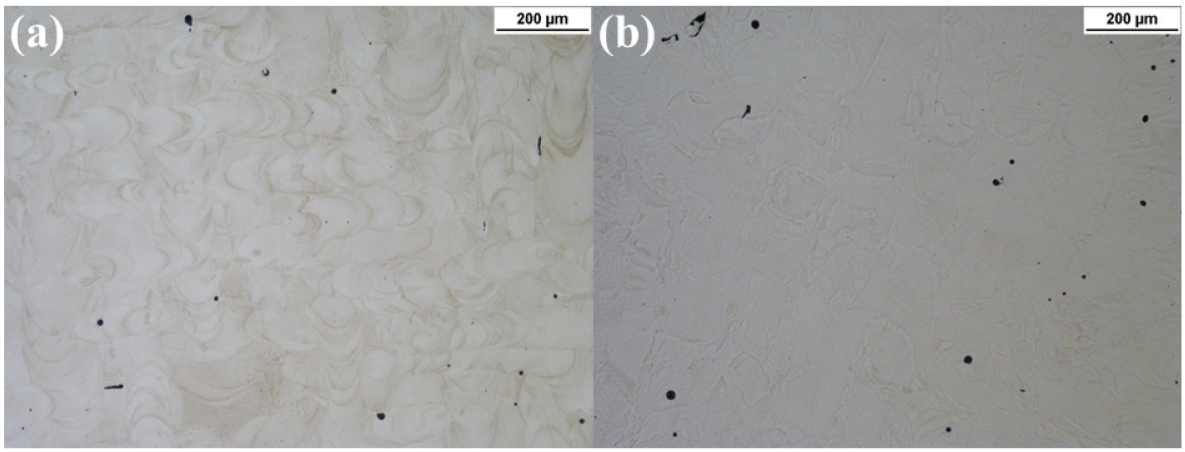

Figure 76 - Substrate microstructure in (a) as-coated condition and (b) heat-treated condition.

3.1.2.3 Low-Force Vickers Hardness Test

An assessment of the impact of aging heat treatment on the Maraging coating was conducted using the Vickers hardness test. Every sample was examined in the direction of coating growth. The hardness trend appears to be superimposable throughout the various samples, as seen in Figure 78. The as-coated sample hardness in all case studies was really in the 350–390 HV range, which was in line with the 18Ni (300) maraging steel's solution-annealed state [252]. With the exception of the initial layer, all deposited layers showed increased hardness values in the samples that underwent age treatment. Actually, because of the treated coating's martensitic microstructure, the hardness difference was about 200 HV. Moreover, from an average value of 235 HV in the PBF-LB component, the hardness drops to 200 HV at the substrate-coating contact and at the first layer. As a result, it is not advisable to apply a single layer of coating (see Figure 78a).

The initial layer of every coating exhibited distinct mechanical properties, as discovered by the microscopic analysis. This characteristic can be attributed to the distinct chemical compositions produced by the combination of maraging steel and substrate metal.

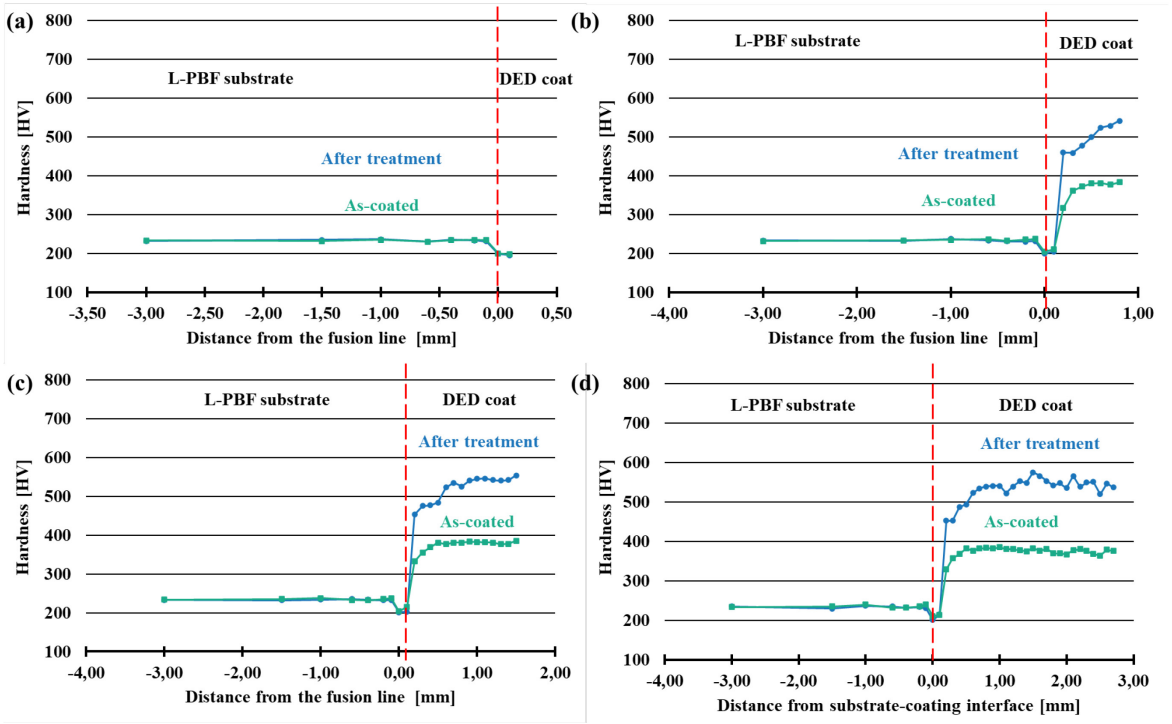

Figure 77 - Hardness trends in as-coated and after treatment samples: (a) 1-layer; (b) 3-layer; (c) 5-layer; (d) 10-layer.

3.1.3 Conclusions

This work involved the effective application of a Directed Energy Deposition (DED) coating on AISI 316L components produced through Laser-Powder Bed Fusion (PBF-LB) utilizing 18 Ni(300) maraging steel powder and subsequent heat treatment. The primary findings are listed below.

The support of an optical monitoring methodology (CCD camera + real-time image processing) enabled for the real-time observation of the melt pool, thereby verifying the stability of the coating process.

From an average value of 235 HV in the PBF-LB component, the hardness fell to 200 HV at the substrate-coating contact and the first layer. The scientific literature states that coatings consisting of 3, 5, and 10 layers have a hardness of 375 HV when they are first coated and 580 HV after treatment.

There is a considerable correlation between the hardness results and the microstructural qualities that the as-coated and after-treatment coatings obtain. Specifically, lath martensite is the microstructure that results from solution annealing combined with age-hardening treatment. Aging is caused by the precipitation of intermetallic compounds rich in nickel inside the lath martensitic structure, which strengthens the hardness through precipitation.

The work's outcomes determined if it would be feasible to create a composite with an AISI 316L core—obtained through the PBF-LB process—coated with 18Ni (300) maraging tool steel using the DED technique. In fact, it was discovered that the coatings developed in the 3-layer, 5-layer, and 10-layer cases were extremely performant due to their little porosity and flawless metallurgical interface, which was free of discontinuities like delamination, cracks, and lack of fusion and adhesion. Ultimately, by utilizing the advantages of the two AM methods used, this study seeks to lower the cost of tool and die manufacture while maintaining good surface mechanical qualities for the finished product.

3.2 WCCoCr-Colmonoy Composites deposition as method to Enhance Coatings Mechanical Performance

This work offers new perspectives and important advancements toward the development of sophisticated WC-Nickel alloy laser-deposited MMC coatings. This study's specific goals are to address the important problems with MMC coating fabrication that have been documented in the literature and to assess how the coating's mechanical properties change as the degree of reinforcement increases. In order to guard against any deterioration of the final qualities of the MMC coating, a thorough analysis of process parameters was carried out in this study to stop the dissolving of ceramic reinforcing particles. Furthermore, two distinct amounts of reinforcement (10% and 40% by weight) were examined within the matrix to illustrate the improvements in the coating's final mechanical characteristics. Without any metallurgical flaws, an MMC coating with 40% WC-Co-Cr reinforcement was accomplished effectively. Furthermore, by preventing the reinforcement from dissolving within the matrix, fractures and insufficient adhesion between the matrix and reinforcement may be avoided, potentially causing embrittlement of the finished coating. This study is scientifically novel since it shows that a high reinforcement level (40 WC-Co-Cr) may be successfully included without causing metallurgical flaws. This level is much higher than the standard range employed in literature. This development highlights the possibility of optimizing DED-LB process parameters to get better mechanical characteristics.

3.2.1 Experimental procedures and materials

3.2.1.1 Experimental setup and plan for DED-LB MMC coatings

A 3kW CO2 laser system from the TRUMPF TLF series was installed in a TRUMPF LASERCELL (TLC 1005) Directed Energy Deposition-Laser Beam (DED-LB) apparatus, which was used for the tests. The TLC 1005 functions as a cartesian machine with six axes. In order to concentrate powders on the deposition plane, a multi-jet nozzle was positioned at the laser head's output, featuring three powder gas jets that are circumferentially spaced 120° apart. The GTV PF 2/2 external powder supply system, which employs gas (helium or argon) to move powders to the nozzle, is fitted with the DED-LB machine. To obtain excellent processing results and avoid oxide formation, argon was employed as the shielding gas in this work at a flow rate of 11 l/min, while helium was used as the carrier gas at a flow rate of 5 l/min. The diameter of the laser spot was 2 mm. The schematic diagram for the DED-LB experimental setup for MMC coating deposition is displayed in Figure 79.

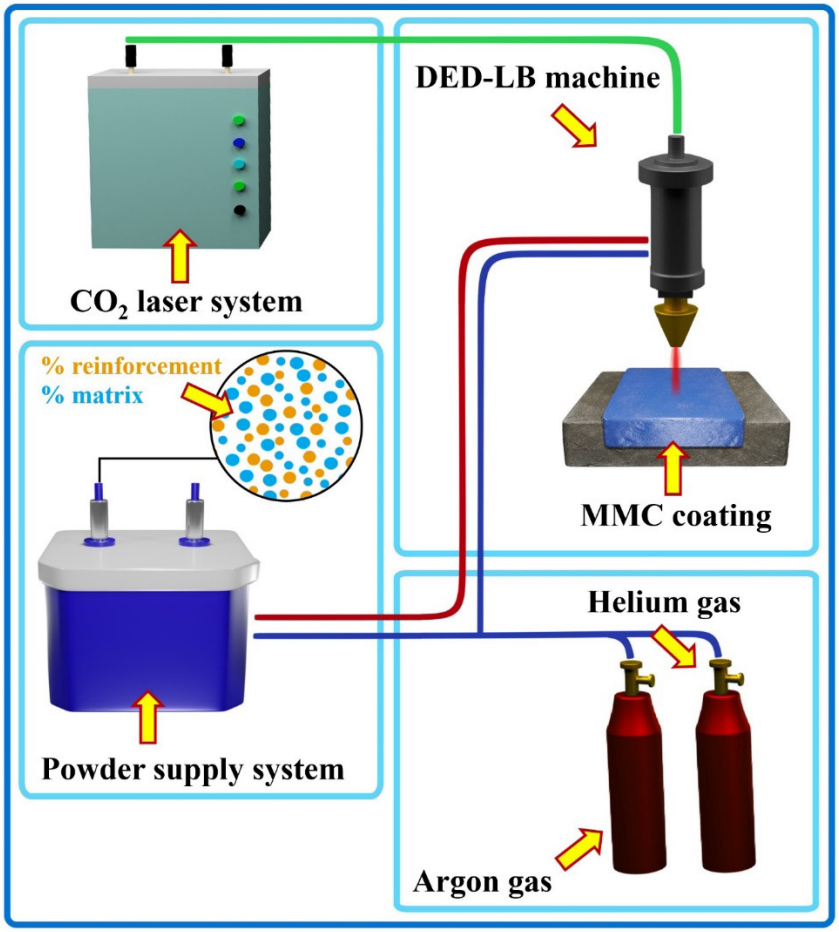

Figure 78 - Schematic diagram of the DED-LB process and experimental setup for MMC coatings

Through a series of single-track depositions along a U-shaped trajectory, a thorough analysis of process parameters was conducted in terms of experimental design. In order to create integrated coatings with excellent mechanical properties, the primary goal was to investigate the deposition process parameters that allow the prevention of ceramic reinforcement particle dissolution during the creation of metal matrix composites (MMCs). In order to rapidly identify the ideal process parameters, a Taguchi experimental plan was employed, which drastically minimizes the number of tests needed in comparison to a full factorial approach. To make the experimental design easier, an orthogonal L9 array was chosen after taking into account three process parameters and their corresponding levels. Nonetheless, the design was carried out again with two distinct reinforcement ratios (10% and 40%). Based on earlier studies done on the same materials, which provided as a starting point, three distinct values of each process parameter were chosen for each combination of percentages of reinforcement and matrix [96].

Table 11 - Combination of process parameters investigated for single-track deposition using Taguchi method.

Single-track	Laser Power, P (W)	Translation Speed, TS (mm/min)	Powder Feed Rate, PFR (g/min)	Reinforcement content, (%)
1	2400	620	14	10
2	2400	720	12	10
3	2400	820	10	10
4	2200	620	12	10
5	2200	720	10	10
6	2200	820	14	10
7	2000	620	10	10
8	2000	720	14	10
9	2000	820	12	10
10	2400	370	10	40
11	2400	470	8	40
12	2400	570	6	40
13	2000	370	8	40
14	2000	470	6	40
15	2000	570	10	40
16	1600	370	6	40
17	1600	470	10	40
18	1600	570	8	40

As shown in Table 15, three sets were found for every reinforcement-matrix combination to produce the final MMC coatings after the proper process parameters were established. These parameter sets were meticulously chosen to prevent melting, dissolution of the reinforcement particles, and any metallurgical flaws in the coating, all while ensuring the best possible adhesion between the reinforcement and matrix. A unidirectional deposition approach was used to deposit the coatings in three layers, with around 30% of the tracks overlapping. As one layer was applied after another, a 90° track rotation was used to increase the coatings' mechanical integrity and homogeneity.

Table 12 - Set of process parameters employed for MMC coatings.

MMC coating	Laser Power, P (W)	Translation Speed, TS (mm/min)	Powder Feed Rate, PFR (g/min)	Reinforcement content (%)
1C	2200	820	14	10
2C	2000	620	10	10
3C	2000	820	12	10
4C	2400	570	6	40
5C	1600	470	10	40
6C	1600	570	8	40

3.2.1.2 Materials

Using the DED-LB method, MMC coatings were created from a powder mixture that contained a WC-Co-Cr alloy for reinforcement and a nickel-based alloy for the matrix. For this reason, the adaptable nickel-based alloy Colmonoy 227-F was chosen because of its superior mechanical, thermal, and strength characteristics. It is frequently utilized in industrial settings that are prone to wear and corrosion, such as coating deposition, welding, and component maintenance. The powdered Colmonoy 227-F was made by gas atomization and included spherical particles ranging in size from 45 to 106 μm [253]. As a reinforcing material, WC-Co-Cr alloy powder, which is also generated using gas atomization and comprises spherical particles ranging in size from 15 to 45 μm, was employed. This alloy is frequently utilized to produce strong, long-lasting coatings for a range of industrial uses. These include the manufacturing of machine parts that are subjected to severe wear and abrasion, cutting tools, and mining and energy components. The literature states that an MMC coating with WC as the hard coating particles and nickel as the matrix offers excellent toughness (Ni), amazing thermal stability, effective wear resistance, and acceptable wettability of nickel on the WC surface [154]. For the DED-LB MMC coatings testing, a few hot-rolled bulk material substrates made of AISI 316L with dimensions of 50 x 50 x 6 mm were utilized. Table 16 displays the materials' (powders and substrate) chemical composition as approved by the manufacturers. The powder morphology of both materials is shown in Figure 80.

Table 13 - Chemical composition of metal matrix composite constituents and substrate (weight %).

Powder	B	C	Co	Cr	Ni	Si	WC
Colmonoy 227-F	0.80	0.03	-	0.30	Bal.	2.51	-
WC-Co-Cr	-	-	10	4	-	-	86
Substrate	**Cr**	**Ni**	**C**	**Mn**	**Si**	**Fe**	**Mo**
AISI 316L	16.70	10.01	0.02	1.00	0.48	Bal.	2.04

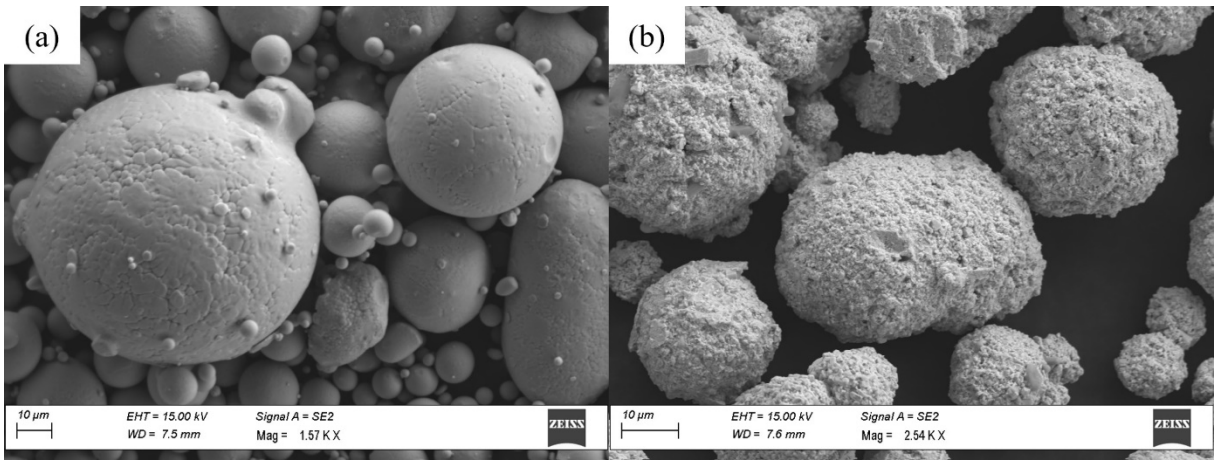

Figure 79 - SEM micrographs of MMC powders: (a) Colmonoy 227-F (matrix) and (b) WC-Co-Cr (reinforcement).

3.2.1.3 Characterization of microstructure, mechanical test, and compositional analysis of MMC coatings

The primary goal of the investigations performed on the fabricated specimens was to confirm the experimental study's premise. In actuality, it was thought to be essential to prevent the dissolving of the ceramic reinforcing particles. By cross-sectioning the deposits, metallographic specimens were prepared in accordance with ASTM E3-11 (2017) standard in order to gather this information. The samples were then heated to embed them in thermosetting epoxy resin, and the surfaces were polished using 240, 600, 1200, and 2500 grit abrasive papers in that order. In order to attain a surface finish that resembled a mirror, polishing cloths with diamond suspensions of 9 µm, 6 µm, and 1 µm were utilized initially, succeeded by an aqueous silica suspension of 0.05 µm. Nikon Corporation, Tokyo, Japan provided an inverted optical microscope, the Nikon Eclipse MA200, with which the specimens were examined at various magnifications. The digital camera on the microscope made it possible to take the pictures that were required for further examination. The porosity %, carbide phase fraction, and geometric size of depositions were among the quantitative data that could be retrieved by analyzing the photos using the free and open-source software FIJI. Following the completion of a chemical

etching on each specimen's cross-section in accordance with EN ISO 4499-(1÷3) standards, the microstructure was identified and the impact of the process parameters assessed. The reagent employed was a 6:2:1 mixture of lactic acid, nitric acid, and hydrofluoric acid to highlight the various phases.

Additionally, the deposits were mechanically examined using an HMV-G Shimadzu hardness tester (Kyoto, Japan) and a low-force Vickers hardness test in accordance with the UNI EN ISO 6507-1:2023 International Standard. The mechanical characteristics of the various phases might be measured independently using an indenter in the shape of a pyramid. Then, a mechanical test of the same kind was carried out using the Brinell scale in accordance with UNI EN ISO 6506-1:2014, a load of 187.5 kg, and a ball with a diameter of 2.5 mm. Verifying the mechanical reaction of the entire composite material created was the goal in this second instance.

In compliance with ASME Code BPVC.IX-2023 (QW-160), two specimens for each deposit composition were created and tested in order to evaluate the degree of bending strength and the adherence of the deposit to the substrate. In order to conduct the Guided-Bend Roller Jig testing, the jig was first pressed up against the deposit and then bent along the inside of the bend. A Universal Load Tester, model number 3369, is the apparatus utilized.

The deposited composite composition has been investigated by means of two distinct approaches. In the first method, the distribution of the most representative chemical elements of the two powders used was ascertained using the Zeiss Sigma 300 VP scanning electron microscope (SEM) from Carl Zeiss Microscopy, New York, NY, USA, fitted with an EDX microprobe. Both considerably smaller areas near the carbide particles and areas large enough to be regarded as typical of the average chemical composition of the combination of components were subjected to measurements. The second approach, on the other hand, divided and measured the various stages shown in the micrographs produced by optical microscopy by using the techniques of image analysis. It was feasible to verify that the percentage of powders utilized was as intended in the experimental plan by performing calculations on the quantities produced. Finally, utilizing a PANalytical Empyrean X-ray diffractometer with Bragg-Brentano geometry, a large beta filter (Nickel), a PIXcel3D detector, and CuKα radiation operating at 40 kV/40 mA, the compounds present in the coating were determined by X-ray diffraction (XRD) analysis. The X-ray data were acquired with a step size of 0.026° and a scan step time of 398.0020 s, throughout the 2θ range of 25° to 70°. Using the PDF-4 database, PANalytical B.V.'s HighScore Plus program, version 3.0e, was able to identify the sample's crystalline phases.

3.2.2 Experimental results and analysis

3.2.2.1 Optimization of the main process parameters for advanced MMC coatings

First, a program of experiments was conducted to optimize the critical process variables needed to produce MMC coatings of superior quality. A set of early single-track depositions were conducted as part of the campaign, with a U-shaped trajectory. Figure 81 provides a few instances.

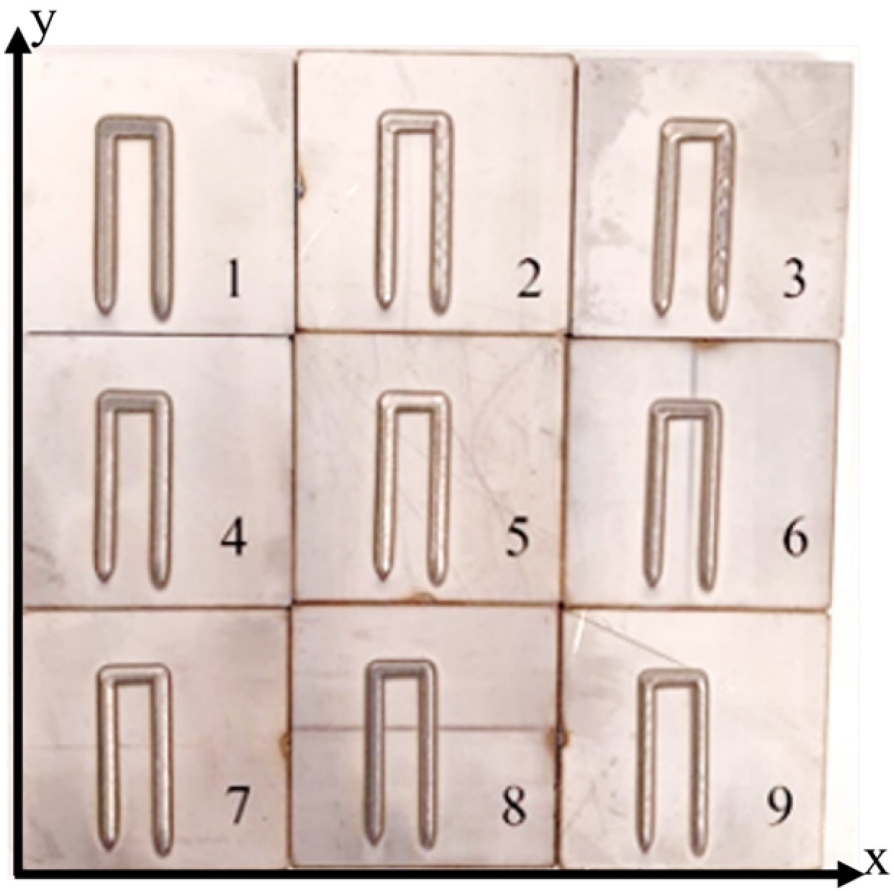

Figure 80 - Examples of single-track depositions showcasing a U-shaped trajectory, illustrating the preliminary experimental methodology employed in the study.

The primary objective was to ascertain the DED-LB process's operating parameters in order to stop ceramic reinforcing particles from dissolving in the matrix while MMC coatings were being formed. This would guarantee that the final coating's qualities are intact. According to the literature, problems such cracking, matrix embrittlement, uneven dispersion of the reinforcement phase, or insufficient adhesion between components might result from the partial or total dissolution of ceramic reinforcement within the metal matrix [158,168]. To achieve this, the best possible combination of manufacturing process factor levels was determined by

designing an experimental plan based on the Taguchi L9 approach. The proposed experimental design is detailed in Table 14.

But in addition to simply preventing the full or partial melting of the ceramic reinforcing particles, the optimal process parameters were carefully selected according to three unique geometric features that define the ideal operating range for the production of high-grade coatings. The coating-substrate dilution, aspect ratio, and wetting angle are among these properties that have been widely referenced in scientific literature [254,5]. Dilution must be kept within the specific range of 2%–10% in order to prevent excessive substrate material contamination of the coating and maintain the inherent qualities of both materials [5]. Furthermore, as this study's base material is softer than the coating material, increasing dilution may result in a decrease in coating hardness, according to empirical data [177]. A sharp wetting angle of less than 47° is essential to produce coatings with a smooth surface and low inter-track porosity [255,256]. Furthermore, when considering a 30%–50% overlap, an aspect ratio larger than 3 is required for single tracks in order to provide coatings with the least amount of undulations and inter-track porosity [255].

The average values of the geometric properties of deposited tracks, such as aspect ratio (H=w/hs), dilution (D=hi/hi+hs), track height (hs), penetration depth (hi), and width (w), are given in Table 17. As seen in Figure 81, the results in Table 17 indicate the arithmetic mean of the geometric measurements taken from each individual U-shaped track's left and right segments. Every track's average porosity % was also ascertained.

Table 14 - Averages of geometric measurements and porosity of the single deposited tracks

Single-track	Track width, w (mm)	Track height, hs (mm)	Penetration depth, hi (mm)	Dilution, D (%)	Wetting angle, α (°)	Aspect ratio, H	Porosity (%)
1	2.65	0.77	0.00	0.00	57.00	3.44	9.50
2	2.65	0.71	0.03	4.05	49.75	3.73	13.40
3	2.49	0.52	0.04	7.14	37.75	4.79	11.15
4	2.62	0.80	0.03	3.61	55.50	3.28	16.85
5	2.57	0.64	0.04	5.88	42.00	4.02	17.40
6	2.49	0.57	0.02	3.39	42.50	4.37	5.50
7	2.43	0.67	0.02	2.90	46.75	3.63	9.65
8	2.37	0.56	0.00	0.00	47.50	4.23	1.60
9	2.33	0.48	0.02	4.00	31.75	4.85	6.20
10	2.94	0.59	0.16	21.33	30.50	4.98	17.90
11	2.77	0.75	0.06	7.41	46.00	3.69	7.80
12	2.87	0.82	0.02	2.38	46.75	3.50	1.40
13	2.64	0.74	0.00	0.00	62.50	3.57	1.50
14	2.72	0.66	0.11	14.29	39.25	4.12	15.55
15	2.53	0.66	0.05	7.04	41.25	3.83	9.85
16	2.47	0.64	0.06	8.57	43.50	3.86	10.35
17	2.39	0.63	0.02	3.08	46.75	3.79	5.55
18	2.33	0.53	0.05	8.62	35.75	4.40	5.15

Three different sets of ideal process parameters were found for each powder mix under study, based on the data shown in Table 17, the porosity values, and the highlighted values pertaining to the three geometric aspects previously addressed. These settings will be applied in the MMC coating deposition process that follows. An x-z cross-section of the single tracks selected for the MMC coating deposition is shown in Figure 82.

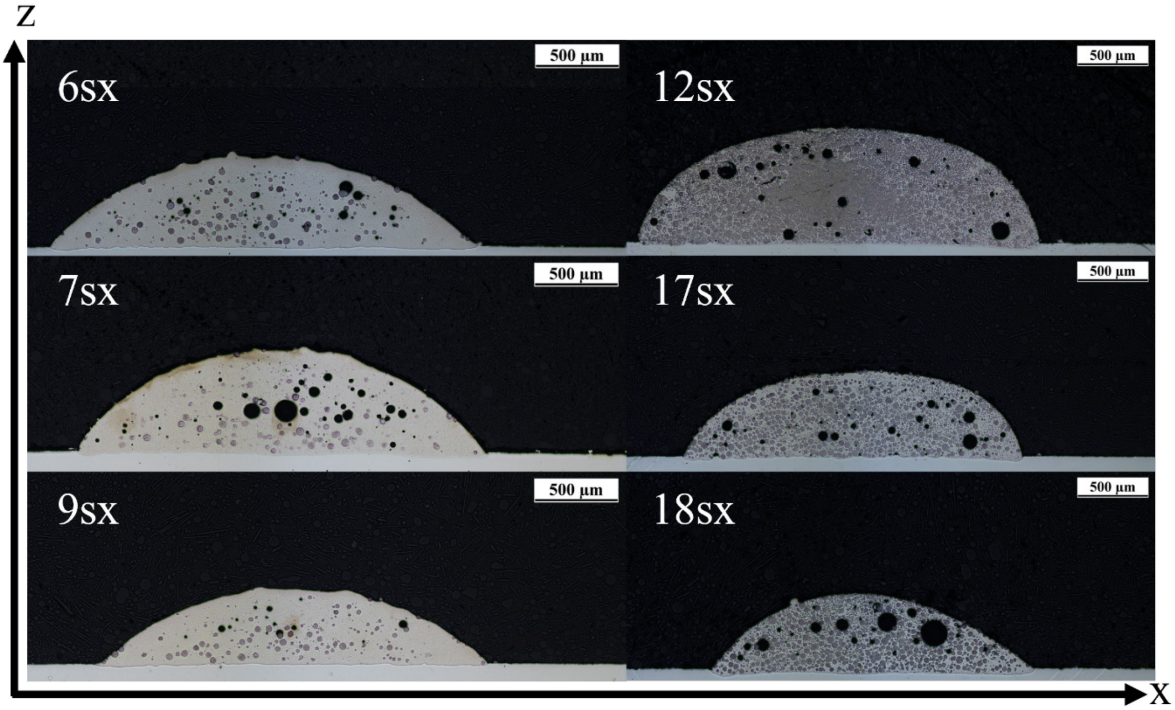

Figure 81 - Microscopic view showing the cross-sectional profiles of single tracks selected for subsequent MMC coating fabrication.

Table 15 offers a comprehensive explanation of the six sets of process parameters selected for the deposition of MMC coatings. Furthermore, using the mathematical framework proposed by Angelastro et al. [257], the geometric evaluations performed on the individual tracks were utilized to calculate important parameters like the hatch distance (Sx) and the overlap percentage (%Ox) between consecutive tracks, as well as the hatch distance between consecutive layers (Sz). The values of these parameters are displayed in Table 18. Furthermore, Figure 83 shows a macrograph that shows the six produced coatings from above.

Table 15 - MMC coating with corresponding geometric values.

MMC coating	Single corresponding track	Sx (mm)	Ox (%)	Sz (mm)
1C	6	1.80	30.92	0.37
2C	7	1.74	30.14	0.41
3C	9	1.64	31.40	0.31
4C	12	2.04	29.29	0.54
5C	17	1.70	30.08	0.41
6C	18	1.62	30.32	0.37

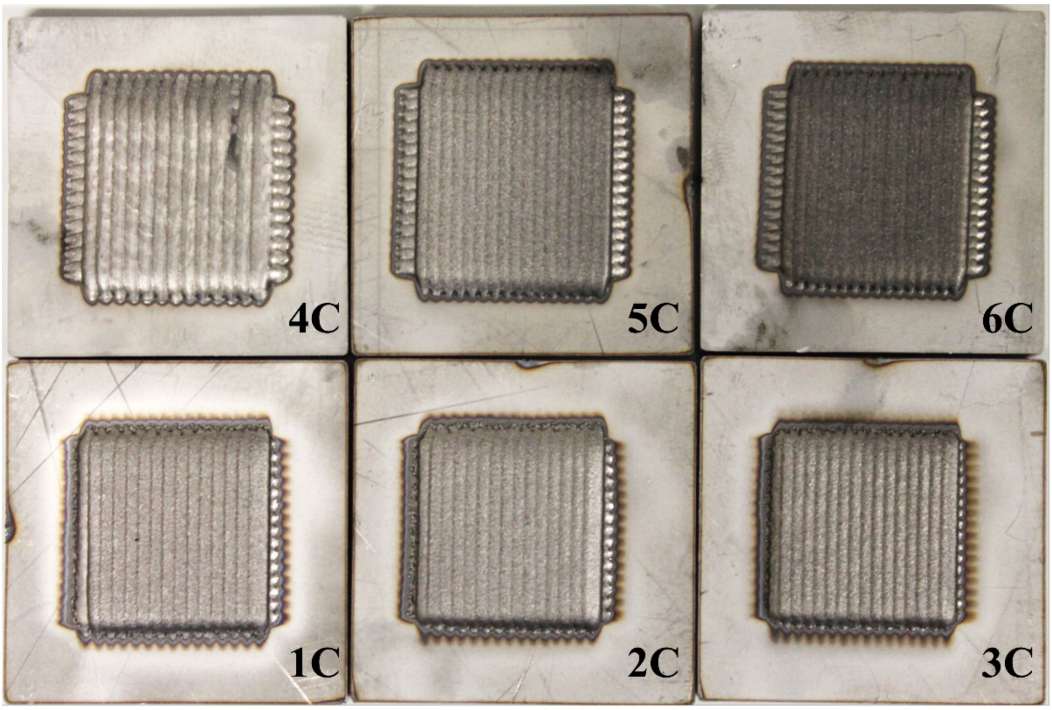

Figure 82 - Top view macrograph showing the six fabricated MMC coatings.

3.2.3 Comprehensive assessment of the microstructure, mechanical test, and compositional analysis of MMC coatings.

3.2.3.1 Microstructure analysis

The optical microscope pictures of the metallographic specimens from coatings 3C (Figure 84a-c) and 6C (Figure 84d-f) are displayed in Figure 84. For practically all of the particles in the 10% reinforcement coating, the reinforcement phase maintained a spherical shape. This demonstrates that the reinforcing particles were prevented from melting by the process settings employed. Conversely, coatings containing 40% reinforcement have a small amount of individual carbide grains dispersed throughout the metal matrix. The differences in behavior can be attributed to the combination of process parameters applied to the two samples displayed in Figure 84. The combined parameter S ($S=P\sqrt{TS-1}\sqrt{PFR-1}$) dependent on the three variable process parameters was used to compare the energy input needed in the realization of the six coatings [258,259]. S is a measurable quantity that is determined by the laser power, translation speed, and powder feed rate. It indicates the precise amount of energy that is applied to both the substrate and the coating material. The value of S in sample 6C is roughly twice that of sample 3C. Higher heat input is the outcome of this significant difference for both WC-Co-Cr and Colmonoy 227-F powders. Because of this, during deposition, elements like chromium and cobalt, which functioned as the tungsten carbide grains' binder in the WC-Co-Cr powder, melted

more readily, making it easier for the tiny carbide particles to distribute in the nickel alloy matrix. Table 19 displays the S-parameter value for each test specimen.

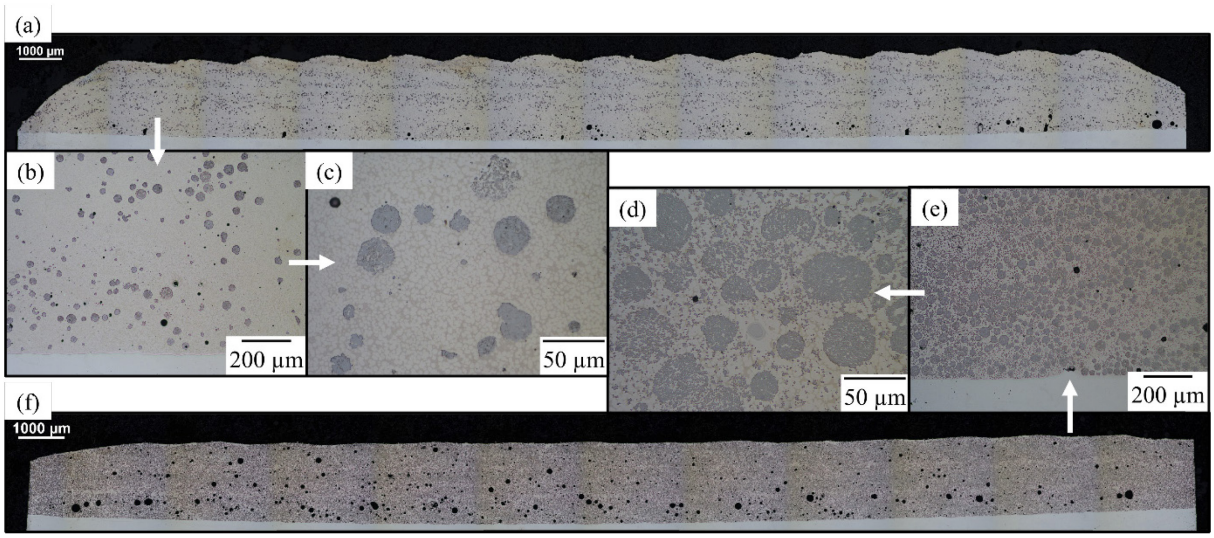

Figure 83 - Micrographs of metallographic specimens at different magnifications: (a-c) specimen 3C, (d-f) specimen 6C.

Table 16 - S-parameter values.

MMC coating	Laser Power, P (W)	Translation Speed, TS (mm/min)	Powder Feed Rate, PFR (g/min)	Specific Energy, S (J·s/mm·g)
1C	2200	820	14	690
2C	2000	620	10	1161
3C	2000	820	12	732
4C	2400	570	6	2526
5C	1600	470	10	1226
6C	1600	570	8	1263

Furthermore, in contrast to other tests reported in the literature, it was possible to observe that there is no indication of WC melting in the metal matrix [181]. For this reason, it is evident that the objective of preventing the carbide phase from fusion was achieved. Because of this outcome, hierarchical resolidification structures—which can lead to the development of cracks or other kinds of defects in MMCs—can be prevented [158,169].

Figure 85 displays the microstructure of sample 2C. The nickel-rich γ-phase, which is the lighter portion of the sample cross-section, and an incredibly diffuse network of compounds like chromium carbides and borides make up the coating's metal matrix.

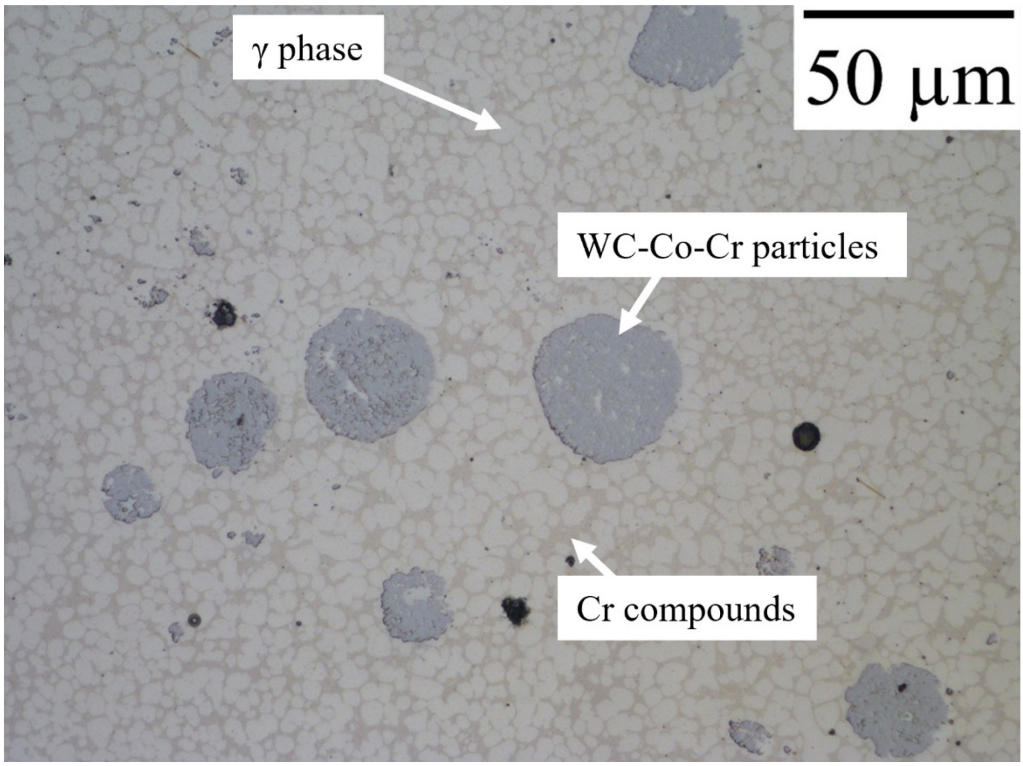

Figure 84 - Micrograph of sample 2C showing the microstructure of the Ni-rich matrix in which chromium carbides and borides are dispersed as precipitates.

Low porosity values were found in the measurements made using image analysis for both kinds of powder combinations. The porosity of samples 1C through 3C ranged from 0.8% to 1.2%, but sample 6C had a measured value of 2.45% (refer to Figure 86c). In terms of porosity distribution, it is evident that the porosity is concentrated in the zone near the substrate, both in terms of average size and quantity, rather than being evenly distributed throughout the coating. As an example, Figure 86a, which displays sample 2C, and Figure 84f, which displays sample 6C, can both be used to deduce this conclusion. The trends seen in Figure 86b can be obtained by analyzing the porosities with respect to their position in the clad, both in terms of size and numerosity. In respect to the overall amount of these discontinuities for each of the two coatings, 2C and 6C, the vertical bars show the proportion of pores for each layer. The trend of the total pore areas in each layer in relation to the total pore areas in each of the two coatings—2C and 6C, respectively—is depicted by the dotted and solid lines.

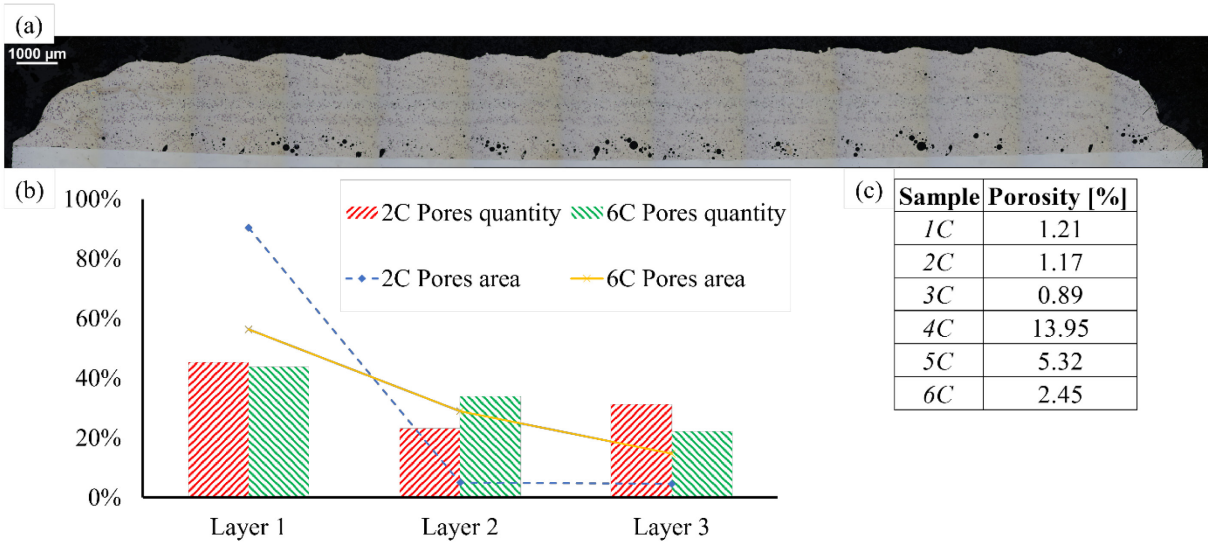

(c)

Sample	Porosity [%]
1C	1.21
2C	1.17
3C	0.89
4C	13.95
5C	5.32
6C	2.45

Figure 85 - (a) Low magnification micrograph of sample 2C showing the distribution and size of the pores; (b) comparison of samples 2C and 6C in the distribution of porosity in the coating; (c) Sample's porosity measurement results

To acquire three-dimensional information regarding the distribution and morphology of the discontinuities present, a more thorough analysis would need to look at many sections of the same specimen, all of which would need to be examined parallel to and equally spaced from one another [260]. Future developments of this experimental investigation will carry out analyses of this kind.

3.2.3.2 Hardness tests

Vickers microhardness measurements allowed the mechanical characteristics of the reinforcement and matrix to be determined separately. In reality, by getting 1275±25 HV as the average result of the various test repetitions, it was possible to confine the area of hardness indentation to reinforcing powder particles by applying a lower load of 2 N. The microhardness of the metal matrix of the coatings was tested using the same methodology; in this instance, the average value was 325±10 HV, which is precisely the hardness value of Colmonoy 227-F [257]. Consequently, this number verified that the reinforcing particles—which are primarily made of Colmonoy 227-F—did not disintegrate in the matrix. The second set of hardness tests used a 2.5 mm diameter sphere and an HB30 hardness scale. This allowed for a more thorough examination of a broader area of the coating, which included a sizable number of reinforcing particles in addition to the Colmonoy 227-F matrix. Using the tables from the international standard ASTM E140-12B (2012)e1, the findings obtained with this scale have been translated into Vickers hardnesses [261]. This allowed comparing the results of the several experiments and figuring out the effects of the various WC-Co-Cr percentages in the powder mixture easy.

The results demonstrated a higher coating hardness when compared to the metal matrix alone; the degree of this increase is obviously influenced by the proportion of WC-Co-Cr powder in the mixture. The coating hardness achieved for the combination including 10% WC-Co-Cr powder was 375±15 HV, indicating a 15% increase in hardness; for the mixture containing 40% WC-Co-Cr powder, the coating hardness obtained was 490±10 HV, representing a 50% increase in hardness. Improvements in mechanical performance (and thus resistance to abrasive wear) seemed to be directly correlated with the weight percentage of WC-Co-Cr powder in the alloy. The weighted average of the values of each coating component, determined by their respective mixing proportions, was higher than the measured hardness values. The unusual distribution of the reinforcing particles in the coating may be the cause of this outcome. As a matter of fact, they do not create a continuous network where every reinforcement grain is in contact with one or more other grains—a necessary condition for giving the material a high degree of hardness [262].

3.2.3.3 Guided-Bend test

To confirm the strength of the deposit to the substrate during severe external deformation, bending tests were performed. The basic processes are depicted in Figure 87. The test specimens were created using the same process parameters as the 3C and 6C specimens, as indicated in Table 19.

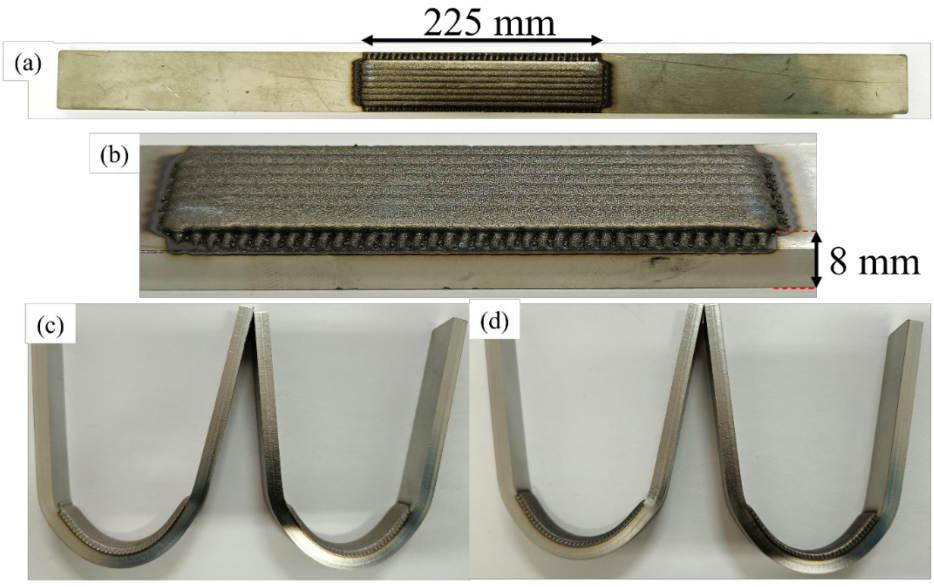

Figure 86 - (a) Guided bend specimen appearance; (b) deposit detail showing total thickness of substrate and deposit; (c-d) appearance of specimens 3C (c) and 6C (d) after the test, in which a deformation of almost 180° can be observed.

Figure 88a-d demonstrate that neither the surface nor the interior of the material under analysis contain any discontinuities or delaminations. Sectioning one of the specimens displayed in Figure 9c at the site of maximal curvature allowed for a metallographic study to be performed, which provided more in-depth information on the internal integrity of the deposit. At different magnifications, the metallographic sections were inspected to make sure there were no non-surface flaws or a lack of adhesion between the deposit and the substrate.

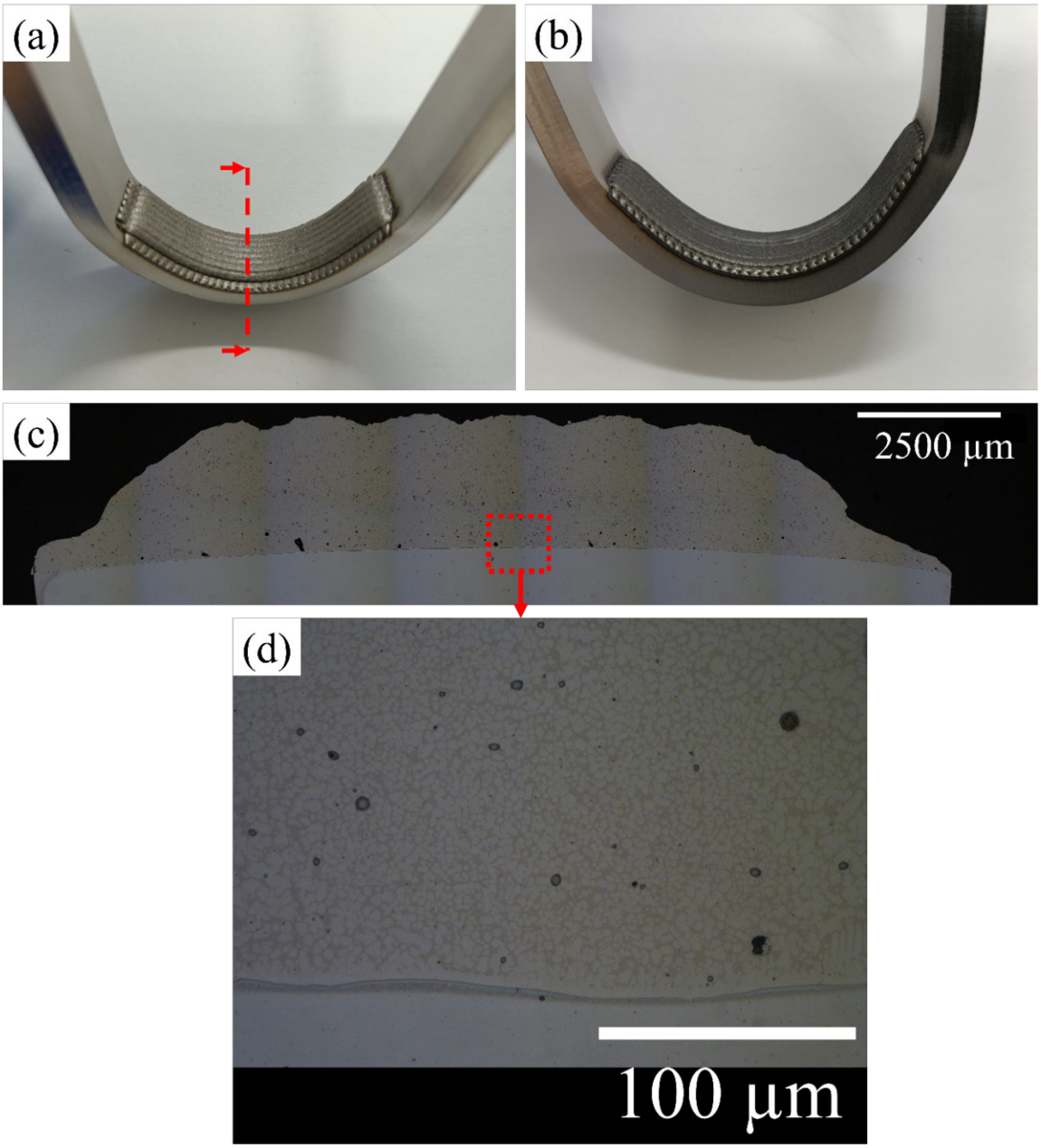

Figure 87 - (a-b) Appearance of specimens 3C and 6C at the end of the bending tests; (c) micrograph of the specimen in Figure 88a, taken along the direction of section indicated by the dashed line; (d) higher magnification of the section shown in Figure 88c within the area enclosed by the dotted line.

3.2.3.4 Compositional analysis of the coatings

The presence of chemical components typical of the two powders in a particular area of the metallographic samples was identified and quantified by SEM analysis. The region of sample 3C (red dashed line) that underwent chemical analysis using an EDX probe is seen in Figure 89a. The outcomes displayed in Figure 89b align with the initial materials' chemical makeup. A closer-up view of one of the coating's reinforcing particles is displayed in Figure 89c. The WC grains are shown in this picture to be in contact with one another and submerged in the binder that Cr and Co have created. It is evident from the maps of the distributions of Ni and Co (see Figure 89d) that there is very little diffusion of the atoms of both elements from the matrix in the direction of Co, and in the opposite direction for Ni, towards the reinforcement.

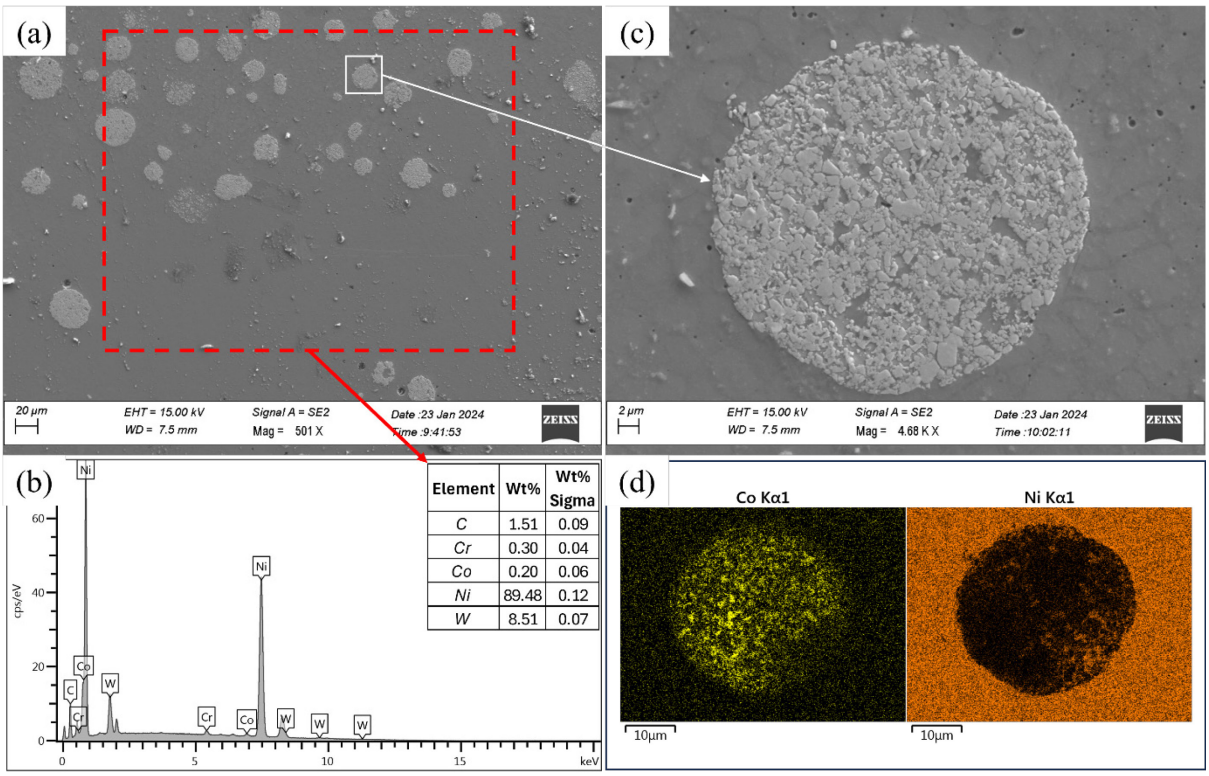

Figure 88 - Area of sample 3C on which chemical composition was measured by EDX probe; (b) spectrum and chemical composition of the area inside the red dotted line in Figure 89a; (c) detail of the reinforcement particle in the solid white line in Fig. 8a; (d) maps of the distribution of Ni and Co elements in the area shown in Figure 89c.

In actuality, Table 16 displays the chemical makeup of Colmonoy 227-F powder, which is devoid of any Co traces. The same thing can be said for coating 6C (see Figure 90), where the mixture's two powder percentages affected the chemical analysis's outcome (see Figure 90b) but still showed the same chemical diffusion phenomenon between the two materials.

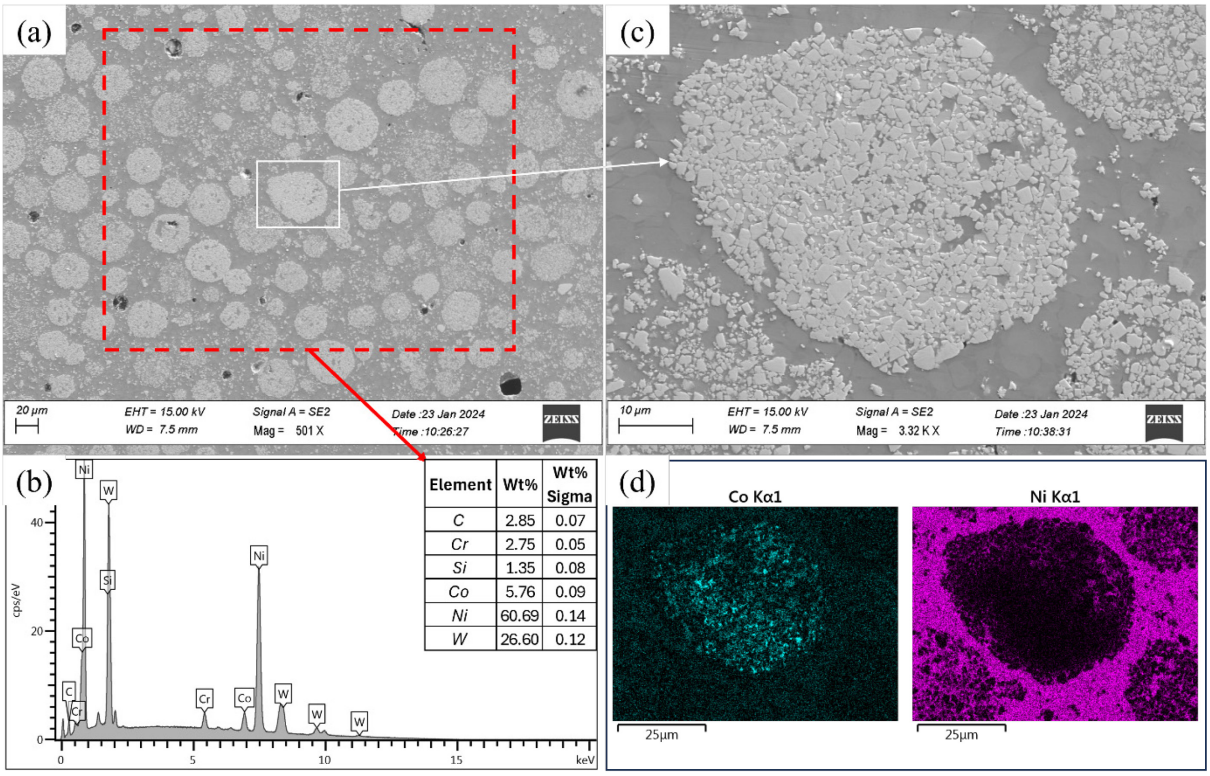

Figure 89 - (a) Area of sample 6C on which chemical composition was measured by EDX probe; (b) spectrum and chemical composition of the area inside the red dotted line in Figure 90a; (c) detail of the reinforcement particle in the solid white line in Fig. 9a; (d) maps of the distribution of Ni and Co elements in the area shown in Figure 90c.

Analytical verification of how closely the resultant coatings' composition matched that of the two deposited powder combinations was done using an image analysis approach. The specimen images captured with the optical microscope were first segmented in order to distinguish the various entities present in the areas that were imaged. The image analysis program offers a number of tools for this purpose. The segmentation approach selected is known as "Trainable Weka Segmentation," and it enables the division of picture pixels into distinct categories based on data entered by the user during the training phase. The low magnification micrographs of specimens 1C and 6C are displayed in Figure 91a and Figure 91b. From these, it is evident that the areas of the metallographic specimens may be classified into three different entities: matrix, voids, and reinforcing powder particles. This is true whether or not the substrate is present.

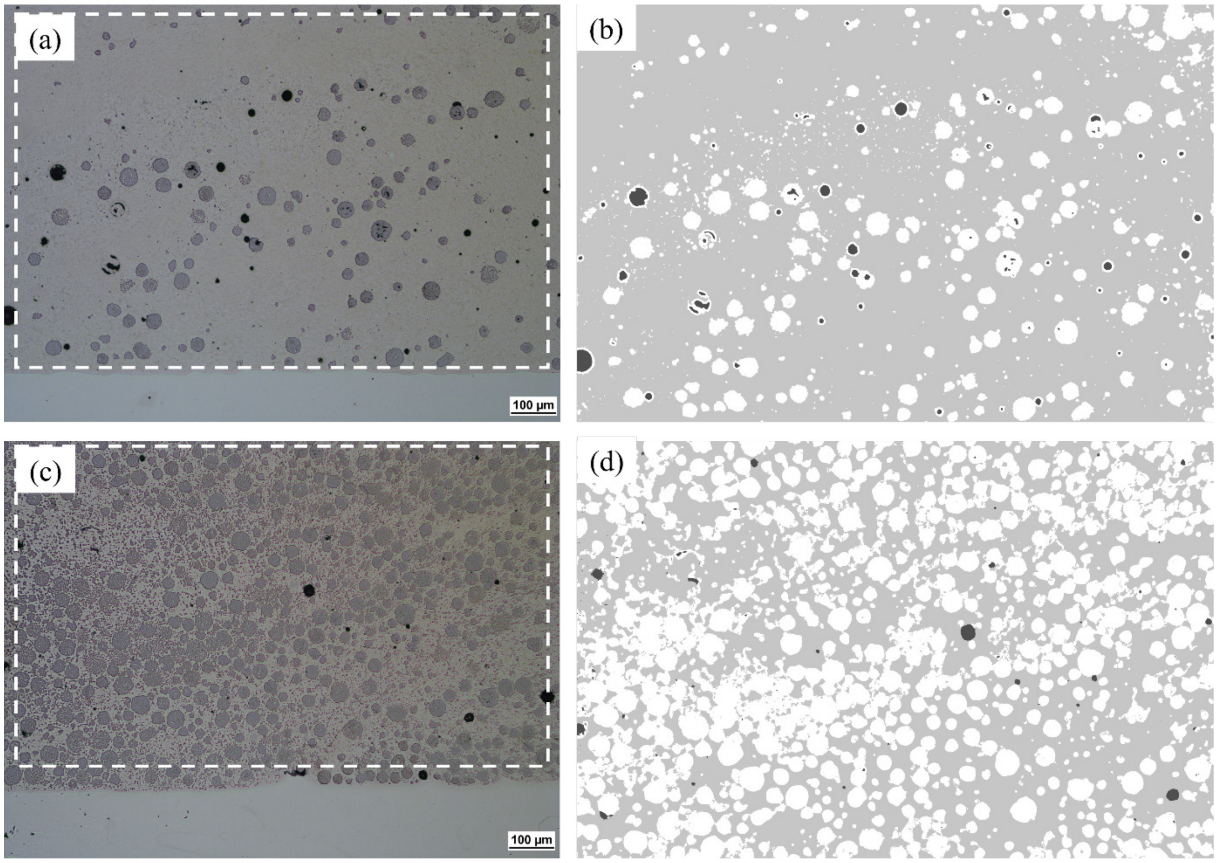

Figure 90 - (a-c) Micrographs of samples 1C and 6C used to calculate the percentage of reinforcing powder by image analysis; (b-d) areas enclosed by the dashed white lines in Figure 91a and Figure 91c after the image segmentation process.

The following formula can be used to determine the weight percentage of reinforcing particles in the coating:

$$\%wt = 100\frac{M_2}{M_1+M_2} \quad [1]$$

where subscript 1 refers to Colmonoy 227-F and subscript 2 to WC-Co-Cr powder. This formula can be rewritten as follows:

$$\%wt = 100(1 + R_M)^{-1} \quad [2]$$

where R_M is the ratio between M_1 and M_2. Since R_M can be written as the product of R_V (ratio between the volumes of the two powders V_1 and V_2) and $R\rho$ (ratio between the densities of the two materials ρ_1 and ρ_2), eq. 2 can be reformulated as

$$\%wt = 100\left(1 + R_V \cdot R_\rho\right)^{-1} \quad [3]$$

Since this analysis was done on images of cross sections instead of volumetric samples of the coatings, the following relationship must be considered:

$$R_V = (R_A)^{3/2} \quad [4]$$

where R_A is the ratio of the A1 and A2 areas, which can be measured directly from the optical microscope images. Thus, Eq. 3 can be rewritten in the following form

$$\%wt = 100\left[1 + \left(\frac{A_1}{A_2}\right)^{3/2} \cdot \frac{\rho_1}{\rho_2}\right]^{-1} \quad [5]$$

The density values of the two materials were 0.00853 g/mm3 for Colmonoy 227-F and 0.0137 g/mm3 for WC-Co-Cr (calculated as a weighted average of the densities of WC, Co, and Cr according to their percentages in the reinforcing powder). Measurements were taken on areas of 1 mm2 (enclosed by the white dashed lines in Figure 90a and Figure 90c) to determine areas A1, A2, and Avoid. The measurement results, which are displayed in Table 7, attested to the fact that the produced coatings' composition closely matched that of the deposited mixes.

Table 17 - Results of image analysis for the verification of the composition of mixtures.

	10% Mixture	**40% Mixture**
	mm²	
A_1	0.8552	0.6312
A_2	0.1381	0.3650
A_{void}	0.0068	0.0038
%wt	**9.39**	**41.26**

To ascertain the coating's composition, XRD analysis was used to the samples. Figure 92 presents the findings. The spectra's analysis verifies that only Ni crystals—which stand in for Colmony 227-F's metal matrix—and WC are present. W2C and Cr compound levels show no peaks. The presence of W2C and chromium carbides has been demonstrated in multiple studies to be deleterious to mechanical characteristics and resistance to specific surface corrosion mechanisms [263,264], therefore this result is quite encouraging. A comparison of the spectra of the two samples under analysis demonstrates that the samples containing 40% WC-Co-Cr powder exhibit an increase in WC crystal peaks and a concurrent decrease in Ni crystal peaks.

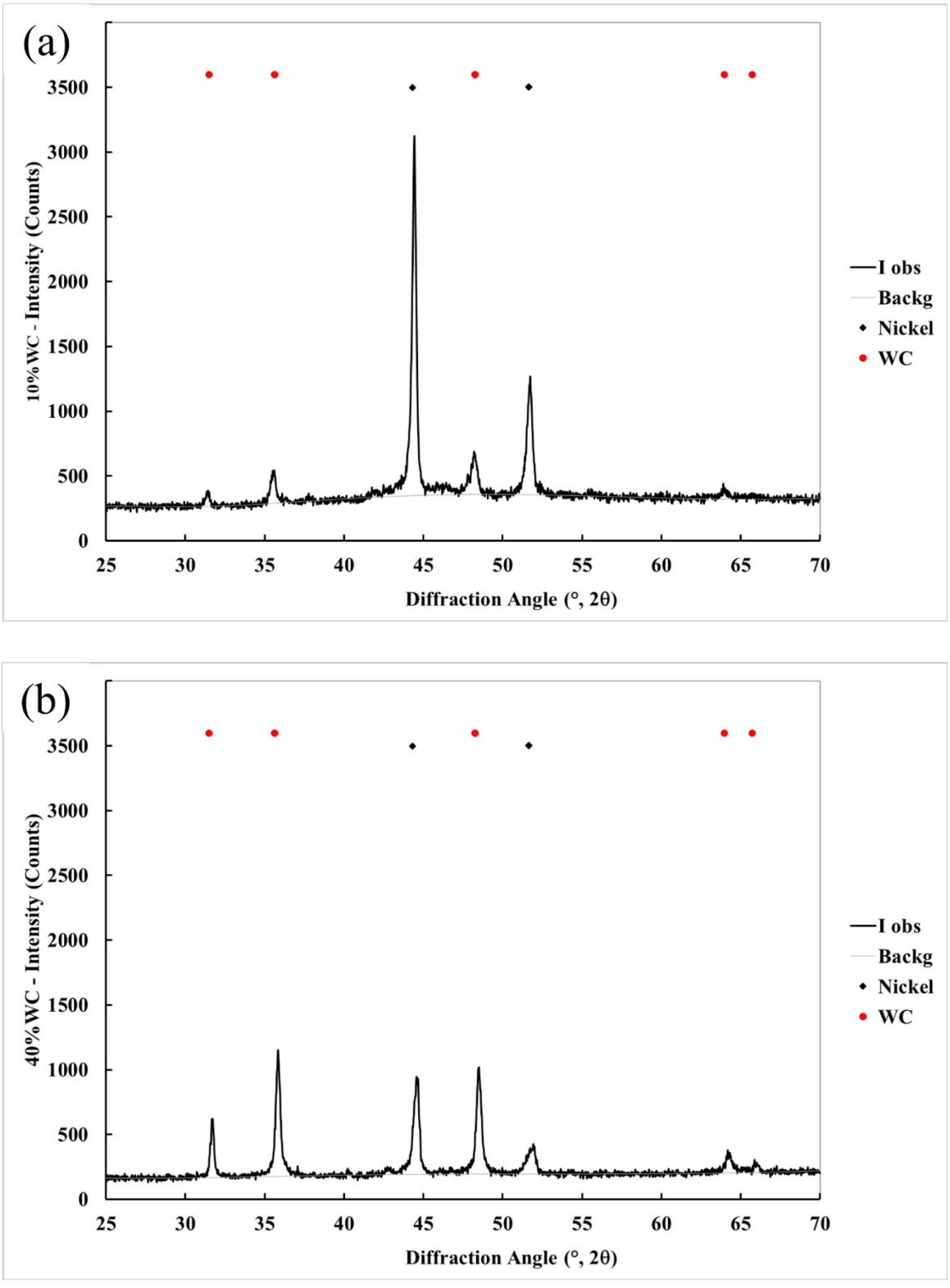

Figure 91 - (a) Results of XRD analysis performed on 3C and (b) 6C.

3.2.4 Conclusions

This work included a detailed investigation of the mechanical performance and microstructural properties of laser-deposited MMC coatings made using WC-Co-Cr reinforcement and Colmonoy 227-F matrix. The aim of the study was to address the significant challenges that have been documented in the literature regarding the production of wear-resistant coatings in metal-working composites (MMC) and to assess how the mechanical properties of the coating improve as the proportion of reinforcement increases. A Taguchi experimental design was used to examine three distinct levels of three process parameters (laser power, translation speed, and powder feed rate) for each of the two reinforcing percentages (10% and 40% by weight) that were examined. The study effectively determined a set of process parameters that were especially designed for the 3C and 6C coatings, and were optimized for each reinforcement % based on the characterizations that were carried out. The carbide phase was almost entirely preserved in a spherical morphology for coatings with 10% reinforcement, according to microstructural analysis. This suggests that the process conditions employed were effective in preventing carbide phase melting. On the other hand, coatings that included 40% carbide showed a little amount of non-critical dispersion of individual carbide grains inside the metal matrix. The coatings' average microhardness of 325±10 HV in the metal matrix is in line with Colmonoy 227-F's hardness value. This demonstrates that the reinforcing WC-Co-Cr particles did not mix in with the matrix. Furthermore, the coating's hardness rose as the WC-Co-Cr content increased, reaching 375±15 HV for the 10% reinforcement and 490±10 HV for the 40% retention. The distinctive elements of the two materials were sufficiently dispersed in the coating, according to a chemical composition study, and there was very little diffusion of nickel and cobalt atoms between the matrix and the reinforcing phase. The resultant coatings' composition was finally verified by optical microscope image analysis to be nearly identical to the deposited mixtures' composition, with true WC-Co-Cr percentages of 9.39% for the first powder mixture and 41.26% for the second powder mixture. According to these findings, MMC coatings made by laser deposition under optimum conditions have a good microstructure, more hardness, and the right amount of components distributed throughout. These characteristics are essential for enhancing the coatings' wear resistance and mechanical performance, which makes them suitable for use in extremely abrasive settings.

Concluding Remarks

At the end of this course of bibliographic and experimental research, it is possible to summarize the results obtained and compare them with those in the relevant scientific literature already mentioned in the previous paragraphs. It is also possible to highlight the contributions made to the state of the art, which could have a significant scientific and social impact and could be an impetus for further research in the field of MMAM.

Several experimental studies have been conducted to produce multi-material metal components using a machine designed to perform the PBF-LB manufacturing process. This machine is not equipped with systems that allow the simultaneous use of two materials to obtain a bi-material component at the layer level. Therefore, special equipment was designed and built to overcome the technological limitations of the existing machine. This was the first attempt in the scientific literature to demonstrate the feasibility of this idea.

Different pairs of materials, creating a sharp transition between them, were used in the various experiments to verify their metallurgical compatibility through various types of metallographic, chemical and mechanical analyses. The following results should be noted in this regard:

- A strong metallurgical bond between AISI 316L and Nickel Superalloy was demonstrated by the presence of swirls brought on by Marangoni convection in the interface area; this conclusion was corroborated by the steady and gradual variation in the microhardness and concentration of the two alloys' characteristic elements (Fe, Ni, and Ti).
- Metallurgical analyses of the interface reveal excellent bonding between AISI 316L and 18-Ni 300 (Maraging); there are no cracks or porosities in the transition zone.
- The EDS and hardness test results from the interface between AISI 316L and 18-Ni 300 (Maraging) witness to the excellent quality of the metallurgical bond between the two materials; the transition zone's slow and consistent trends confirm the absence of brittle intermetallic compounds.
- Tensile tests verify that the interface between AISI 316L and 18-Ni 300 (Maraging) strength is greater than that of AISI 316L, demonstrating that the bi-material specimens fracture on the weak region.
- An intralayer multi-material powder bed fusion technique is effectively used to create bimetallic lattice structures of 17-4PH and 316L stainless steel.

- The material interface between 17-4PH and AISI 316L exhibits strong and complete fusion and is shown to be resilient to compressive force in both parallel and series.

Similar experiments were performed between different pairs of materials, but this time special equipment was used that could determine the transition from one material to another in a gradual and continuous manner, creating what is called a Continuous Functionally Graded Material (cFGM). Again, interesting results were obtained, which can be summarized as follows:

- a blade-based powder spreading method was successful applied to create samples of continuous functionally graded materials (cFGMs) within the same layer for the first time.
- The metallographic examination showed that, in specimens made by AISI 316L and 18-Ni 300 (Maraging), a fine dual-phase microstructure of austenite and martensite produces two elongated zones along the layers, perpendicular to the direction of powder deposition.
- As envisaged by the powder separation system, the results of the comprehensive microhardness tests confirmed the presence of a continuous and gradual transition zone. These outcomes confirm that the two materials were sufficiently connected.
- The cFGM specimens, as determined by the microstructure and composition gradient, exhibited ductile behavior with good strength (UTS between 650MPa and 700MPa) and ductility (elongation at break between 24% and 28%), similar to AISI 316L.
- Optical microscopy showed that the discontinuities from 18Ni Maraging 300 to AISI 316L gradually decreased in both number and width.
- A significant concentration of porosity was found in the area where the processing parameters were changed in specimen divided into two processing zones and created using varying scanning speeds. However, there were no concentrated discontinuities in the areas where scan speeds varied in specimen made with distinct process parameters for each of the three composition zones.
- Residual stress analysis revealed that the residual stress field in specimen made without heat treatment and with a single scanning speed of 180 mm/s, had tensile stress concentrations at the top and bottom surfaces. Compression at the center counterbalanced these, and the top surface of 18Ni Maraging 300 showed the most significant stress, measured at 850 MPa. Additionally, the specimen's upper surface showed a decrease in peak residual stresses following the application of heat treatment. Notably, the base material 18Ni Maraging 300 showed the greatest stress relaxation,

lowering the maximum tensile stress from 850 MPa to 450 MPa by nearly 50%. Furthermore, the maximum tensile stress was lowered to 700 MPa in specimen by using two distinct scan rates. Additionally, the maximum tensile stress was further reduced to about 560 MPa in specimen made by three different process parameters. Significantly, it was discovered that the residual stresses throughout the component were decreased. This was accomplished by applying appropriate heat treatment in conjunction with three distinct process parameters for each of the three composition zones.

- The interface of the samples produced made by AISI 316L and Nickel Superalloy seemed to be free of defects like lack of fusion and delamination, which is synonymous with the good metallurgical bond created between the materials. The metallographic examinations have shown that the designed system is feasible for producing cFGMs components at the layer level.
- According to the hardness tests, there was a continuous and progressive change in mechanical properties within a graded zone that was equal to the one that the divider (20 mm, along the Y direction) defined. Furthermore, the findings of the hardness test indicated that the mutual position of the starting materials has a minimal impact on the samples' final mechanical characteristics.
- All of the samples' chemical characteristics varies along the grading direction, according to the chemical analyses; however, the same analyses also showed that the relative position of the various powders had an impact on the outcome.

In order to study the applied PBF-LB process in depth, an optical monitoring method was used to acquire a great deal of information about the quality of the powder bed during laser beam scanning. In fact, by applying this data acquisition methodology and coupling it with image analysis, it was possible to obtain information on the size of the interface (which affects the contamination between materials), the stability of the process as the layers progress, and the actual geometry of the samples produced. These results can be summarized as follows:

- Throughout the whole construction, the layer-by-layer variation in the real interface profile between the two materials and the ideal (linear) one could be observed in real time thanks to the deployment of the layer-wise in-situ optical monitoring system. By avoiding material contamination, this approach made it possible to guarantee the excellent quality of the final product without requiring extra, expensive, and time-consuming inspections.

- The results can be quite similar to those obtained using methods based on electron or optical microscopy, provided that the imaging system's resolution is enough for the purpose.
- Optical monitoring provides a viable alternative to more invasive, costly, and time-consuming methods for geometric characterization of parts made using the PBF-LB process, even for multi-material components.
- Cross-contamination across materials can be detected using optical monitoring of a multi-material PBF-LB process, provided that the materials respond differentially to the laser beam.
- In cFGM fabrication processes, optical monitoring demonstrated the very gradual transition between the two materials and the existence of a transition area comparable to that intended by the powder separation system. It also demonstrated that the zone of pure material was free of contamination. Every layer that was examined had excellent repeatability, which suggests that the process is generally steady and free of unusual fluctuations. The results also demonstrated that the position on the fabrication platform has no effect on the final product.

The L-DED process for the fabrication of multi-material metal components was also used in this thesis. This type of additive process also lends itself to some of the analyses performed in the experiments described above, and the main results can be summarized as follows:

- An optical monitoring methodology (CCD camera + real-time image processing) was used to support the successful application of a Directed Energy Deposition (DED) coating on AISI 316L components made by Laser-Powder Bed Fusion (PBF-LB) using 18 Ni(300) maraging steel powder and subsequent heat treatment. This allowed for the real-time observation of the melt pool, confirming the stability of the coating process.
- The hardness decreased to 200 HV at the substrate-coating contact and the first layer from an average of 235 HV in the PBF-LB component. According to scientific literature, coatings with three, five, or ten layers have a hardness of 375 HV at initial coating and 580 HV after treatment.
- The microstructural characteristics that the as-coated and after-treatment coatings acquire are significantly correlated with the hardness results. In particular, the microstructure produced by solution annealing in conjunction with age-hardening treatment is known as lath martensite. Intermetallic compounds rich in nickel precipitate

inside the lath martensitic structure, strengthening the hardness by precipitation and causing aging.

- The results of the investigation established whether it would be possible to use the DED technology to make a composite with an AISI 316L core, which was obtained through the PBF-LB process, covered with 18Ni (300) maraging tool steel. The 3-layer, 5-layer, and 10-layer coatings were really found to have very high performance because of their low porosity and perfect metallurgical interface, which was devoid of discontinuities such as delamination, cracks, and lack of fusion and adhesion. In the end, this study aims to reduce the cost of tool and die fabrication while preserving good surface mechanical properties for the final product by leveraging the benefits of the two AM techniques.
- It was possible to use a mixture of Colmonoy 227-F and WC-Co-Cr powders to improve the wear resistance surface properties of an AISI 316L steel substrate. By optimizing the process parameters, it has been possible to identify an operating window in which only Colmonoy 227-F is melted, while the carbide-rich powder, which remains in the solid state, is incorporated, contributing to the improvement of the mechanical properties of the deposit without modifying its chemical composition and ductility.

REFERENCES

[1] Oh et al. (2019), https://doi.org/10.1016/j.optlastec.2019.04.012

[2] Lewis et al. (2015), https://doi.org/10.1016/j.wear.2015.02.027

[3] Samei et al. (2021), https://doi.org/10.1016/j.addma.2021.102068

[4] Wei et al. (2018), https://doi.org/10.1016/j.matdes.2017.10.020

[5] Errico et al. (2022), https://doi.org/10.1016/j.surfcoat.2021.127965

[6] Rajaguru et al. (2020), https://doi.org/10.1016/j.matpr.2019.06.728

[7] Liu et al. (2018), https://doi.org/10.1016/j.promfg.2018.07.104

[8] Bogdan et al. (2020), https://doi.org/10.3390/ma13204534

[9] Feenstra et al. (2021), https://doi.org/10.1016/j.cossms.2021.100924

[10] Mei et al. (2019), https://doi.org/10.1016/j.msea.2019.05.011

[11] Chen et al. (2019), https://doi.org/10.1016/j.msea.2019.02.097

[12] Saleh et al. (2020), https://doi.org/10.1016/j.compositesb.2020.108376

[13] Kunimine et al. (2020), https://doi.org/10.1038/s41598-020-65429-8

[14] Feenstra et al. (2020), https://doi.org/10.1007/s10853-020-04913-y

[15] Hasanov et al. (2021), https://doi.org/10.3390/jmmp6010004

[16] Demir et al. (2017), https://doi.org/10.1016/j.mfglet.2017.01.002

[17] Yan et al. (2020), https://doi.org/10.1016/j.addma.2019.100901

[18] Wei et al. (2018), https://doi.org/10.1016/j.cirp.2018.04.096

[19] Wei et al. (2019), https://doi.org/10.1016/j.addma.2019.100818

[20] Wei et al. (2020), https://doi.org/10.1088/2631-7990/abce04

[21] Ligon et al. (2017), https://doi.org/10.1021/acs.chemrev.7b00074

[22] Pajonk et al. (2022), https://doi.org/10.1016/j.jobe.2021.103603

[23] Galantucci et al. (2019), https://doi.org/10.1007/978-3-030-18180-2_12

REFERENCES

[24] Demir et al. (2022), https://doi.org/10.1016/j.jmatprotec.2021.117439

[25] Wei et al. (2021), https://doi.org/10.1080/17452759.2021.1928520

[26] Wang et al. (2022), https://doi.org/10.1016/j.ijmachtools.2022.103872

[27] Sefene et al. (2022), https://doi.org/10.1016/j.jmsy.2022.04.002

[28] Chen et al. (2020), https://doi.org/10.1016/j.jmatprotec.2020.116701

[29] Sun et al. (2020), https://doi.org/10.1016/j.addma.2020.101448

[30] Tey et al. (2020), https://doi.org/10.1016/j.addma.2019.100970

[31] Wei et al. (2021), https://doi.org/10.1016/j.addma.2020.101683

[32] Dolev et al. (2021), https://doi.org/10.1016/j.addma.2020.101657

[33] Demir et al. (2022), https://doi.org/10.1016/j.jmatprotec.2021.117439

[34] Wei et al. (2020), https://doi.org/10.1016/j.addma.2020.101138

[35] Zhang et al. (2019), https://doi.org/10.1115/1.4041427

[36] Wei et al. (2022), https://doi.org/10.1016/j.addma.2021.102588

[37] Wei et al. (2019), https://doi.org/10.1115/1.4043983

[38] Zhang et al. (2020), https://doi.org/10.1016/j.addma.2020.101113

[39] Cheng et al. (2022), https://doi.org/10.1016/j.addma.2021.102481

[40] Chueh et al. (2020), https://doi.org/10.1016/j.addma.2020.101465

[41] Wang et al. (2022), https://doi.org/10.1080/17452759.2022.2028343

[42] Errico et al. (2023), https://doi.org/10.1016/j.mfglet.2022.11.004

[43] Dolev et al. (2021), https://doi.org/10.1016/j.addma.2020.101657

[44] Azizi et al. (2019), https://doi.org/10.1016/j.addma.2019.03.025

[45] Yuchao et al. (2020), https://doi.org/10.1016/j.matchar.2020.110489

[46] Chen et al. (2020), https://doi.org/10.1016/j.msea.2020.139316

[47] Rafiee et al. (2020), https://doi.org/10.1002/advs.201902307

[48] Horn et al. (2019),

[49] Wang et al. (2022), https://doi.org/10.1080/17452759.2022.2028343

[50] Santecchia et al. (2020), https://doi.org/10.3390/met10030341

[51] Rittinghaus et al. (2022), https://doi.org/10.1007/s40516-022-00190-6

[52] Palm et al. (2020), https://doi.org/10.1016/j.procir.2020.09.044

[53] Montazeri et al. (2018), https://doi.org/10.1115/1.4040543

[54] Zhang et al. (2023), https://doi.org/10.1016/j.ijmecsci.2023.108477

[55] Tey et al. (2020), https://doi.org/10.1016/j.addma.2019.100970

[56] Sun et al. (2020), https://doi.org/10.1016/j.addma.2020.101448

[57] Wei et al. (2021), https://doi.org/10.1016/j.addma.2020.101683

[58] Chen et al. (2020), https://doi.org/10.1016/j.jmatprotec.2020.116701

[59] Chen et al. (2019), https://doi.org/10.1016/j.msea.2019.02.097

[60] Errico et al. (2023), https://doi.org/10.1016/j.msea.2023.145731

[61] Angelastro et al. (2023), https://doi.org/10.3390/met13091588

[62] Heidarzadeh et al. (2021), https://doi.org/10.1016/j.pmatsci.2020.100752

[63] Salih et al. (2023), https://doi.org/10.1016/j.ijmecsci.2022.107827

[64] Mac Ardghail et al. (2018), https://doi.org/10.1016/j.ijfatigue.2018.02.015

[65] Yang et al. (2015), https://doi.org/10.1016/j.jmapro.2015.06.024

[66] Schmelzle et al. (2015), https://doi.org/10.1115/1.4031156

[67] Roach et al. (2019), https://doi.org/10.1016/j.addma.2019.100819

[68] Benyahia et al. (2022), https://doi.org/10.1016/j.addma.2022.102993

[69] Ritchie et al. (2011), https://doi.org/10.1038/nmat3115

[70] Rocha et al. (2020), https://doi.org/10.1039/d0ta04181e

[71] Sajjad et al. (2022), https://doi.org/10.1016/j.ijheatmasstransfer.2022.123352

[72] Modrek et al. (2023), https://doi.org/10.1016/j.csite.2022.102684

[73] Suzuki et al. (2023), https://doi.org/10.1016/j.matdes.2023.111969

REFERENCES

[74] Sarabhai et al. (2023), https://doi.org/10.1016/j.matdes.2023.111787

[75] Gao et al. (2023), https://doi.org/10.1016/j.applthermaleng.2023.121098

[76] Nguyen et al. (2013), https://doi.org/10.1007/s12541-013-0144-5

[77] Boschetto et al. (2023), https://doi.org/10.3390/app13052809

[78] Cheng et al. (2017), https://doi.org/10.1108/RPJ-04-2016-0069

[79] Ramos et al. (2022), https://doi.org/10.1016/j.ijimpeng.2022.104202

[80] Tancogne-Dejean et al. (2016), https://doi.org/10.1016/j.actamat.2016.05.054

[81] Yu et al. (2022), https://doi.org/10.1016/j.addma.2021.102497

[82] Arabnejad Khanoki et al. (2012), https://doi.org/10.1115/1.4006115

[83] Mahmoud et al. (2017), https://doi.org/10.3390/jmmp1020013

[84] Yu et al. (2022), https://doi.org/10.1016/j.ijmecsci.2022.107531

[85] Sundararaman et al. (2023), https://doi.org/10.1016/j.matdes.2023.111649

[86] Mora et al. (2022), https://doi.org/10.1016/j.mattod.2022.05.008

[87] Khatri et al. (2023), https://doi.org/10.1089/3dp.2022.0196

[88] Yavas et al. (2022), https://doi.org/10.1016/j.matdes.2022.110613

[89] Tulpan et al. (2024), https://doi.org/10.1016/j.addma.2023.103902

[90] Prajapati et al. (2022), https://doi.org/10.1016/j.addma.2022.102766

[91] Verma et al. (2022), https://doi.org/10.1016/j.addma.2021.102463

[92] Zhang et al. (2020), https://doi.org/10.1016/j.compositesb.2020.108417

[93] Zhang et al. (2019), https://doi.org/10.1016/j.matdes.2019.107583

[94] Zhang et al. (2021), https://doi.org/10.1108/rpj-10-2020-0254

[95] Mahamood et al. (2017), https://doi.org/10.1007/978-3-319-53756-6_2

[96] Angelastro et al. (2017), https://doi.org/10.1088/2051-672X/aa8021

[97] Caiazzo et al. (2022), https://doi.org/10.1016/j.jmapro.2022.09.031

[98] Reichardt et al. (2021), https://doi.org/10.1080/09506608.2019.1709354

[99] Sam et al. (2021), https://doi.org/10.1016/j.jmapro.2021.06.062

[100] Ansari et al. (2021), https://doi.org/10.1016/j.jmatprotec.2021.117117

[101] Zhang et al. (2018), https://doi.org/10.1115/1.4039683

[102] Muller et al. (2013), https://doi.org/10.4028/www.scientific.net/AMR.698.117

[103] Tay et al. (2022), https://doi.org/10.1080/17452759.2022.2048521

[104] Kumar et al. (2023), https://doi.org/10.1080/10426914.2022.2075892

[105] Tan et al. (2020), https://doi.org/10.1016/j.ijmachtools.2020.103592

[106] Wang et al. (2021), https://doi.org/10.1007/s11771-021-4687-9

[107] Zhang et al. (2019), https://doi.org/10.1016/j.msea.2019.138209

[108] Liu et al. (2017), https://doi.org/10.1016/j.pmatsci.2017.04.013

[109] Woo et al. (2019), https://doi.org/10.1016/j.msea.2018.12.078

[110] Bartlett et al. (2019), https://doi.org/10.1016/j.addma.2019.02.020

[111] Fang et al. (2020), https://doi.org/10.1016/j.optlastec.2020.106283

[112] Ahmad et al. (2018), https://doi.org/10.1016/j.addma.2018.06.002

[113] Smudde et al. (2023), https://doi.org/10.1016/j.msea.2023.145266

[114] Braun et al. (2021), https://doi.org/10.1111/ffe.13552

[115] Shi et al. (2023), https://doi.org/10.1016/j.ijfatigue.2022.107469

[116] Ye et al. (2021), https://doi.org/10.1016/j.jmatprotec.2021.117317

[117] Dubey et al. (2022), https://doi.org/10.1021/acsbiomaterials.1c01416

[118] Rouf et al. (2022), https://doi.org/10.1016/j.jor.2022.06.013

[119] Lin et al. (2005), https://doi.org/10.1016/j.msea.2004.08.072

[120] Lin et al. (2005), https://doi.org/10.1016/j.msea.2005.05.024

[121] Hilzenthaler et al. (2021), https://doi.org/10.1016/j.powtec.2021.06.011

[122] Sutton et al. (2020), https://doi.org/10.1016/j.addma.2019.100981

[123] Liu et al. (2014), https://doi.org/10.1016/j.matchar.2014.05.001

REFERENCES

[124] Escano et al. (2019), https://doi.org/10.1080/08940886.2019.1582281

[125] Habiba et al. (2023), https://doi.org/10.3390/ma16072824

[126] Mercelis et al. (2006), https://doi.org/10.1108/13552540610707013

[127] Kruth et al. (2012), https://doi.org/10.1177/0954405412437085

[128] Wu et al. (2014), https://doi.org/10.1007/s11661-014-2549-x

[129] Lu et al. (2015), https://doi.org/10.1016/j.optlastec.2015.07.009

[130] Strantza et al. (2021), https://doi.org/10.1016/j.addma.2021.102003

[131] Simson et al. (2017), https://doi.org/10.1016/j.addma.2017.07.007

[132] Mishurova et al. (2019), https://doi.org/10.1016/j.addma.2018.11.023

[133] Ali et al. (2018), https://doi.org/10.1016/j.msea.2017.11.103

[134] Casavola et al. (2009), https://doi.org/10.1243/03093247JSA464

[135] Li et al. (2018), https://doi.org/10.1016/j.ijmecsci.2017.12.001

[136] Shan et al. (2023), https://doi.org/10.1016/j.addma.2022.103378

[137] Ghanavati et al. (2023), https://doi.org/10.1016/j.jmapro.2023.11.018

[138] Li et al.https://doi.org/10.1007/s00170-020-05673-4/Published

[139] Shin et al. (2023), https://doi.org/10.1016/j.matdes.2023.111681

[140] Zhao et al. (2023), https://doi.org/10.1007/s00170-023-12348-3

[141] Rodrigues et al. (2022), https://doi.org/10.1016/j.jmrt.2022.08.169

[142] Bodner et al. (2020), https://doi.org/10.1016/j.addma.2019.101027

[143] Bodner et al. (2022), https://doi.org/10.1016/j.jmrt.2022.11.064

[144] Alafaghani et al. (2018), https://doi.org/10.1007/s00170-018-2586-5

[145] Tolosa et al. (2010), https://doi.org/10.1007/s00170-010-2631-5

[146] Mei et al. (2019), https://doi.org/10.1016/j.msea.2019.05.011

[147] Ben-Artzy et al. (2021), https://doi.org/10.1016/j.matdes.2021.109500

[148] Aydogan et al. (2021), https://doi.org/10.3390/met11111717

[149] Félix-Martínez et al. (2021), https://doi.org/10.1007/s00170-021-07320-y

[150] Swain et al. (2021), https://doi.org/10.5772/intechopen.94211

[151] Errico et al. (2022), https://doi.org/10.3390/met12101669

[152] Karmakar et al. (2021), https://doi.org/10.1016/j.surfcoat.2021.127498

[153] Muvvala et al. (2018), https://doi.org/10.1016/j.jallcom.2017.12.364

[154] Zhang et al. (2019), https://doi.org/10.1016/j.jmapro.2019.01.001

[155] Ostolaza et al. (2023), https://doi.org/10.1016/j.surfcoat.2023.129538

[156] Svetlizky et al. (2022), https://doi.org/10.1016/j.msea.2022.142967

[157] Brueckner et al. (2018), https://doi.org/10.2351/1.5040639

[158] Mostafaei et al. (2021), https://doi.org/10.1016/B978-0-12-803581-8.11884-3

[159] Novichenko et al. (2011), https://doi.org/10.1016/j.phpro.2011.03.038

[160] Balokhonov et al. (2022), https://doi.org/10.1016/j.engfracmech.2021.108138

[161] Ngo et al. (2018), https://doi.org/10.1016/j.compositesb.2018.02.012

[162] Raahgini et al. (2022), https://doi.org/10.1016/j.surfcoat.2021.127975

[163] Bandyopadhyay et al. (2022), https://doi.org/10.1016/j.mattod.2021.11.026

[164] Hu et al. (2018), https://doi.org/10.1016/j.ceramint.2018.08.083

[165] Muvvala et al. (2017), https://doi.org/10.1016/j.jallcom.2017.04.254

[166] Bartkowski et al. (2016), https://doi.org/10.1016/j.ijrmhm.2016.04.017

[167] Wang et al. (2019), https://doi.org/10.1016/j.ijrmhm.2019.02.024

[168] Ostolaza et al. (2023), https://doi.org/10.3390/ma16041746

[169] Mertens et al. (2021), https://doi.org/10.1016/B978-0-12-818411-0.00005-7

[170] Nurminen et al. (2009), https://doi.org/10.1016/j.ijrmhm.2008.10.008

[171] Jiang et al. (2007), https://doi.org/10.1016/j.jmatprotec.2006.12.053

[172] Bartkowski et al. (2017), https://doi.org/10.1016/j.ijrmhm.2016.12.013

[173] Adam et al. (2018), https://doi.org/10.1088/1757-899X/430/1/012001

REFERENCES

[174] Traxel et al. (2021), https://doi.org/10.1016/j.addma.2020.101602

[175] Li et al. (2021), https://doi.org/10.1016/j.vacuum.2021.110242

[176] Xie et al. (2021), https://doi.org/10.1016/j.jmrt.2021.08.114

[177] Zhao et al. (2022), https://doi.org/10.1016/j.ijrmhm.2021.105720

[178] Shanenkov et al. (2023), https://doi.org/10.1007/s12540-023-01533-4

[179] Celebi Efe et al. (2011), https://doi.org/10.1016/j.jallcom.2011.02.170

[180] Kumar et al. (2021), https://doi.org/10.1016/j.matpr.2020.08.580

[181] Ostolaza et al. (2022), https://doi.org/10.1016/j.matdes.2022.111172

[182] Jin et al. (2024), https://doi.org/10.1016/j.heliyon.2024.e29666

[183] Guerra et al. (2022), https://doi.org/10.1016/j.addma.2022.102850

[184] Guerra et al. (2019), https://doi.org/10.1016/j.cirpj.2019.09.003

[185] Park et al. (2022), https://doi.org/10.1016/j.addma.2022.102680

[186] Acharya et al. (2015), https://doi.org/10.1002/adem.201400589

[187] Wei et al. (2022), https://doi.org/10.1016/j.addma.2021.102588

[188] Zhang et al. (2022), https://doi.org/10.1016/j.jmrt.2022.01.111

[189] Oropeza et al. (2022), https://doi.org/10.1016/j.addlet.2022.100078

[190] Guerra et al. (2022), https://doi.org/10.1016/j.addma.2022.102850

[191] Casalino et al. (2015), https://doi.org/10.1016/j.optlastec.2014.07.021

[192] D.'Accardi et al. (2023), https://doi.org/10.1007/s10921-023-00936-y

[193] Maconachie et al. (2019), https://doi.org/10.1016/j.matdes.2019.108137

[194] du Plessis et al. (2022), https://doi.org/10.1016/j.pmatsci.2021.100918

[195] Ashby et al. (2005), https://doi.org/10.1098/rsta.2005.1678

[196] Gibson et al. (1997), https://doi.org/10.1017/cbo9781139878326

[197] Lin et al. (2023), https://doi.org/10.3390/ma16020520

[198] Bai et al. (2019), https://doi.org/10.3390/ma12132192

[199] Crupi et al. (2017), https://doi.org/10.1016/j.matdes.2017.09.003

[200] Mazur et al. (2015), https://doi.org/10.1007/s00170-015-7655-4

[201] Zhao et al. (2018), https://doi.org/10.3390/ma11122411

[202] Lei et al. (2019), https://doi.org/10.1016/j.matdes.2019.107685

[203] Amani et al. (2018), https://doi.org/10.1016/j.actamat.2018.08.030

[204] Alaimo et al. (2023), https://doi.org/10.1016/j.ijmecsci.2023.108599

[205] Leary et al. (2016), https://doi.org/10.1016/j.matdes.2016.02.127

[206] Maskery et al. (2016), https://doi.org/10.1016/j.msea.2016.06.013

[207] Tancogne-Dejean et al. (2018), https://doi.org/10.1016/j.ijmecsci.2018.03.027

[208] Gümrük et al. (2013), https://doi.org/10.1016/j.ijmecsci.2013.01.006

[209] McKown et al. (2008), https://doi.org/10.1016/j.ijimpeng.2007.10.005

[210] Wang et al. (2023), https://doi.org/10.1016/j.tws.2022.110439

[211] Zhang et al. (2023), https://doi.org/10.1016/j.ijmecsci.2023.108616

[212] Liu et al. (2017), https://doi.org/10.1016/j.jmps.2017.07.003

[213] Qi et al. (2019), https://doi.org/10.1016/j.ijmecsci.2019.105091

[214] Patel AD et al. (2015), https://doi.org/10.4172/2169-0022.1000191

[215] Schindelin et al. (2012), https://doi.org/10.1038/nmeth.2019

[216] Palmieri et al. (2023), https://doi.org/10.1002/srin.202200665

[217] Zikmund et al. (2019), https://doi.org/10.1016/j.ndteint.2019.02.008

[218] Bajaj et al. (2020), https://doi.org/10.1016/j.msea.2019.138633

[219] Meredith et al. (2018), https://doi.org/10.1016/j.msea.2018.09.066

[220] Parmar et al. (2022), https://doi.org/10.1080/09506608.2021.1954805

[221] Grazia Guerra et al. (2023), https://doi.org/10.1016/j.optlastec.2023.109252

[222] Blinn et al. (2019), https://doi.org/10.1016/j.ijfatigue.2019.03.022

[223] Kgee Ong et al. (2022), https://doi.org/10.1016/j.matpr.2022.09.362

REFERENCES

[224] Tan et al. (2021), https://doi.org/10.1016/j.msea.2020.140642

[225] Song et al. (2019), https://doi.org/10.1016/j.optlastec.2019.105725

[226] Blinn et al. (2020), https://doi.org/10.1016/j.ijfatigue.2019.105301

[227] Prime et al. (2001), https://doi.org/10.1115/1.1345526

[228] Carone et al. (2022), https://doi.org/10.3390/met12122039

[229] Zhang et al. (2023), https://doi.org/10.1016/j.jmapro.2023.08.019

[230] Prime et al. (2013),

[231] Hosseinzadeh et al. (2014), https://doi.org/10.1049/joe.2014.0134

[232] Ghasri-Khouzani et al. (2017), https://doi.org/10.1016/j.msea.2017.09.108

[233] Yu et al. (2019), https://doi.org/10.1016/j.jmapro.2019.09.010

[234] Campanelli et al. (2019), https://doi.org/10.1088/2053-1591/ab0c6e

[235] Serrano-Munoz et al. (2021), https://doi.org/10.1002/adem.202100158

[236] Serrano-Munoz et al. (2021), https://doi.org/10.1007/s10853-020-05553-y

[237] Mishurova et al. (2018), https://doi.org/10.1007/s11661-018-4653-9

[238] Clausen et al. (2020), https://doi.org/10.1016/j.addma.2020.101555

[239] Pagliaro et al. (2011), https://doi.org/10.1007/s11340-010-9424-5

[240] Xu et al. (2022), https://doi.org/10.1016/j.actamat.2022.118307

[241] ISO: Geneva et al.

[242] Liyanage et al. (2010), https://doi.org/10.1016/j.surfcoat.2010.07.095

[243] Blakey-Milner et al. (2021), https://doi.org/10.1016/j.matdes.2021.110008

[244] Jiménez et al. (2019), https://doi.org/10.1155/2019/9656938

[245] Ganesh Sarvankar et al. (2019),

[246] Errico et al. (2021), https://doi.org/10.3390/ma14030673

[247] Akbari et al. (2019), https://doi.org/10.1007/s00170-019-04195-y

[248] Niu et al. (2019), https://doi.org/10.1016/j.actamat.2019.08.042

[249] Jiang et al. (2020), https://doi.org/10.1016/j.ijleo.2019.164044

[250] Bidare et al. (2021), https://doi.org/10.1007/s40436-021-00365-y

[251] 28. Adams et al. (2001),

[252] Simson et al. (2019), https://doi.org/10.1016/j.prostr.2019.08.112

[253] Angelastro et al. (2009), https://doi.org/10.4028/www.scientific.net/AMR.83-86.842

[254] Zhu et al. (2021), https://doi.org/10.1016/j.optlastec.2021.106915

[255] Steen et al. (1991), https://doi.org/10.1007/978-1-4471-3820-4

[256] Steen et al. (1986), https://doi.org/10.1117/12.938104

[257] Angelastro et al. (2011), https://doi.org/10.4028/www.scientific.net/KEM.473.75

[258] Svetlizky et al. (2021), https://doi.org/10.1016/j.mattod.2021.03.020

[259] Traxel et al. (2020), https://doi.org/10.1016/j.mfglet.2020.08.005

[260] Papynov et al. (2018), https://doi.org/10.1016/j.matchar.2018.08.044

[261] Developed by Subcommittee: E28.06 et al. (2013),

[262] Campanelli et al. (2019), https://doi.org/10.3390/ma12152397

[263] Garcia-Ayala et al. (2021), https://doi.org/10.1016/j.ijrmhm.2021.105565

[264] Trueman et al. (1998), https://doi.org/10.1016/S0010-938X(98)00069-9